Semi-Classical Hamiltonian Daemons

Approaching Daemons in Phase-Space

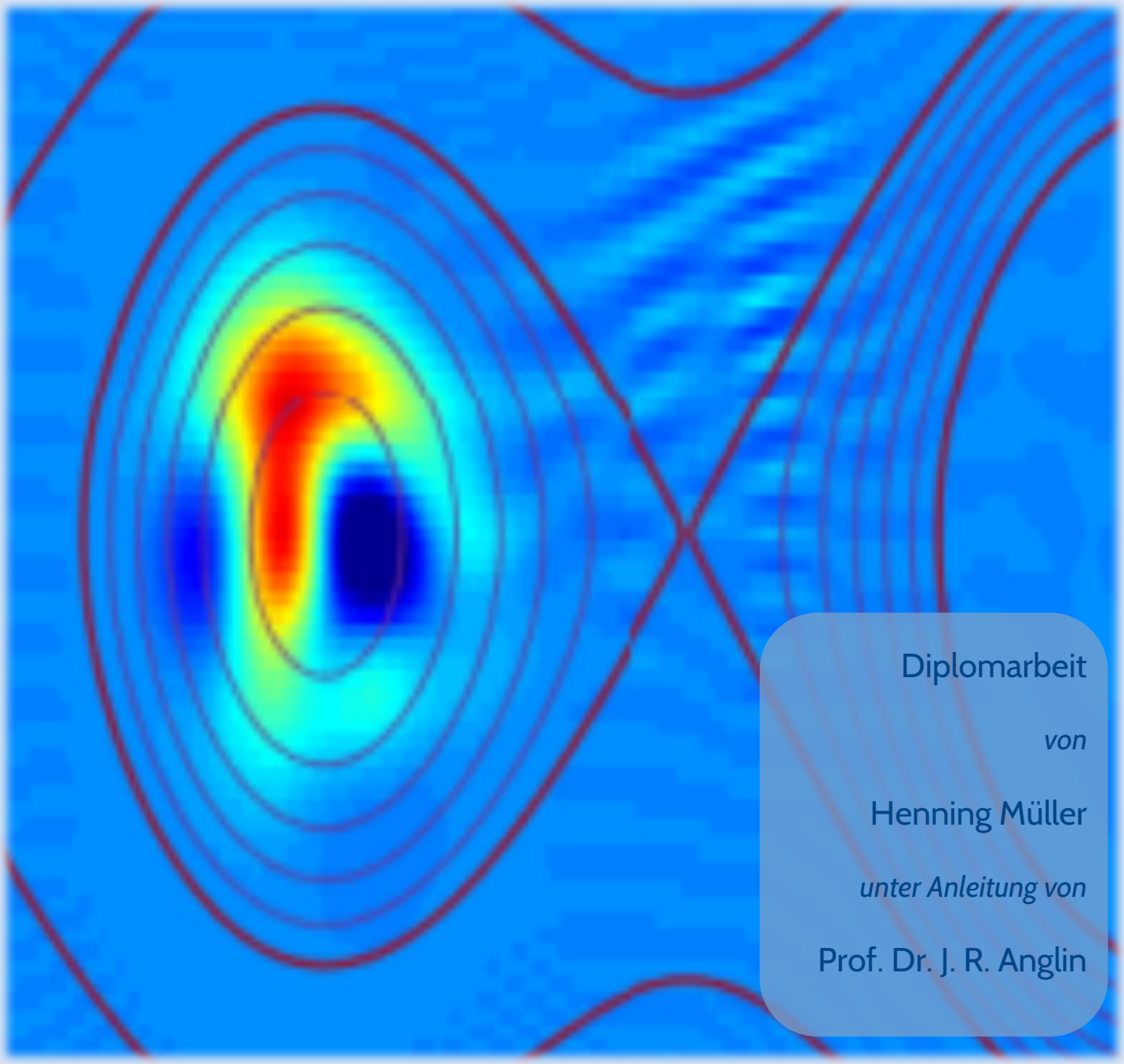

Diplomarbeit

von

Henning Müller

unter Anleitung von

Prof. Dr. J. R. Anglin

TECHNISCHE UNIVERSITÄT
KAISERSLAUTERN

Fachbereich Physik

Semi-Classical Hamiltonian Daemons

Diplomarbeit

in

Theoretischer Physik

von

Henning Müller

durchgeführt am

Fachbereich Physik

der Technischen Universität Kaiserslautern

unter Anleitung von

Prof. Dr. J. R. Anglin

November 2019

Zusammenfassung

Hamiltonsche Dämonen ermöglichen es Energie von Systemen mit sehr schnellen auf solche mit langsameren Freiheitsgraden zu übertragen, auch über viele Größenordnungen der entsprechenden Zeitskalen hinweg. Sie agieren auf kleinsten Skalen und können als Mikromotoren angesehen werden.

Bisher wurden solche Dämonensysteme im klassischen sowie im quantenmechanischen Bereich beschrieben. In dieser Arbeit wird nun der semi-klassische Bereich untersucht, in dem Quantenphänomenen als Korrektur an klassischen Systemen auftreten. Das Augenmerk liegt hierbei auf numerischen Simulationen.

Untersucht werden zunächst einführende Modelle die sich mit dem Tunneleffekt befassen, da dieser als bedeutende Quantenkorrektur auftritt, sowie mit dem Gewinn und Zerfall gebundener Zustände, da dies die Übergänge zwischen den dynamischen Phasen eines Dämons – adiabatische Entkopplung und Downconversion – darstellt.

Die Untersuchungen erfolgen numerisch anhand von Wellenfunktionen aus der Schrödinger-Gleichung und mittels Wignerfunktionen in einem quantenmechanischen Phasenraum im Rahmen des Weyl-Wigner-Groenewold-Moyal-Formalismus. Die Wignerfunktionen werden zum Einen aus den Wellenfunktionen berechnet, zum Anderen kommt eine numerische Methode auf Grundlage der Moyalgleichung zum Einsatz, welche hier vorgestellt wird.

Die so erarbeitete Methodik wird anschließend zur Betrachtung eines Dämonsystems mit tilted washboard-Potential eingesetzt. Untersucht wird das Verhalten des Dämon im Hinblick auf auftretende Quantenkorrekturen, insbesondere im Phasenraum und bezüglich des Kruskal-Theorems, welches den Einfang von Phasenraumfluss durch eine zeitlich veränderliche Separatrix beschreibt.

Der semi-klassisch quantisierte Phasenraum wird schließlich als Grundlage einer kombinierten Beschreibung von klassischen und quantenmechanischen Dämonen diskutiert. Das Verhalten des Energiespektrums im tiefen Quantenbereich wird hier durch dynamisches Tunneln erklärt.

Abstract

Hamiltonian daemons allow the transfer of energy from systems with very fast degrees of freedom to systems with slower ones across several orders of magnitude. They act on small scales and can be regarded as micro-engines.

Such daemons were previously described in the classical as well as the quantum mechanical regime. In this thesis the semi-classical regime is examined, where quantum phenomena occur as corrections to classical systems. Here, the focus is on numerical simulations.

First some introductory models are examined. They are concerned with quantum tunneling, since it occurs as an important quantum correction, as well as with the capture and decay of bound states, since this represents the transition between the dynamical phases of a daemon: adiabatic decoupling and downconversion.

The examinations are carried out using wave functions, as solutions to the Schrödinger equation, and by means of Wigner functions in a quantum mechanical phase-space in the framework of the Weyl-Wigner-Groenewold-Moyal formalism. For one these Wigner functions are computed from the wave functions, but they are also obtained from a numerical method based on the Moyal equation, which will be introduced here.

After developing this methodology, it is employed in the study of a daemon system with a tilted washboard potential. The daemon behavior is studied with regards to quantum corrections, especially in phase-space and concerning Kruskal's theorem, which describes the capture of phase-space flow via a time-dependent separatrix.

Lastly the semi-classically quantized phase-space will be discussed as a basis for a combined description of both classical and quantum daemons. The behavior of the energy spectrum in the deep quantum regime is explained by dynamical tunneling processes.

Contents

I. Introduction

This chapter introduces the fundamentals of Hamiltonian engines given in previous publications, upon which this thesis will build.

First, **section I.a** provides a brief motivation for micro-engines from the realm of cellular biology, delivering some important keywords of the topic in advance.

Section I.b gives the introduction to Hamiltonian daemon engines and their behavior in phase-space in the scope of classical mechanics, followed by the deep quantum regime.

Section I.c delivers the outline, which highlights the areas of interest to be explored and presents the structure of this thesis. It also contains a few remarks about the handling of constants and units.

I.a. Motivation

The big picture is about energy exchange and transport processes on microscopic scales, *i. e. micro-engines.*

In biological systems there are proteins that act as *molecular machines*[2]. They convert chemical energy to mechanical work and can generate movement or transport cargo.

A concrete example from the field of cell biology is the enzyme *V-ATPase*[3], illustrated in Figure I.1. In its upper section (V_1) the molecule *adenosine triphosphate* (ATP) is used as an energy source by hydrolyzing it to adenosine diphosphate (ADP) and phosphate, whereupon chemical energy is made available. This lets the lower section V_O rotate, facilitating the (active) transport of protons through the membrane. This protein therefore is a proton pump, acting against the concentration gradient of the protons.

In other terms, V-ATPase is an engine that uses energy from a fuel source to power a pump.

This demonstrates the direct coupling of different subsystems with dynamics on vastly *different time scales*: the chemical energy corresponds to a fast time scale (10^{13} Hz)[4], whereas the rotation happens a much slower time scale (10^1 to 10^2 Hz)[5]. Energy is converted over many orders of magnitude.

Such proteins may be macromolecules, but they are still microscopic systems on the boundary between classical and quantum physics. While macroscopic engines are de-

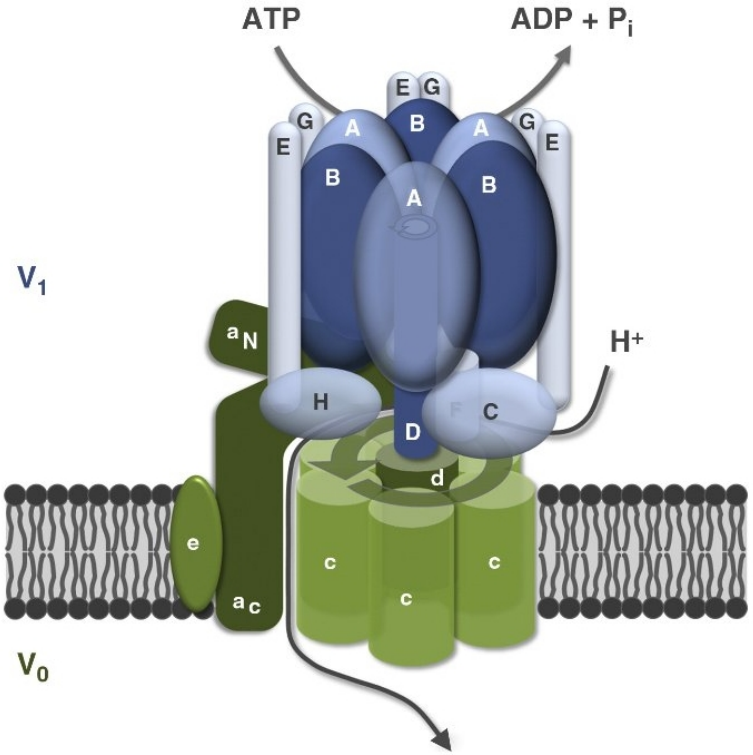

Figure I.1.: from [1]; The enzyme V-ATPase converts the chemical energy of the hydrolysis of ATP to mechanical work in the form of rotation.

scribed in terms of thermodynamics with large ensembles and thermal reservoirs, this will not work at these scales.

To explore the mechanisms behind micro-engines, *Hamiltonian Daemons* use the formalism of closed Hamiltonian systems. This could even lead to the microscopic origins of thermodynamics.

I.b. Introduction to Hamiltonian Daemons

Engines are complex systems that are commonly described in the language of thermodynamics. In this section a description based on closed Hamiltonian systems is presented, that does not rely on macroscopic baths, but rather shows energy transfer between weakly coupled microscopic subsystems.

This section serves as an overview of the subject and a background for the thesis with the necessary definitions. Further details can be found in the journal articles [6, 7] and the dissertations [8, 9].

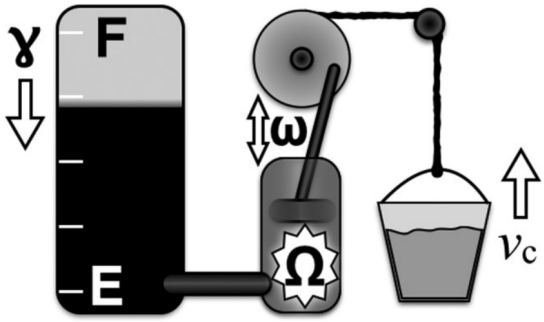

Figure I.2.: from [6]; Illustration of an engine with different time scales.

1. Introduction to Hamiltonian Engines

To understand Hamiltonian daemons it is necessary to look at adiabatic decoupling first. For this a systems is regarded that contains subsystems with dynamics on greatly differing time scales. For these subsystems to effectively interact and exchange energy some sort of resonance condition has to be fulfilled. Otherwise they are considered to be decoupled and can be regarded as independent of each other. This phenomenon is called *adiabatic decoupling* and is usually used as an approach to eliminate high frequency terms in Hamiltonians describing slower evolutions.

The idea behind Hamiltonian daemons is to bypass the decoupling and facilitate an exchange of energy, even across multiple orders of magnitude between the time scales of the subsystems.

This invokes a thought experiment of James Clerk Maxwell: *Maxwell's demon*. Just like this suggested a violation of the second law of thermodynamics, *Hamiltonian daemons* target the concept of adiabatic decoupling.

The kind of systems these daemons represent should be made a bit more concrete. Figure I.2 shows an illustration of an engine that lifts a weight in a gravitational field. It can be described by a general classical Hamiltonian

$$\mathcal{H} = \mathcal{H}_{\mathrm{W}} + \mathcal{H}_{\mathrm{F}} + \gamma\,\mathcal{H}_{\mathrm{E}}. \tag{I.1}$$

This engine features a fuel tank (F) – representing the fast degrees of freedom – coupled with strength γ to the engine subsystem (E) – with time scale Ω – which in turn is coupled to the work subsystem (W) – with time scale ω – lifting the weight with a speed v_{c}.

Such an engine can already be understood by means of thermodynamics, *e. g.* a combustion engine. The description involves thermal reservoirs, *i. e.* macroscopic subsystems.

Daemon engines on the other hand are *micro-engines*: closed systems described in terms of Hamiltonian mechanics which can also work on microscopic scales.

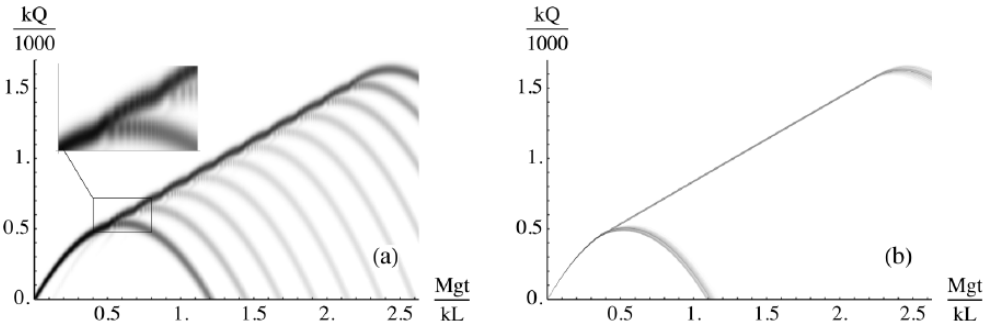

Figure I.3.: from [7]; Dynamics of a classical engine for the Position Q. *left:* The quantum system splits into multiple branches. *right:* The classical system shows steady lift with speed v_c.

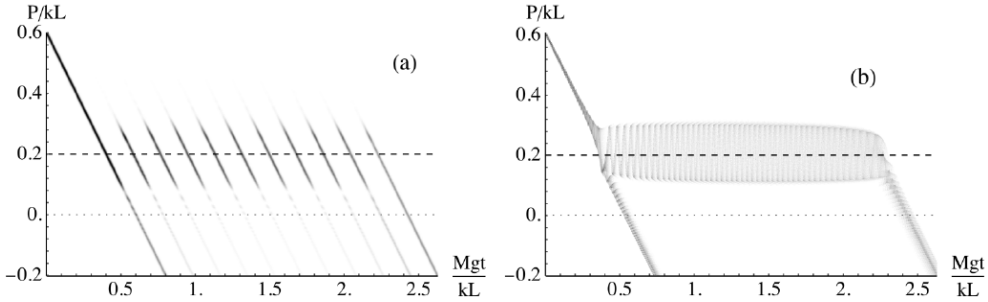

Figure I.4.: from [7]; Dynamics of a classical engine for the Momentum P. *left:* The quantum system shows periodic quantum jumps in downconversion. *right:* The classical system oscillates around p_c.

2. Description of the Dynamics

The phenomenon of the energy exchange despite adiabatic decoupling is called *downconversion*, as the energy of the fast subsystem is converted down to the slow subsystem. This works via non-linear coupling, which can occur in small regions of phase-space.

A classical Hamiltonian for a daemon engine can be given as[a]:

$$\mathcal{H} = \frac{P^2}{2M} + Mg\Omega + \Omega L_z - \gamma \left(L_x \cos(kQ) + L_y \sin(kQ) \right), \tag{I.2}$$

where Q is the height, P the momentum, M the mass raised against gravity g. The angular momentum L represents the fast degrees of freedom with high frequency Ω. The rate γ and the inverse length k are coupling parameters.

The resulting dynamics are depicted in Figure I.3 for the position Q and in Figure I.4 for the momentum P. Without downconversion the weight follows the usual parabola with a linearly decreasing momentum. At momentum $P = \frac{M\Omega}{k}$ a transition to a different dynamical phase occurs. The weight rises at critical speed $v_c = \frac{\Omega}{k}$ against gravity, while the momentum oscillates around a critical value p_c.

[a] Equation (1) from [7]

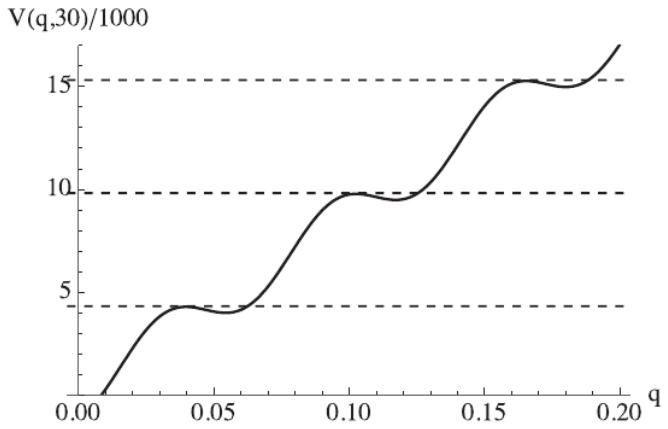

Figure I.5.: from [6]; The tilted washboard potential of the effective Hamiltonian H_5 in [6], which is closely related to Equation I.3.
The potential can exhibit local potential wells, facilitating bound orbits.

Since total energy is conserved, the power needed to drive the weight upwards is supplied by the high-frequency subsystem, *i. e.* the engine's fuel tank, until its energy reserve is expended. The resonant effects keep the weight's speed near v_c during this driving. The steady transfer of energy is *steady downconversion*.

The Hamiltonian of Equation I.2 can be rewritten as the effective Hamiltonian[b]:

$$\mathcal{H}_{\text{eff}} = \frac{k^2 L_z^2}{2M} + gktL_z - \gamma\sqrt{L^2 - L_z^2} \tag{I.3}$$

This is now an explicitly time-dependent Hamiltonian. The problem is reduced to a single particle (the weight) in a time-dependent potential exhibiting local potential wells.

Due to the sinusoidal shape (for fixed t) the potential V of Equation I.3 is called a *tilted washboard* potential. Such a potential is depicted in Figure I.5. V is considered adiabatically, where it is taken at fixed point in time with the parameters then slowly changing with t.

In Reference [6] a series of transformations is shown to result in a Hamiltonian (H_5), which is closely related to the effective Hamiltonian. This amounts to a shift in the momentum, changing the problem to the comoving frame where $v_c = 0$, since the stable fixpoint is now a local minimum in the potential.

3. The Phase-Space of Daemon Engines

For the phase-space yet another version of the daemon Hamiltonian is introduced: a rescaled effective Hamiltonian from [8]:

[b] Equation (4) from [7], obtained from the semi-classical limit of I.6
[c] from H_2 (Equation (8)) in [10]

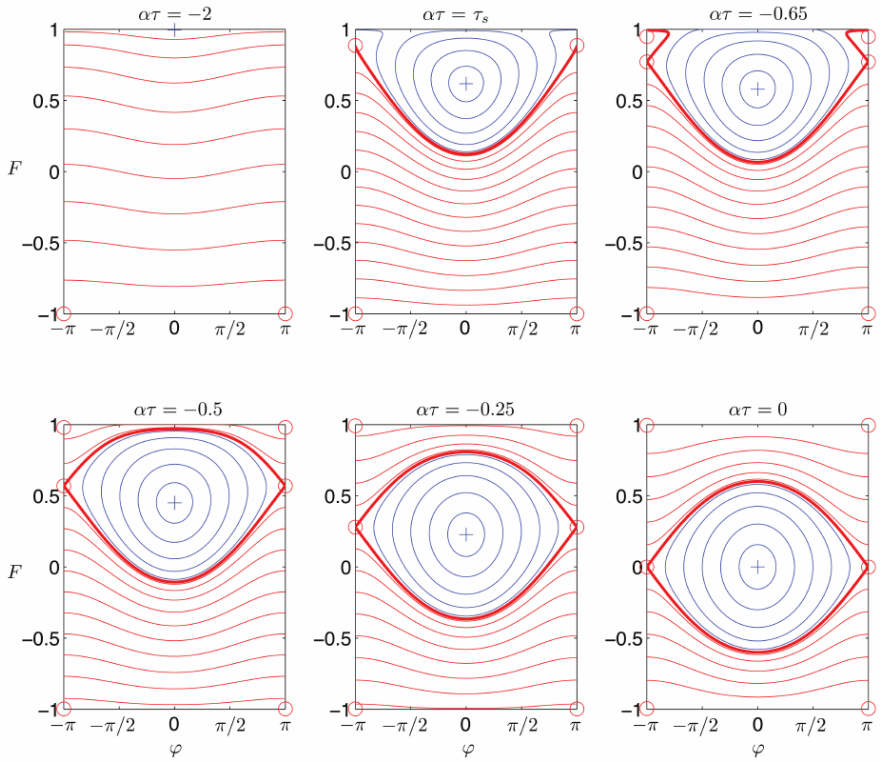

Figure I.6.: from [8]; The phase-space of the rescaled effective Hamiltonian I.4 for different times $\alpha\tau$.
Unstable fixpoints are marked by a red circle, the stable fixpoint by a blue cross. Thin red lines are open trajectories, blue lines the bound orbits. The thick red line marks the separatrix.

$$\mathcal{H}_{\text{eff}} = \frac{F^2}{2} + \alpha(\tau - \tau_0)F - \bar{\gamma}\sqrt{1 - F^2}\,\cos(\phi). \tag{I.4}$$

Here (ϕ, F) are canonically conjugate action-angle variables, where F can be regarded as the amount of fuel in the tank.

The phase-space for this Hamiltonian at different times $\alpha\tau$ is shown in Figure I.6. The separatrix divides the adiabatic regions. Open trajectories belong to the adiabatically decoupled phase, indicating that the engine is not running. Bound orbits are closed around the stable fixpoint and slowly drift downwards to lower fuel levels with it, indicating a running engine.

For the effective model with a tilted washboard potential the phase-space in Figure I.7 is now quasi-periodic. The two dynamical regions are still present. Most trajectories are open and display adiabatic decoupling, with only slight undulations. However, within

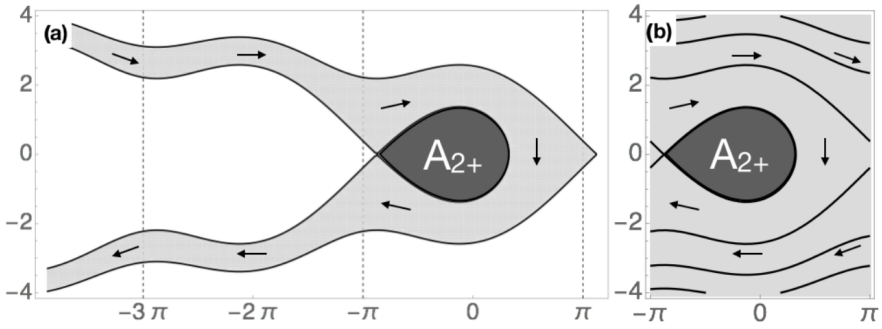

Figure I.7.: from [10]; The phase-space for a tilted washboard potential[c] $V = \dot{\lambda}\phi - \beta^2 \cos\phi$ with flow around the separatrix.

an enclosed separatrix area (A_{2+}) bound orbits are possible, corresponding to the local wells in the potential.

In order for the daemon engine to start – or stall – transitions between these regions must be possible. Incompressible phase-space flow, based on Liouville's theorem, would not permit this. However, for systems with a slowly time-dependent Hamiltonian the separatrices slowly move and deform while also changing in size. Trajectories can then cross over because of *post-adiabatic* effects, as the trajectories close to a separatrix are non-adiabatic. The effective Hamiltonian I.4 (or I.3) is now explicitly time-dependent.

The probability for transitions is given by *Kruskal's theorem*[11] based on the rate of growth of the separatrix area. In [10] this is extended and additionally transport processes in phase-space are considered.

4. Daemons in the Deep Quantum Regime

Hamiltonian daemons can not only be regarded in classical mechanics, and truly microscopic systems would invoke the laws of quantum physics. The Hamiltonian I.2 was already the classical analog of:

$$\hat{H} = \frac{1}{2M}\hat{P}^2 + Mg\hat{\Omega} + \Omega\hat{L}_z - \frac{\gamma}{2}\left(\hat{L}_- e^{ik\hat{Q}} + \hat{L}_+ e^{-ik\hat{Q}}\right). \tag{I.5}$$

With the effective Hamiltonian:

$$\hat{H}_{\text{eff}} = \frac{k^2\hat{L}_z^2}{2M} + gkt\hat{L}_z - \gamma\hat{L}_x \tag{I.6}$$

If the phase-space is quantized by the Bohr-Sommerfeld procedure and thus regarded semi-classically, the separatrix area corresponds to a maximum number of allowed bound states N. The quantum daemon is considered here in the *deep quantum regime* for $N < 1$.

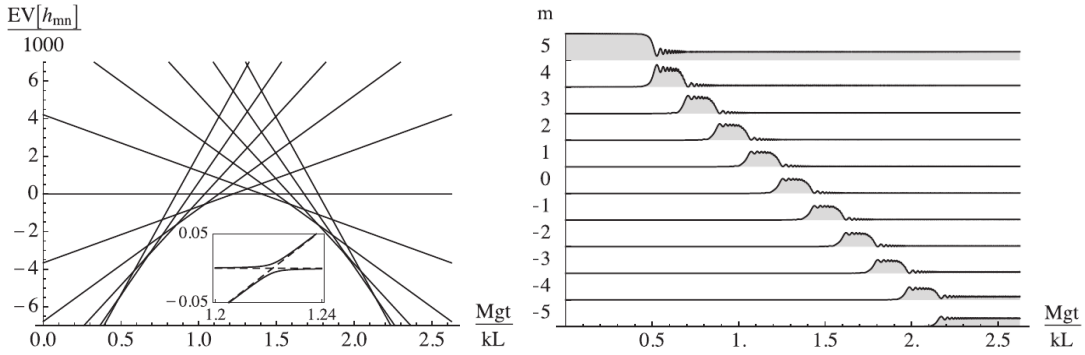

(a) instantaneous eigenspectrum (b) fuel occupation numbers

Figure I.8.: Quantum evolution generated by $\hat{H}_{\text{eff}}$ (I.6). *(a)*: The instantaneous eigenspectrum with avoided crossings. *(b)*: The probability for fuel occupation numbers m over time. probability for the fast subsystem to occupy particular $|m\rangle$ states over time.

The evolution generated by $\hat{H}_{\text{eff}}$ (I.6) can now be understood by the examination of the instantaneous eigenspectrum, depicted in Figure I.8a. It implies that the system's amplitude to make transitions between different $|m\rangle_f$ states[d] is negligible, thus not performing steady downconversion. The spectrum shows that the instantaneous eigenvalues of different $|m\rangle_f$ states would cross. However, there are quantum mechanical resonances which resolve this, leading to avoided crossings. This can now be regarded with Landau-Zener transitions, which gives a probability for adiabatic transitions from initial $|m\rangle$ to $|m-1\rangle$ states.

The quantum evolution for position and momentum is shown in the left plot of Figure I.3 respectively I.4. Starting in the ground state $|m\rangle = |l\rangle$ of the eigenspectrum the systems remains adiabatically in the $|l\rangle_f$ state until the first avoided crossing is encountered. Here a bifurcation into a diabatic (decoupling) and an adiabatic (downconversion) branch occurs. The diabatic branch corresponds to the continued fall along the parabolic curve with linearly decreasing momentum, while the adiabatic branch means a drop from $|l\rangle_f$ to $|l-1\rangle_f$, resulting in an upwards kick in the momentum.

Figure I.8b shows how the probability for different fuel occupation numbers favor a decrease in m over time. The probability amplitude does, however, oscillate back and forth several times, as can also be seen in the inset of Figure I.3.

[d] The quantum number m describes occupation numbers in the fuel system, in contrast to the weight's Mass M.

I.c. Outline of the Thesis

1. Scope

So far daemon engines have been examined in the classical and the deep quantum regime.

The classical description of daemon engines as well as transport mechanisms is based on phase-space quantities, while the quantum description utilizes the Hamiltonian's energy spectrum.

The question is: How are these descriptions connected?

Now the semi-classical regime is regarded. This provides insight into the emergence of quantum behavior and the resulting quantum corrections to otherwise classical systems. And additionally enables the examination of the direct quantum analogs as an extension of such classical systems.

Apart from the usual approximations, a phase-space formalism of quantum mechanics lends itself to the description of semi-classical daemon engines. This extends classical theories to quantum mechanics and allows the use of phase-space quantities, like the separatrix area, for the quantum daemon engines and quantum transport processes.

Numerical methods to study such system are of interest.

This thesis examines the semi-classical regime of Hamiltonian daemons with an emphasis on numerical computations.

An example for a daemon Hamiltonian is simulated, modeled as an analog of a system described in a previous publication. Additional models illustrate aspects thereof.

2. Structuring

Quantum Tunneling is thought to be the main correction to classical systems. Thus **chapter II** starts with theoretical background on tunneling processes and the decay of quasi-bound states.

This is then examined numerically through a series of model systems: the scattering of a particle on a barrier, the decay of a particle trapped behind a barrier via tunneling and the inverse problem of capturing a free particle behind a barrier. These models exemplify some aspect of the tilted washboard potential examined in chapter IV.

Chapter III introduces the *Weyl-Wigner-Groenewold-Moyal*-formalism of quantum mechanics on a phase-space, involving the Wigner quasi-probability distribution. The the models of chapter II are then explored in phase-space by computing the Wigner functions as a transform of the numerical wave functions.

After that an alternative scheme for simulations of time evolutions in phase-space is presented, which is followed by exemplary models. The chapter concludes in a comparison of both methods.

Chapter IV examines a quantum daemon engine by simplifying a tilted-washboard-Hamiltonian via a time-dependent control parameter conveying the dynamical evolution of the potential. The model and its characteristics are presented in the context of daemon engines. The time evolution is simulated with the methods of the previous two chapters.

Afterwards an attempt at going further beyond the simplified model is undertaken. For that, a genuine quantum daemon Hamiltonian is rewritten in an *exact quantum phase model* representation. The results and the occurring problems are discussed.

Chapter V deals with merging classical and quantum daemons into one description, based on a semi-classical phase-space. The proposed theory explains the dynamical evolution of daemon engines through phase-space quantities.

For this, avoided crossings in the quantum spectrum are linked to dynamical tunneling processes between different regions in phase-space.

Chapter VI concludes the main part of this thesis by summarizing the results and indicating potential future research.

Appendix A elaborates on some of the theoretical framework concerning quantum mechanics in phase-space.

Appendix B explains the numerical algorithms used for the simulations and summarizes details on computational implementations.

Appendix C delivers additional derivations of equations and other entities.

3. Explanatory Notes

Equations will be given in natural units, with Planck's constant $\hbar \equiv 1$ and the weight's mass $M \equiv 1$, resulting in dimensionless quantities, *e. g.* position q, momentum p and time t.

Sections introducing theoretical background and equations will feature $\hbar$ or M for clarity.

M (upper case) describes a mass, whereas m (lower case) describes a quantum number, usually in regards to occupation numbers.

II. Basics of Tunneling and Decay Theory

This chapter takes a look at tunneling in different contexts.

Section II.a establishes a theoretical basis concerning the tunneling of particles through an arbitrary potential barrier in general, as well as the decay of initially bound states via tunneling.

Section II.b introduces a numerical scheme to solve the Schrödinger equation first. Then several models are introduced and their behavior is simulated numerically. This will showcase different aspects of tunneling, primarily the decay of bound states in a local potential well. Additionally, the inverse problem will be treated: capturing initially free particles in a potential, either by tunneling through a barrier or by raising the barrier behind the particle.

II.a. Theoretical Overview

1. Tunnel Effect

One effect not witnessed in classical mechanics is the so-called *tunnel effect*[12], where a particle can start out on one side of a potential barrier and appear on the other side, even though the energy of the particle is lower than the local maximum of the potential.

In the following textbook example a brief theoretical explanation will be given for the specific case of a rectangular potential barrier.

The barrier of height V_0 and width w is given by

$$V(q) = \begin{cases} V_0, & -\frac{w}{2} \leqslant q \leqslant \frac{w}{2}, \\ 0, & \text{else} \end{cases} \tag{II.1}$$

An illustration of such a potential is given in Figure II.1. Assuming an incoming particle from the left ($q < -\frac{w}{2}$) with mean energy $E_{kin} < V_0$, the region of the finite barrier ($-\frac{w}{2} \leqslant q \leqslant \frac{w}{2}$) would be classically forbidden and and a classical particle could not traverse it to reach the right side of the barrier ($q > \frac{w}{2}$).

In quantum mechanics this is different, as can be deduced from these solutions to the Schrödinger equation:

$$\psi(q) = \begin{cases} e^{ikq} + \mathcal{R}e^{-ikq}, & q < -\frac{w}{2}, \\ Ce^{i\kappa q} + De^{-i\kappa q}, & -\frac{w}{2} \leqslant q \leqslant \frac{w}{2}, \\ \mathcal{T}e^{ikq}, & q > \frac{w}{2}, \end{cases} \tag{II.2}$$

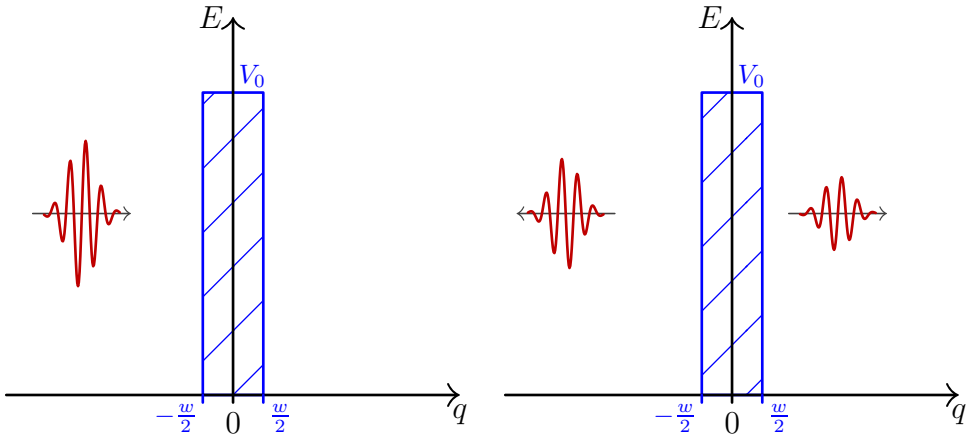

(a) A wave packet approaches the barrier.

(b) A part of the wave packet has been reflected, but the rest tunneled through the barrier, continuing to travel to the right.

Figure II.1.: A rectangular potential barrier of height V_0 centered around $q = 0$.

where $k = \sqrt{2E}$, $\kappa = \sqrt{2(V_0 - E)}$ and $\mathcal{R}$, C, D, $\mathcal{T}$ are energy-dependent constants. The solutions in Equation II.2 describe an incoming wave superposed with a reflected wave of amplitude $\mathcal{R}$ to the left. Due to constraints on the continuity and differentiability of the wave function at the boundaries of the potential barrier, the wave function does continue into the barrier region, where it decreases exponentially, and further beyond the barrier to the right as an outgoing wave of amplitude $\mathcal{T}$.

The probabilities for reflection and transmission are then given by $|\mathcal{R}|^2$ and $|\mathcal{T}|^2$. This means that for a barrier which is neither too high nor too wide, there exists a non-negligible amplitude of the solution at the right boundary, giving rise to a non-vanishing probability of transmission.

In classical mechanics this cannot happen, but a quantum particle can *tunnel* through a potential barrier, This is an effect inherent to quantum systems because of the wave characteristics of solutions to the Schrödinger equation.

2. Decay of Quasi-Stationary States

Tunneling also comes into effect when a particle is trapped behind a barrier. The initial situation is a potential well with infinitely high walls. At the initial time $t = 0$ one wall of the potential is changed to a barrier of finite height V_0 and width w[a], with a vanishing value beyond that (see Figure II.2). This system does allow for quasi-bound states with energies E_R below V_0 as well as unbound states above V_0.

The setup for a system regarded in this section is the following: A single particle is

[a] Generally, $w = r_2 - r_1$ (see Figure II.2b) and thereby energy-dependent. For the the rectangular barrier this simplifies to $w = b - a$.

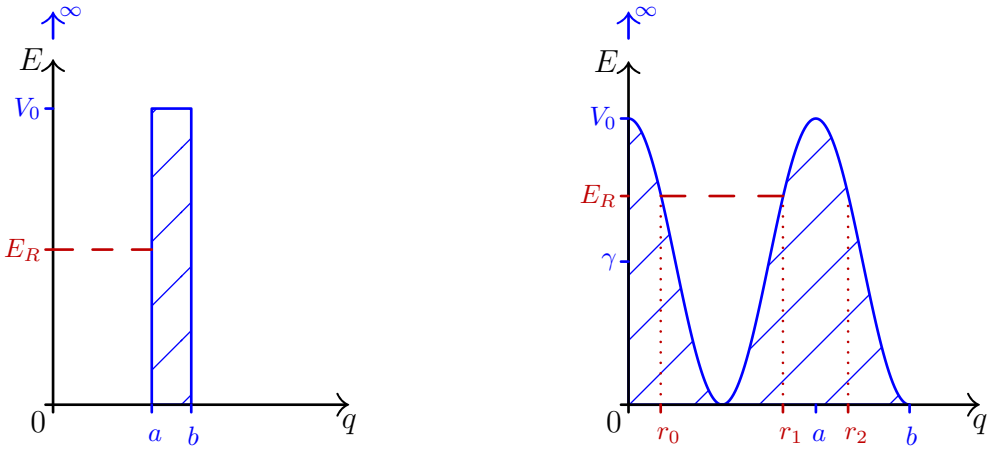

(a) rectangular barrier

(b) cosine barrier

Figure II.2.: Two types of potential barrier, separating a well from the free region. The dashed red line shows an arbitrary resonance energy E_R of an initial quasi-bound state.
(a): The rectangular barrier has a width of $w = b - a$ and a height V_0.
(b): The cosine barrier has a height of $V_0 = 2\gamma$ and an energy-dependent width defined by the classical turning points, which are marked in red as r_0 to r_2.

bound in the infinite potential well, represented by an eigenstate $|\Psi_0(E_R)\rangle$ with corresponding eigenenergy E_R which does not change over time and is therefore *stationary*. The potential is then changed to the finite barrier with $V_0 > E_R$. This change is assumed to be happening without altering the particle's state. Now $|\Psi_0\rangle$ is not an eigenstate anymore, but rather a superposition of all energy-eigenstates. Thus, it will decay over time and it will do so by tunneling through the barrier. Such a state is referred to as being *quasi-stationary*. These systems are of interest in particle and nuclear physics, and the theory was first developed to describe α-decay[13].

Non-decay Probability

Of interest is now the time-evolution of such a quasi-stationary state and especially the probability that the state has not decayed within the time interval $(0, t)$, called the non-decay probability $P_{\text{nd}}(t)$.

The starting point for the decay problem[14] is:

$$P_{\text{nd}}(t) = |A(t)|^2, \tag{II.3}$$

with the amplitude:

$$A(t) = \langle\psi|\ e^{-i\hat{H}t}\ |\psi\rangle\,. \tag{II.4}$$

$\hat{H}$ is the time-independent Hamiltonian which determines the system's evolution.

$|\psi\rangle$ is not an eigenstate of the system and will therefore be expanded in the energy basis. A complete set of commuting operators including $\hat{H}$ is considered: $(\hat{H}, \hat{\alpha})$, with the common eigenstates $|\phi_{E,a}\rangle$ and the eigenvalues:

$$\hat{H}\,|\phi_{E,a}\rangle = E\,|\phi_{E,a}\rangle\,, \tag{II.5}$$

$$\hat{\alpha}\,|\phi_{E,a}\rangle = a\,|\phi_{E,a}\rangle\,. \tag{II.6}$$

By expanding the state $|\psi\rangle$ in a series of these $|\phi_{E,a}\rangle$, Equation II.4 can be written as:

$$A(t) = \int_{E_{\min}}^{\infty} \mathrm{d}E\ \omega(E)\, e^{-iEt} \tag{II.7}$$

with the energy distribution

$$\omega(E) = \int \mathrm{d}a\ |\langle\phi_{E,a}|\psi\rangle|^2\,. \tag{II.8}$$

The limit $E_{\min}$ in the integral of Equation II.7 stems form the fact the Hamiltonian of any physically relevant system is bounded from below. By defining:

$$\tilde{\omega} = \begin{cases} 0, & E < E_{\min} \\ \omega, & E \geqslant E_{\min}, \end{cases} \tag{II.9}$$

the integration can be written as a Fourier transform:

$$A(t) = \int_{-\infty}^{+\infty} \mathrm{d}E\ \tilde{\omega}(E)\, e^{-iEt} \tag{II.10}$$

For ω the Breit-Wigner[15,16] form[b] can be chosen, which is given by:

$$\omega(E) = \frac{1}{\pi}\frac{\Gamma/2}{(E-E_R)^2 + (\Gamma/2)^2} \tag{II.11}$$

where Γ is the half-width of the distribution.

Any energy distribution ω' that is very similar to the Breit-Wigner form ω in a large enough interval around E_R results in probabilities P'_{nd} which are close to P_{nd}.

If $E_{\min} = -\infty$ is assumed in II.7, then $A(t)$ is the Fourier transform of ω, resulting in $A(t) = \exp(-iE_Rt - \frac{\Gamma}{2}t)$ and $P(t) = \exp(-\Gamma t)$, which would give the well-known exponential law of decay. But this assumption is not physically possible. A finite lower bound on the energy effectively means cutting of a part of the energy distribution. Hence $A(t)$ cannot be a pure exponential[17].

The derivative of $P_{\mathrm{nd}}(t)$ vanishes at $t = 0$. For large times, $\lim_{t\to\inf} A(t) = 0$ and $P_{\mathrm{nd}}(t)$ vanishes. Thus $P_{\mathrm{nd}}(t)$ is larger than the exponential $e^{-\Gamma t}$ for small and large times. At

[b] also called a *Cauchy* or *Lorentz* distribution

intermediate times $P_{\mathrm{nd}}(t)$ follows an exponential law[c].

The smaller the width Γ gets, the smaller is the contribution of ω for E below $E_{\min}$ and the closer $P(t)$ resembles the exponential.

Decay Width

The half-width Γ of the distribution in Equation II.11 is called the *decay width* in the framework of decaying states. Its inverse $\tau = \Gamma^{-1}$ is the mean lifetime of the initial state and the half-life is given by $t_{1/2} = \ln(2)\,\tau$. Thus, smaller values for Γ correspond to more stable systems.

The semi-classical derivation for the probability P_T of a particle tunneling out of the bound region usually[19] gives

$$P_T = \exp(-2G) \tag{II.12}$$

where G is the *Gamow factor*[20]

$$G = \int_{r_1}^{r_2} \mathrm{d}r\, |p(r)| \tag{II.13}$$

with the semi-classical momentum $p(r) = \sqrt{2(E - V(r))}$. In order to evaluate tunneling rates, this is then correlated with the frequency associated with the particles movement: Everytime it approaches the barrier, there is a chance for it to tunnel through or be reflected. But Equation II.12 is based on the exponential decay law, from which Equation II.7 and the explanations following that showed a deviation.

In [21, 22] the decay width of a quasi-stationary state is derived with a different approach.

The derivation uses a two-potential approach and gives Γ in terms of the wave functions. For the scope of the following simulations, however, the result in semi-classical approximation should suffice without the derivation.

The result for the decay width is:

$$\Gamma = \frac{N}{4} \exp\left(-2 \int_{r_1}^{r_2} \mathrm{d}r\ \ |p(r)| \right) \tag{II.14}$$

where:

$$N^{-1} = \int_{r_0}^{r_1} \tfrac{1}{p(r)} \cos^2\left(\int_{r_0}^{r} p(r')\,\mathrm{d}r' - \tfrac{\pi}{4} \right) \mathrm{d}r \tag{II.15}$$

is the semi-classical normalization of the quasi-stationary state. The integrals are evaluated between the classical turning points as indicated in Figure II.3.

[c] These are only a few observations useful in the examination of the simulations, further aspects of non-exponential decay are given in [14] and [18].

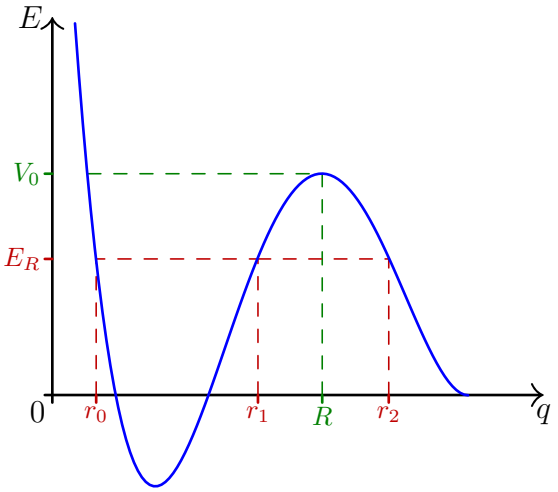

Figure II.3.: An arbitrarily chosen potential showing a local potential well with the classical turning points r_0, r_1 and r_2 for an energy E_R.

This result is of the same form as the Gamow factor (II.13), but the prefactor N is more general and applicable to low-lying states as well.

Lastly, a mentioning of Fermi's *golden rule* is in order when it comes to transition rates, like the transition here from bound to unbound states here.

The formula for a transition to a continuum of states is given in first order perturbation theory by:

$$\Gamma_{i\to f} = 2\pi \left| \langle f | \hat{H}' | i \rangle \right|^2 \rho(E_f) \tag{II.16}$$

where $|i\rangle$ and $|f\rangle$ describe the initial and final state, $\langle f | \hat{H}' | i \rangle$ is the corresponding element of the transition matrix due to the perturbation described by $\hat{H}'$ and $\rho(E_f)$ is the density of states in the continuum.

The golden rule can be recovered from the approach in [22], but Equation II.14 is easier to handle for the cases studied in the following simulations, as it involves only readily available parameters of the system.

3. Particle Capture in Potential Wells

Previously, quasi-stationary state were introduced by setting up a system where infinitely high walls were changed to a finite barrier. This is useful for analytical computations and for implementing initial values in numerics, but in regards to Daemon systems this procedure does not seem realistic. Instead, the particle is initially in a *decoupled* phase and should therefore be considered to be moving freely.

The question to be pursued here is: How can a free particle be trapped in a local potential well?

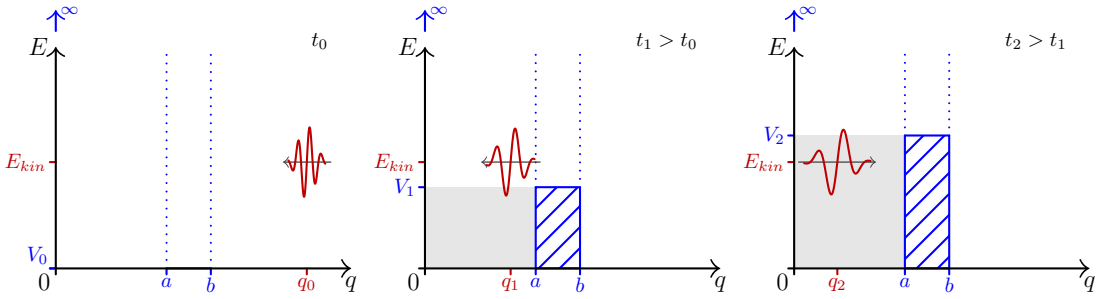

(a) t_0: initial setup

(b) t_1: particle moved over barrier

(c) t_2: barrier is now higher than the particle's energy

Figure II.4.: An illustration of trapping a particle by raising a potential barrier. The particle is indicated in red, its direction of motion by the underlying arrow. The grey area shows the region allowing for quasi-bound states.

Two ways of particle *capture* will be discussed:

1. a stationary potential barrier through which a free particle can tunnel into the well,
2. and a time-dependent potential, raising the barrier after the particle has passed it.

Approach 1 works on the basis of tunneling as discussed before, but now the initial state can be chosen freely, while tunneling is supposed to lead to a quasi-stationary state with a corresponding resonance energy.

Approach 2, as illustrated in Figure II.4, is a rather classical idea. For it to work the particle must be sufficiently localized in q in comparison to the width of the potential.

The particle can move over the barrier into the region of the potential well. The height of the barrier is increased with time and after the particle passes the barrier it should be too high to pass over again, effectively trapping the particle in the potential well. However, in quantum mechanics a particle moving over a potential barrier is still influenced by it, as Section II.b.1 will show. Therefore, a part of the wave packet is expected to be reflected by the barrier when first passing, and some part is expected to pass it later, when the barrier has been significantly raised.

In both cases the result should be a particle trapped behind barrier, that can then tunnel free, as laid out in Section II.a.2.

There is no particular theory to describe this proposed particle capture, thus at this point reference is made to the discussion of the simulations in Section II.b.3.

II.b. Simulations of Introductory Models

With the general considerations of the previous section as a basis, simple models will be introduced in this section along with numerical simulations thereof.

Numerical Scheme

First, a brief introduction into the numerical scheme used will be given. A more detailed description is given in Appendix B.i.

The numerical solutions to the Schrödinger equation $i\hbar\partial_t |\psi(t)\rangle = \hat{H}(q,t) |\psi(t)\rangle$ are computed with a *finite difference approximation* using the Crank-Nicolson method[23]. This scheme[24] is second order in time and implicit – meaning it a system of linear equations is solved at every time-step – and it is numerically stable. It operates on a discretized grid, approximating the differentials by central difference quotients.

On one end of the grid Dirichlet boundary conditions were implemented, setting the wave function to zero. In most of the models this boundary coincides with an infinitely high potential wall and $\psi = 0$ is the physically correct solution there. For the other models (*i. e.* tunneling through a barrier) the wave packets do not reach the boundaries over the course of the simulation.

The other boundary of the grid is undetermined, as no condition[d] gives the correct physical behavior of the wave function there. This leads to reflections of the outgoing wave functions back into the domain of the simulation. By choosing a large enough extent of the grid these reflections are kept from interfering with the relevant part of the model.

1. Tunneling: Scattering on a barrier

First, the behavior of a free particle encountering a localized potential barrier is simulated based on Section II.a.1. The barrier has a maximum height of V_0 and extending over a some finite width w. This leads to three different regions, as depicted in Figure II.5, with the incoming particle in I, a transmitted particle in III, and the classically forbidden region II.

The initial wave function is a gaussian wave packet:

$$\psi_0 = \psi(q, t=0) = (2\pi\Delta_q)^{-\frac{1}{4}} \exp(iqp_0) \exp\left(-\left(\frac{q-q_0}{\sqrt{2}\Delta_q}\right)^2\right) \tag{II.17}$$

with mean position q_0, an uncertainty of Δ_q in q and mean momentum p_0.

In contrast to the solutions to the Schrödinger equation in Equation II.2 describing plane waves, the wave packet is localized both in q and p. For the simulation the parameter

For the simulation two different forms of potential barriers have been chosen: a rectangular barrier (see Figure II.5a) and a barrier based on a single period of a cosine (see Figure II.5b), referred to as the *cosine* or *pendulum*-potential (in connection to the quantum pendulum examined in the next part of this section).

The barriers are defined on a region of q bounded by a parameter a:
$B = \{\, q \mid -a \leqslant q \leqslant a \,\}$.

[d] except for transparent boundary conditions, see also Appendix B.iii

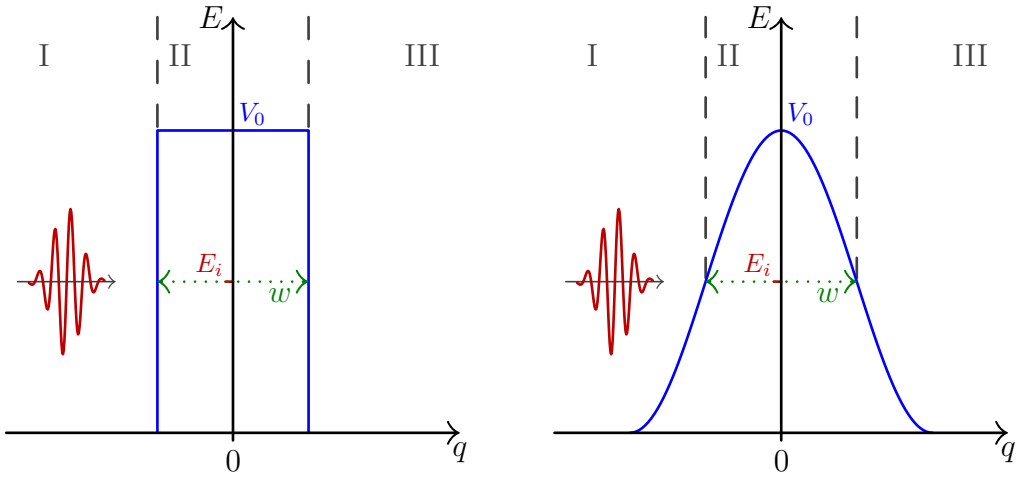

(a) rectangular barrier (b) cosine barrier

Figure II.5.: The two types of barrier used in the tunneling simulations: *(a)* rectangular and *(b)* cosine barrier.
The outline of the barrier with height V_0 is in blue. The width (at $\frac{1}{2}V_0$) is given in green. The red wave form indicates the incoming particle with energy $E_i = \frac{1}{2}V_0$. Additionally marked are the regions in roman numerals.

The rectangular barrier is approximated by a flat-topped gaussian function and defined as:

$$V_{\text{rect}} = V_0 \exp\left(-\left(\frac{q}{0.5\,w}\right)^{128}\right), \quad q \in B, \tag{II.18}$$

with height V_0, width w and boundary $a = \frac{1}{2}w$.

The cosine-barrier is defined as:

$$V_{\cos} = \tfrac{1}{2}V_0\left(\cos(\tfrac{\pi}{w}q) + 1\right), \quad q \in B, \tag{II.19}$$

where V_0 again defines the height and w gives the half width of the cosine at $\frac{1}{2}V_0$, with boundary $a = w$.

The computations have been done for different sets of parameters: V_0 fixed with three different widths w each for the two barriers. Figure II.6 shows the results for these examples, where the parameters were chosen so that the plots are comparable between both barriers.

There is no significant difference between both barrier types in the qualitative behavior. The incoming wave packet moves towards the barrier, where it is partly reflected, while also partly tunneling through the barrier and subsequently moving away from the barrier on the other side. The wave packet widens over time, regardless of which path it takes.

The apparent holes in ρ for $q < \frac{1}{2}w$ stem from the superposition of the slow part of the incoming part of the wave packet with the fast part of the reflected one. This

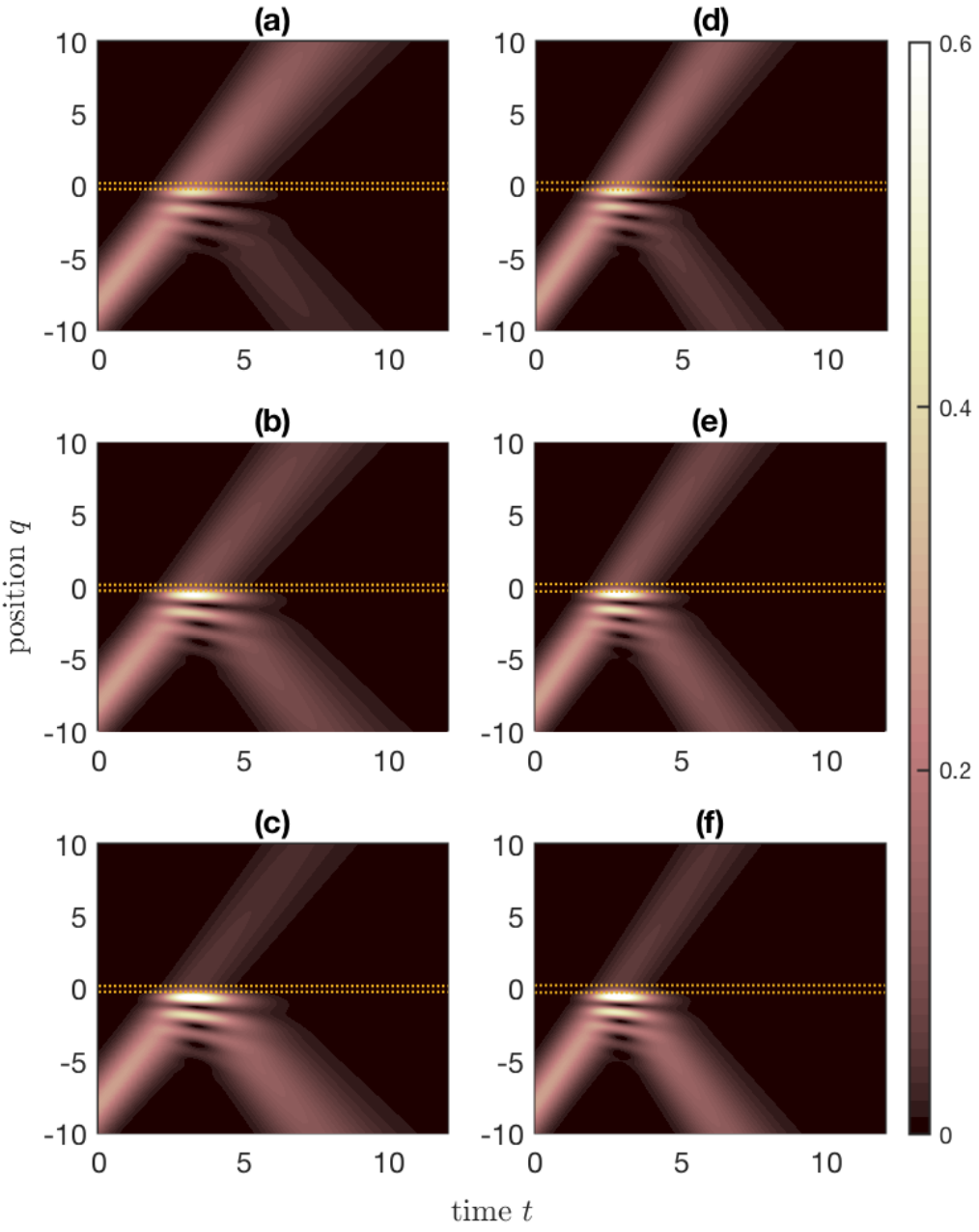

Figure II.6.: The probability density $\rho(q) = |\psi|^2$ of the tunneling model for two barriers and three sets of parameters each. The dotted yellow lines mark the width w of the barrier (compare Figure II.5) and thus indicate the position of the barrier.
For the initial state the parameters $q_0 = -8$, $\Delta_q = 2$ and $E_i = \frac{1}{2}V_0$, thus $p_0 = \sqrt{V_0}$, were chosen.
left: rectangular barrier, $V_0 = 6$; (a) $w = 0.2$, (b) $w = 0.4$, (c) $w = 0.6$
right: cosine barrier, $V_0 = 8$; (d) $w = 0.2$, (e) $w = 0.35$, (f) $w = 0.5$

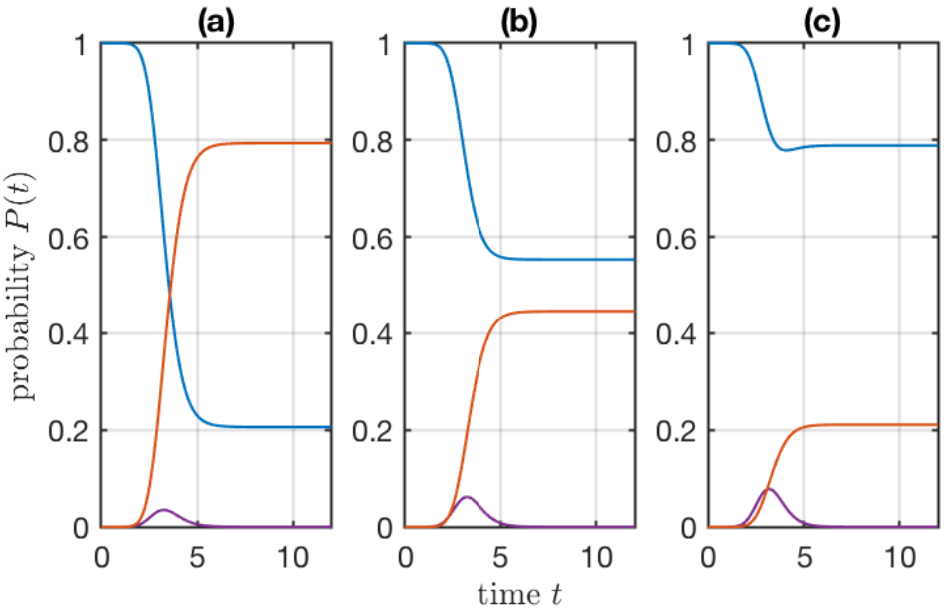

Figure II.7.: Probabilities to localize the particle in the different regions of the systems; blue: $q < -a$, purple: $-a \leqslant q \leqslant a$, orange: $q > a$. The parameters correspond to (a)-(c) of Figure II.6 (left column). For later times the orange (blue) curve shows the probability for transmission (reflection).

is similar to Equation II.2. In the region $q > \frac{1}{2}w$ there is only the transmitted wave packet, hence no interference occurs.

The probability to locate the particle in certain regions of the system is given in Figure II.7 for the rectangular barrier. The curves were computed by numerically integrating the wave function over the three distinct regions: $q < -a$ for reflection, $q > a$ for transmission and $-a \leqslant q \leqslant a$ for the barrier. In the beginning the wave packet is located on one side (blue), but it can be transmitted to the other side (orange) during barrier interaction. The purple curve rises and falls, corresponding to the wave packet passing through the barrier region. After the barrier interaction is over, it falls back to zero. The other curves remain at stationary values, too, and the probability for reflection $P_R = |\mathcal{R}|^2$ and transmission $P_T = |\mathcal{T}|^2$ can be obtained. The relation of the amplitudes $\mathcal{R}$ and $\mathcal{T}$ depends on the barrier parameters, in this case w. The dependence on the height is implicitly contained in the relative energy $\mathcal{E} = \frac{E_{kin}}{V_0}$.

Figure II.8 shows the results for different initial energies $\mathcal{E}$ for a barrier of fixed width and height. The transmission probability grows for larger energies, as would be expected. But for $\mathcal{E} = 1$ there is still a chance for reflection $P_R > 0.3$, and $P_R < 0.01$ is only achieved for $\mathcal{E} \geqslant 4.2$. The reason for this behavior is the distribution around the particle's mean energy, giving a decent probability for the actual energy value to be lower than the V_0 even for $\mathcal{E} > 1$. Only with a high energy of the incident particle the part of the distribution below V_0 is negligible.

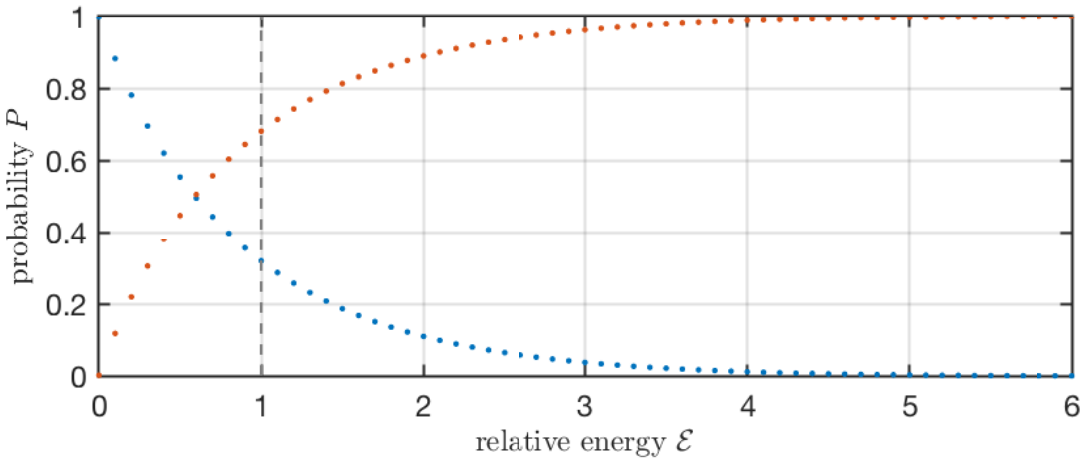

Figure II.8.: Probability for transmission (orange) and reflection (blue) in relation to the relative kinetic energy for the case of a rectangular barrier with $V_0 = 6$ and $w = 0.4$. The dashed grey line indicates an initial energy higher than the barrier.

This simulation therefore shows behavior not possible in classical mechanical systems: A particle with an initial relative energy $\mathcal{E} < 1$ can move through a classically forbidden region and move on beyond the barrier. For $\mathcal{E} > 1$ the barrier is still not fully opaque, with considerable probability for reflection remaining. This means that the barrier influences the particle, even if it would classically move above the barrier unobstructed.

Both of these features can be explained by the uncertainty principle, a distinctive trait of quantum systems due to the probabilistic description of quantum systems. These features, however, also show the description of particles in terms of wave functions, as is inherently given by the solutions of the Schrödinger equation.

In conclusion, this introductory simulation shows the features of quantum systems expected from the study of these textbook examples.

2. Decay of Quasi-Stationary States

Next, the time-evolution of the quasi-stationary state introduced in Section II.a.2 is examined in simulations. Again, two types of potential are considered here: the rectangular barrier as an easy example and the cosine-potential of the quantum pendulum in preparation of the Daemon system.

Analytical expressions for the decay width Γ can be found for the rectangular barrier, this is derived in Appendix C.ii, and the cosine barrier in terms of elliptic integrals. However, expressions II.14 and II.15 are evaluated numerically, since this is necessary anyway if an additional tilt is introduced in the cosine-potential.

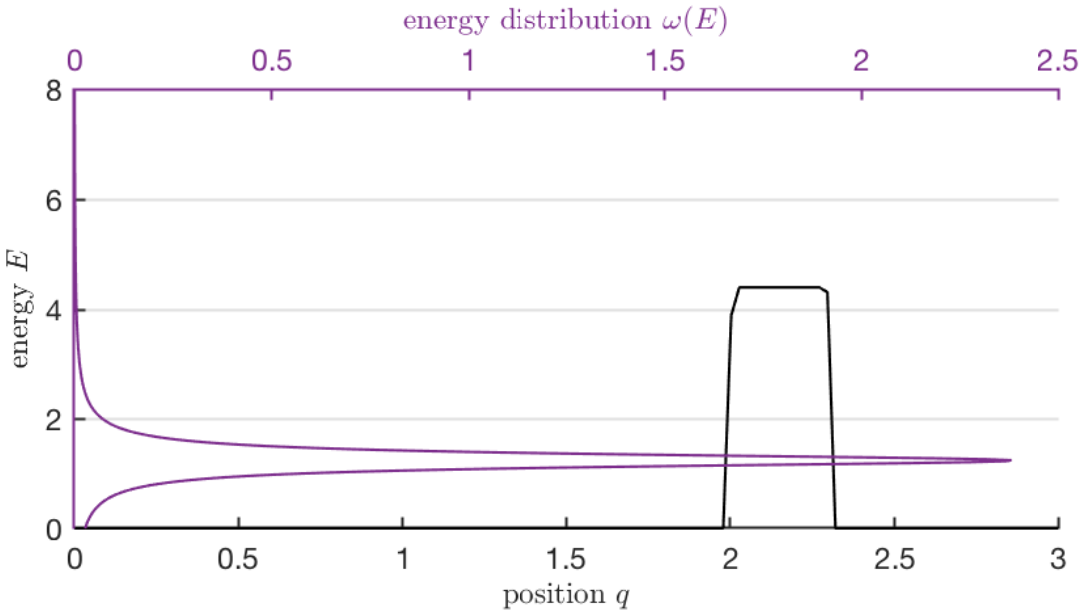

Figure II.9.: An example of the actual rectangular potential barrier (black) used in the simulations, approximated by a flat-topped gaussian function. Also shown is the energy distribution $\omega(E)$ (blue) of the initial state.

Rectangular Potential Barrier

The basic setup for this system is illustrated in Figure II.2a. The initial state of this problem is given by the n-th eigenstate of a particle in a box[16]:

$$\psi_0 = \sqrt{\frac{2a}{\pi}} \sin\left(\frac{n\pi}{a} q\right), \tag{II.20}$$

with the corresponding eigenenergy (or resonance energy E_R)

$$E_n = \frac{1}{2}\left(\frac{n\pi}{a}\right)^2 (= E_R), \tag{II.21}$$

where the lowest energy for $n = 1$ was chosen in the simulation.

The rectangular steps of the potential are approximated by using a flat-topped gaussian function:

$$V = V_0 \exp\left(-\left(\frac{q}{0.5\,w}\right)^{128}\right) \tag{II.22}$$

and is thus continuous everywhere. The infinitely high wall at $q = 0$ is achieved by the boundary condition $\psi|_{q=0} = 0$.

The actual potential for the particular set of parameters is given in Figure II.9, overlain with the energy distribution function $\omega(E)$. It shows a distinct portion of the distribution pertains to an energy value $E > V_0$.

The time-evolution of the system is shown in Figure II.10, given by the probability density $\rho(q) = |\psi|^2$, together with the non-decay probability $P_{\mathrm{nd}}(t)$. This was numerically obtained by integrating $|\psi|^2$ over the region of well ($q < a$). The analytical curve is defined by Equation II.7, which was evaluated numerically. For comparison, the exponential form $\exp(-\Gamma t)$ is shown as well.

For the bound particle in the well oscillations in the density can be observed. With every approach to the barrier a portion of the distribution can be seen to emerge beyond the barrier, moving away in a straight line as a free particle. As a result, the probability to find the particle in the well decreases. The intensity of the oscillations decreases as well, indicating a reduce in mean energy. This is also indicated by the emerging flow. The time needed to reach the edge of depicted domain increases, indicating a decreasing momentum.

The non-decay probability in Figure II.11 reflects this. The simulated (blue) curve's behavior over time relates to the oscillations: the decrease accelerates when the maximum of the distribution approaches the barrier. With less prominent oscillations, the curve becomes smoother.

For small times, the probability deviates significantly from the exponential $\exp(-\Gamma t)$. The analytical curve of Figure II.11, is initially higher than the exponential and then approaches it. The simulated probability resembles this closely for small times. It then drops corresponding to an approach of the oscillation and deviates further from the analytical curve, but closer to the curve of the Phase-Space Evolution (green). It is slightly below the exponential for a brief time, but slows its decline, corresponding to the absence of strong oscillations, and stays above the analytical curve for the remainder of the simulated time span. The probability of the Phase-Space evolution resembles this behavior, but at higher values. In the end, both numerical curves approach the analytical one.

The simulation shows the predicted behavior for initial and intermediate times, with the probability higher than the exponential and approaching it. The behavior for larger times could not be studied, since the simulation did not cover a long enough time axis.

In addition to $\psi(q)$, wave functions $\phi(p)$ in momentum representation can be gained via Fourier transform. The momentum probability density $\sigma(p) = |\phi|^2$ is depicted in Figure II.12a alongside the corresponding plot of the quantum pendulum model.

Initially the momentum is distributed around $p = 0$, with bounds around $p \simeq \pm 1.8$. Early on a bulk flow of the distribution forms, focussed around $p \simeq 0.65$. This represents the particle leaving the well and moving away freely. There is a rather sharp upper bound around $p \simeq 1.5$, slowly decreasing to $p \simeq 1.4$ over time. From this bound smaller streaks of the distribution form, which curve towards the bulk flow asymptotically. This indicates a movement of the particle over the barrier with high enough momentum, which is possible due to the uncertainty principle.

Beyond this boundary, at higher momentum, there is one more faint flow, superposed with an extension of the lesser streaks, around $p \simeq 2$ and narrowing in momentum over

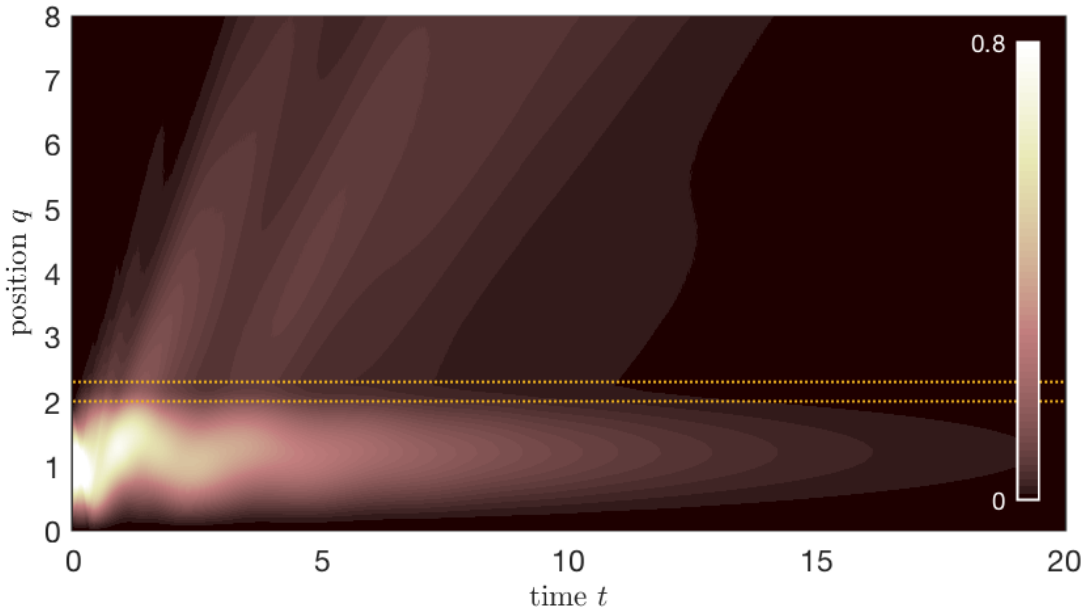

Figure II.10.: The spatial probability density $\rho(q) = |\psi(q)|^2$ for the rectangular barrier with parameters $a = 2$, $w = 0.3$ and $V_0 = 4.4$, resulting in $\Gamma = 0.27$, $\mathcal{E} = 0.28$. The dotted yellow lines indicate the position of the barrier between a and $b = a + w$.

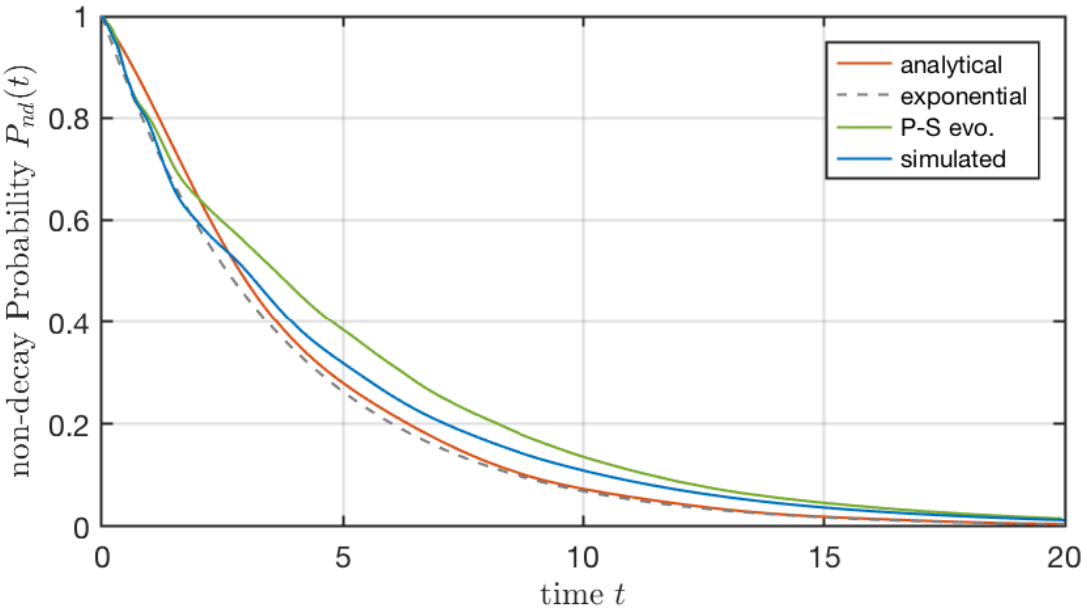

Figure II.11.: The non-decay probability from simulations and analytical computation with the exponential $e^{-\Gamma t}$ for comparison.
The additional green curve from a numerical simulation with the Phase-Space Evolution scheme discussed in Section III.c.2.

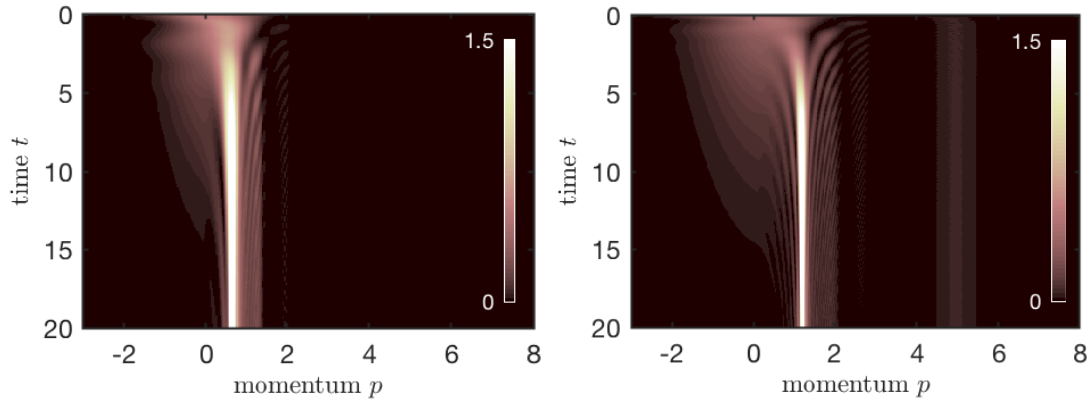

(a) rectangular barrier (b) cosine barrier

Figure II.12.: Probability densities $\sigma(p) = |\phi(p)|^2$ for the decay models. The wave functions $\phi(p)$ in momentum representation where obtained via fast Fourier transforms of the numerical wave functions presented in Figure II.10 and II.14.

time.

The lower bound of the main part of the distribution slowly rises, crossing $p = 0$ at $t \approx 15$. After that the probability for negative momentum of an oscillating bound particle is marginal. From this lower part of σ form additional lesser flows at lower values of p, one around $p \simeq 0.4$ and another around $p \simeq 0.2$, indicating a reduction in the momentum of the tunneled particle over time.

The comparison to ρ in Figure II.10 shows the the same aspects of the behavior, since they are based on the exact same data, but with a different portrayal. σ shows the initial relaxation phase with a broad spectrum in p and signs of oscillations in the lower part of σ. From this emerges then a more stationary flow pattern for later times, which shows streams of varying p forming at different times, indicating the tunneling of high energy first.

The system's behavior can be characterized appropriately by the two quantities Γ, giving all information about the system, and $\mathcal{E}$, describing the particle within the system. This also means that any change in a system parameter can be seen as a change in Γ or $\mathcal{E}$, since the height and width of the barrier directly influence Γ via the definition in II.14.

Single-Well Quantum Pendulum Potential

The second decay model is determined by the potential function

$$U(q) = \gamma \left(\cos\left(\tfrac{2\pi}{R}q\right) + 1\right) \tag{II.23}$$

hereafter called the *cosine-* or *quantum pendulum*-potential.

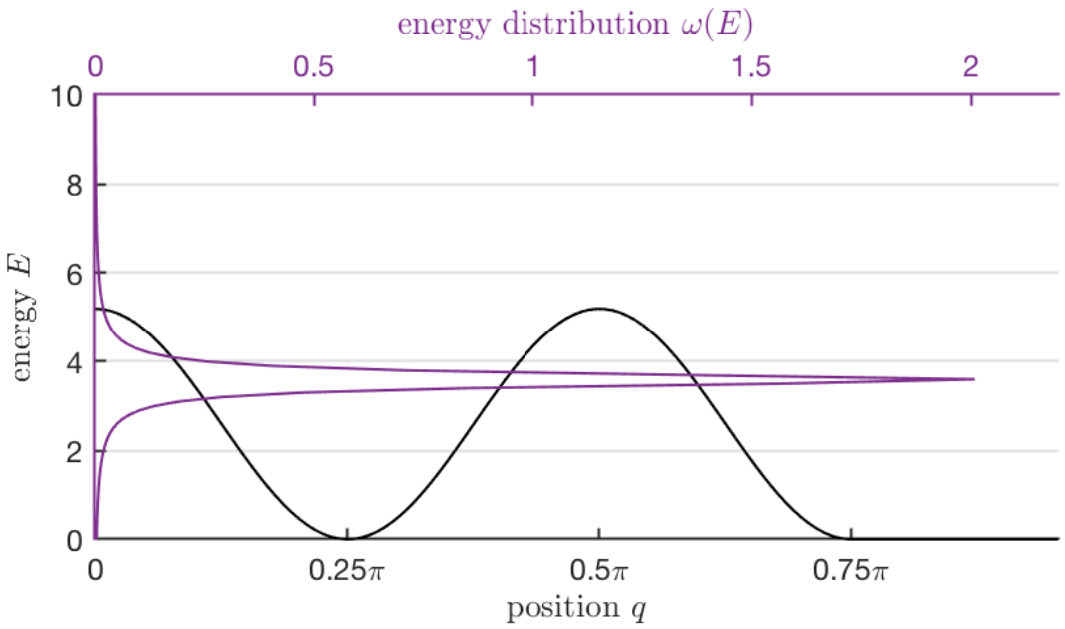

Figure II.13.: An example of the single well quantum pendulum potential barrier used in the simulations. Also shown is the energy distribution $\omega(E)$ of the initial state.

From this, the well and barrier, and the complete potential, follow as:

$$V(q) = \begin{cases} \infty, & q \leqslant 0, \\ U(q), & 0 < q \leqslant b = \frac{3}{2}R \\ 0, & \text{else} \end{cases} \tag{II.24}$$

This is reduced to a single well with an infinitely high wall to one side and a barrier of limited extend, depicted in Figure II.13. The maximum depth of the well is given by $V_0 = 2\gamma$, the maximum width by a.

For the initial state and resonance energy, an excursion to the mathematical description of the quantum pendulum[25] is needed, which is given in Appendix C.i. The resulting eigenfunctions are special functions[26]: the Mathieu sine se_{2m} and cosine ce_{2m} of even order. These do not have an analytical representation. They are implemented with [27]. The wave function (see Equation C.5) corresponding to $n = 2m = 2$ was chosen as the initial solution.

The potential barrier, shown in Figure II.13, is implemented according to Equation II.24. The initial wave function is defined between the turning points r_0 and r_1 (as given in Figure II.2b) and appropriately shifted.

The result of a simulation is shown in Figure II.14. The parameters were chosen such that the decay width ($\Gamma = 0.28$) is close to that of the rectangular barrier ($\Gamma = 0.27$). Both simulations show very similar behavior. Oscillations can be observed again, but

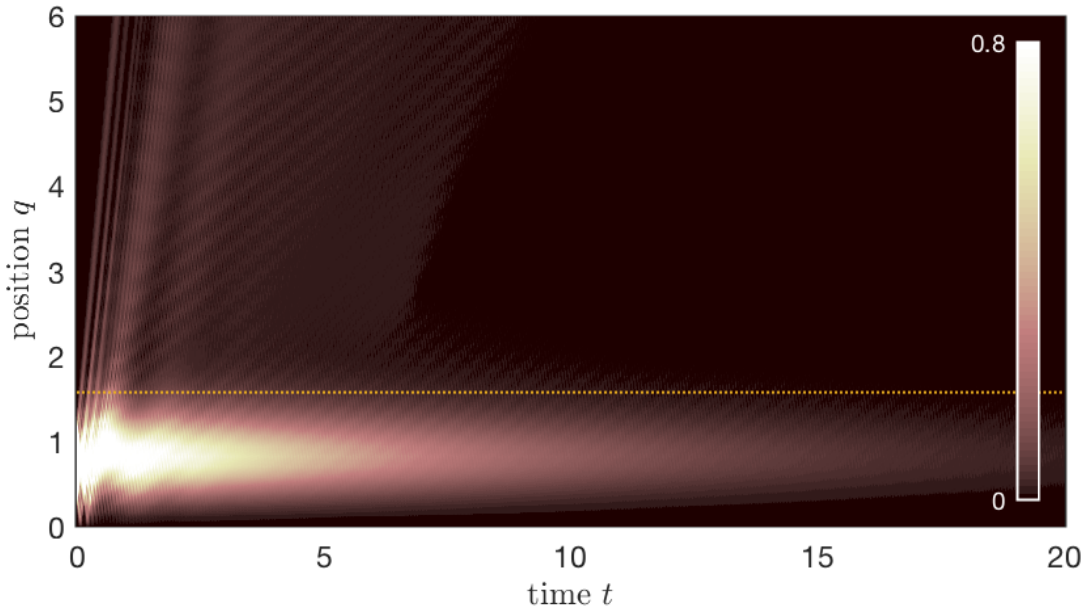

Figure II.14.: The spatial probability density $\rho(q) = |\psi(q)|^2$ for the cosine barrier with parameters $a = \frac{\pi}{2}$, $b = \frac{3}{4}\pi$ and $V_0 = 5.2$, resulting in $\Gamma = 0.28$, $\mathcal{E} = 0.69$. The dotted yellow line indicates the maximum of the barrier a an thereby the maximum width of the well R.

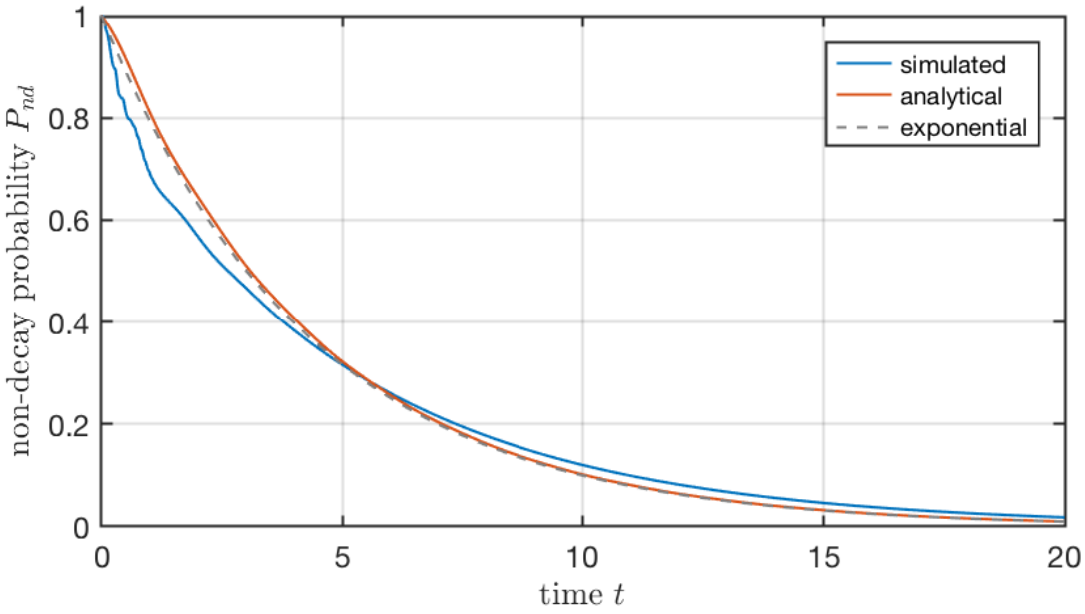

Figure II.15.: The non-decay probability from the simulation and analytical computation with the exponential $e^{-\Gamma t}$ for comparison.

they are less prominent and disappear sooner.

In this model the well is less wide for lower energies, so the available space for the particle decreases along with the energy over time. The edge of the distribution along the barrier is thus less sharp compared to the edge towards the wall (at $q = 0$) or the rectangular model.

The streams of probability move away from the well show at a higher momentum due to the higher resonance energy of the quasi-stationary state. They disappear from the plot – due to the color scale – earlier than in the rectangular model. In addition, these streams, as well as the blurred edge of the distribution, exhibit stripes due of interferences of different parts of the wave function.

For this model the momentum distribution $\sigma(p)$ was computed as well via Fourier transform. The result is depicted in Figure II.12b. The distribution again shows a main part with flows branching off, but there are also additional flows at higher momentum. The bulk is centered around $p \approx 2.4$ and appears to form more directly out of the initial distribution. The bounds of the distribution are $p \simeq \pm 2.1$. The lower part rises quicker and forms more of the lesser streaks.

The second large flow forms right after $t = 0$ and shows as a wide straight line centered around $p \approx 5.0$. This corresponds to the lines in Figure II.14 that lead away from the well right in the beginning.

A third flow can be seen around $p \simeq 2.5$. It is superposed with lesser streaks forming close to the upper bound of the main part.

The non-decay probability shows the same overall behavior as before in the rectangular model, but the simulated curve drops considerably faster in the beginning compared to the two other curves. For intermediate times the decline is slower and the curve is only slightly above the exponential.

3. Capture of a Particle in a Potential Well

This section is concerned with obtaining quasi-bound states. Presented here are simulations of the two approaches of particle capture described in Section II.a.3. In both cases the initial wave function is given by the wave packet of Equation II.17 with parameters $q_0 = 8$ and $\Delta_q = 2$, located outside the potential well and moving towards it.

Particle Capture Through Tunneling

The first approach is about a free particle tunneling through a barrier into a potential well. This system has the same setup as the decay model in Section II.b.2, with the barrier given by Equation II.22.

The simulation has been performed for two cases which vary only in the the initial momentum – and thereby energy – of the particle: the resonant case, where the particle's energy matches the resonance energy of the well[e] $\mathcal{E} = 0.28$, and a non-resonant case, where $\mathcal{E} = 0.40$.

[e] More precisely, the expectation value of the kinetic energy of the initial wave function matches the

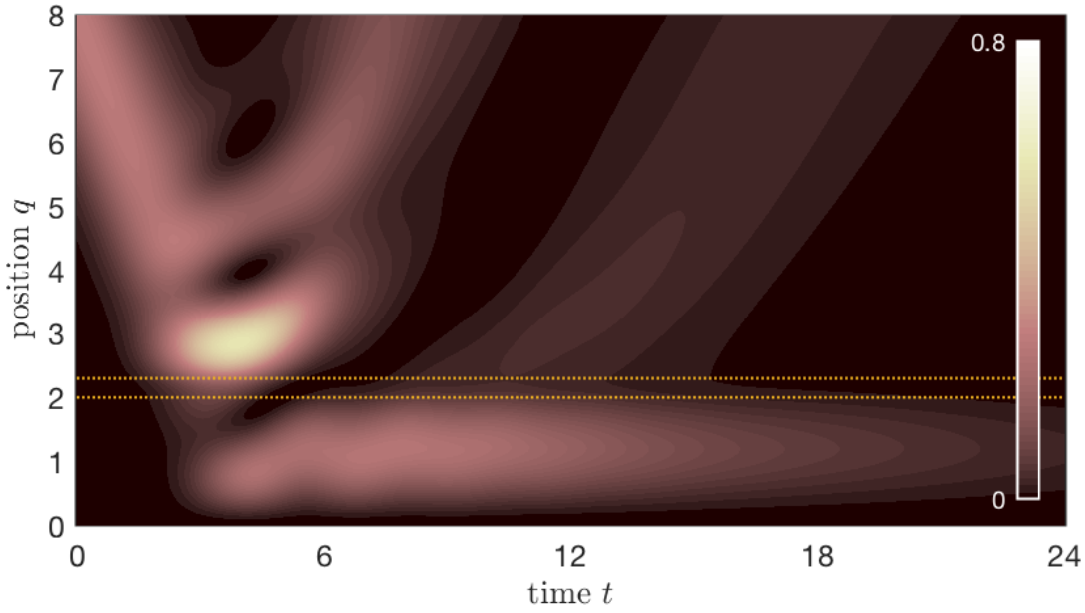

(a) resonant case

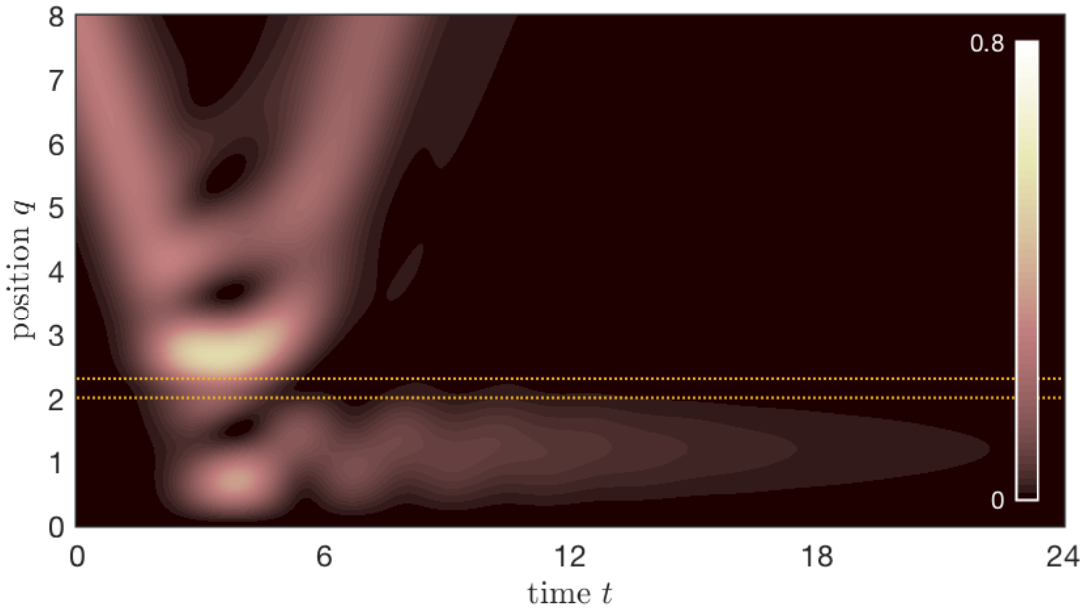

(b) non-resonant case

Figure II.16.: Tunneling of a particle through the rectangular barrier into a potential well with $V_0 = 4.4$ and $w = 0.3$, the same parameters as in Figure II.10. In (a) the initial energy is $\mathcal{E} = 0.28$ ($p_0 = -\frac{\pi}{2}$), equal to the well's resonance energy E_R of the rectangular decay model. In (b) the relative initial energy is $\mathcal{E} = 0.4$ ($p_0 = -1.88$). The dotted yellow lines indicate the position of the barrier between a and $b = a + w$.

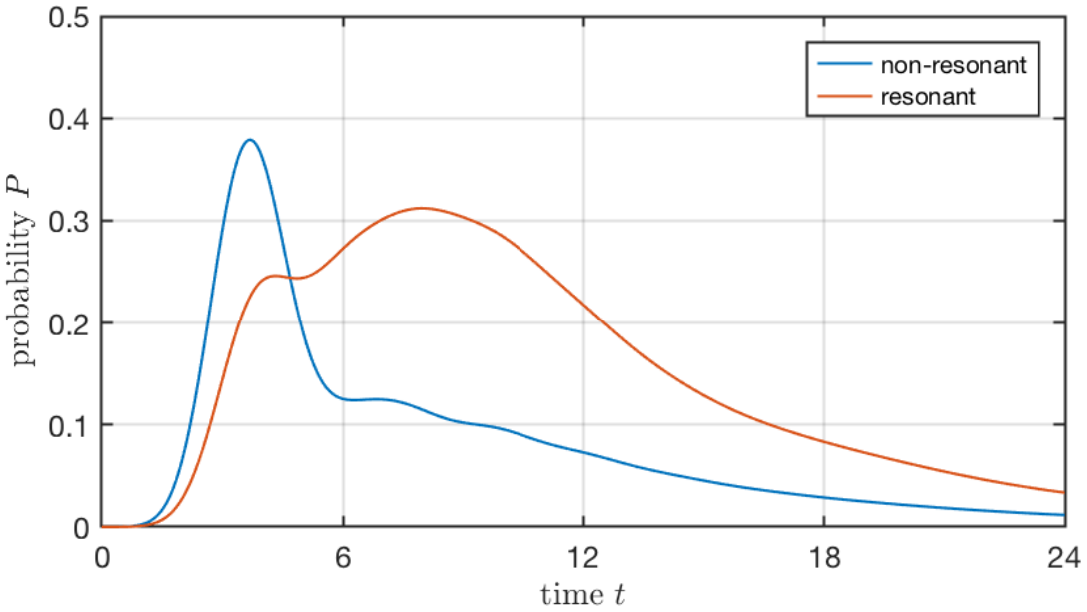

Figure II.17.: Probabilities in the raising-barrier model to localize the particle within the well, *i. e.* for $q < a$. The blue curve corresponds to the non-resonant case, the orange one to the resonant case.

The resulting probability densities $\rho(q)$ are depicted in Figure II.16. Additionally the probability to locate the particle within the region of the well, *i. e.* $q \in [0, a]$, was computed via numerical integration. The results are shown in Figure II.17.

Both cases exhibit a very similar time evolution. The particle moves towards the barrier. There it is either reflected and moves away, or it is transmitted through the barrier and into the well, possibly resulting in a trapped particle. This trapped particle bears a great resemblance to the quasi-stationary decay (compare Figure II.10 and II.11). The density in the well diminishes over time and the probability curves show a downward slope similar to the non-decay probability of the decay model, starting around $t = 7$ for the non-resonant case, or around $t = 8$ for the resonant one. This indicates a particle tunneling out of the well. Also, oscillations occur in the density in the well at least for a short time.

These two cases also show some differences. With the initial momentum chosen to be different, the particle in the non-resonant case encounters the barrier earlier and has a sharper angle between the incoming and the reflected parts of the distribution. This is also discernible in the probabilities, where the non-resonant curve shows an earlier rise.

The density values in the well are higher in the resonant case. The probability reflects this. While the peak value is higher in the non-resonant case, the resonant case shows a higher probability over a longer period of time, which corresponds to the higher

eigenenergy (see II.21) corresponding to the initial quasi-stationary state in the rectangular decay model of Section II.b.2.

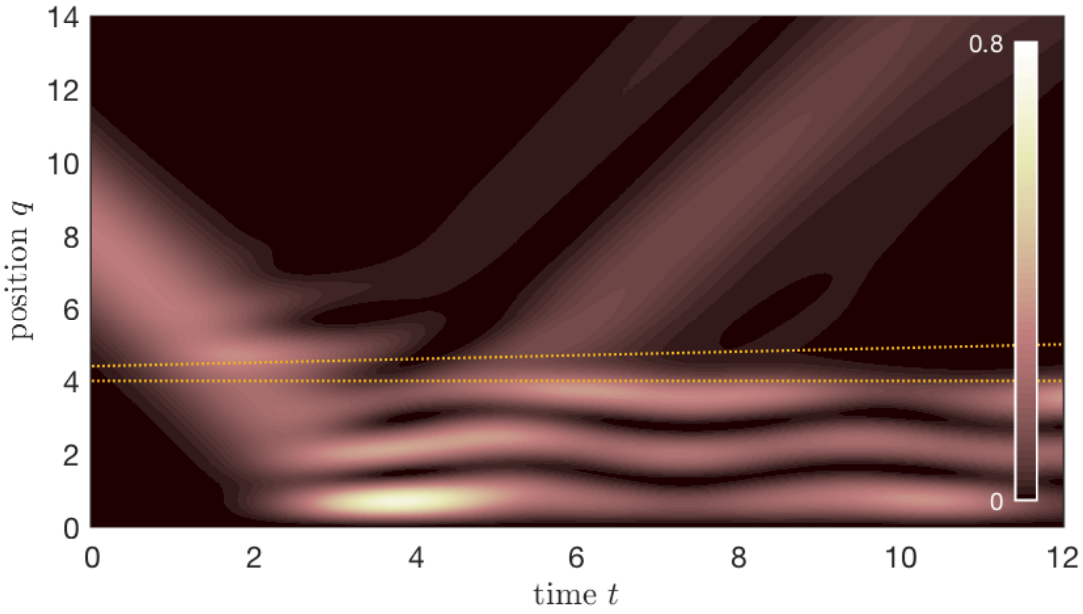

Figure II.18.: Time evolution of the probability density ρ for a wave packet encountering a rectangular potential barrier that rises with time. The system parameters are: $a = 4$, $w_i = 0.4$ to $w_f = 1$, $V_i = 0$ to $V_f = 12$, $E_{\text{kin}} = 0.31$ ($p_0 = -0.79$). The dotted yellow lines indicate the position of the barrier between a and $b = a + w$ and shows the increasing width.

probability density values.

Another difference is apparent in the resonant case: ρ shows a flow of the distribution, emanating from the barrier approximately in the time period $t \in [8, 15]$. This, again, indicates the possibility for the particle to tunnel out of the well. The probability curve shows a greater change for the resonant case in this time period, whereas the non-resonant case shows a much slower change in the similar time period $t \in [7, 14]$. To clarify, in both cases the particle can and will tunnel out once it is trapped. But the resonant case has a higher probability to capture the particle, making the change in the probability over time more visible.

These two examples show that in principle the capture of a particle in a potential well is possible. The probability for capture is dependent on the energy in relation to the system parameters, as is the general probability for tunneling through a barrier. On the basis of these simulations, the trapped particle appears to be quasi-bound. It will tunnel out of the well at some point.

Particle Capture Behind a Raising Barrier

The second approach utilizes a (rectangular) time-dependent potential that raises a barrier from height $V_i = 0$ to a finite value $V_f = 12$, which is high compared to the kinetic energy of the particle, while also increasing the width from $w_i = 0.4$ to $w_f = 1.0$. Both

of these processes are linear. In this case, the well itself is wider in order to facilitate the particles movement through the well to wall and back, without having to raise the barrier too rapidly. The wider barrier reduces the probability of the particle to tunnel through it further.

The particle encounters the barrier first at a low height. It can move over the barrier, but is also partly reflected by it, as can be seen in the tunneling model of Section II.b.1. After crossing the well, the particle is reflected and moves back towards the barrier. This time, it is higher and the particle is mostly reflected, being now trapped inside the well. This time evolution is shown in Figure II.18, effectively portraying a superposition of a particle being reflected by a barrier or the wall, and a bound particle in a wide well. The resulting quasi-bound state is less likely to decay, the higher the barrier rises.

III. The Example Models in Phase-Space

The aim of this chapter is to establish a phase-space formulation of quantum mechanics for the examination of daemon systems, utilizing Wigner functions. Furthermore two different methods[a] are introduced to examine such Wigner functions and their time evolution numerically.

Section III.a gives a short overview of the theoretical framework. The basic definitions and equations used throughout the following chapters are introduced.

Section III.b shows the results of the first numerical method. The wave functions from the previous chapter to are transformed to the corresponding Wigner functions in phase-space.

In **Section III.c** the second numerical method is derived and examined. The time evolution of Wigner functions is determined solely on the basis of the phase-space description. Results are given for selected models of the previous section.

Lastly, **Section III.d** compares the the two methods and their possible uses.

III.a. Quantum Mechanics in Phase-Space

1. Short Review of Phase-Space Quantum Mechanics

A formulation of quantum mechanics would be useful, but the canonical quantization does not allow it because of the incommensurability of position and momentum. This problem is circumvented in the *Weyl-Wigner-Groenewold-Moyal*-formalism (WWGM).

It is an consistent and autonomous quantization procedure, that delivers a description of quantum theory in terms of c-number functions in phase-space with position and momentum as coequal variables instead of operators on a Hilbert space.

The cornerstone is the *Wigner function*[28]:[b]

$$W[\psi](q,p) = \frac{1}{2\pi}\int \mathrm{d}y\, \psi^*\left(q-\frac{\hbar}{2}y\right) e^{-iyp}\,\psi\left(q+\frac{\hbar}{2}y\right). \tag{III.1}$$

[a] Figure III.14 shows a schematic overview of the relations between equations, numerical schemes and results.

$W(q,p)$ acts as a probability distribution of a state in phase-space, but it can also take on negative values in small areas. It is therefore also referred to as the *Wigner quasi-probability distribution*. The discrete version of the Wigner transform (Equation III.1) will be called the *Wigner-Ville*-transform here, in accordance with its use in signal processing.

Some useful properties[29] of Wigner functions are:

- The marginal probability densities are given by:

$$\int \mathrm{d}p\, W(q,p) = \rho(q), \tag{III.2a}$$

$$\int \mathrm{d}q\, W(q,p) = \sigma(p). \tag{III.2b}$$

- The probability over an area Ω in phase-space is:

$$P = \iint_{\Omega} \mathrm{d}q\, \mathrm{d}p\, W(q,p). \tag{III.2c}$$

- W is normalized to 1 (for normalized wave functions).
- W is real.

The composition of phase-space functions is given by the $\star$-product[30]:

$$\star \equiv \exp\left(\frac{i\hbar}{2}\left(\overleftarrow{\partial_q}\overrightarrow{\partial_p} - \overleftarrow{\partial_p}\overrightarrow{\partial_q}\right)\right). \tag{III.3}$$

The *Weyl-correspondence* mediates between phase-space functions and operators:

$$\begin{aligned} F(q,p) &\leftrightarrow \hat{F}(\hat{q},\hat{p}), \\ F(q,p) \star G(q,p) &\leftrightarrow \hat{F}(\hat{q},\hat{p})\,\hat{G}(\hat{q},\hat{p}). \end{aligned} \tag{III.4}$$

The mapping of operators onto phase-space functions is the Wigner-transform, its inverse is called the Weyl-transform.

The dynamic evolution of a function f in phase-space is specified by the *Moyal equation*[31]:

$$\partial_t f = \frac{1}{i\hbar}\left(H \star f - f \star H\right) \equiv \{\{H,f\}\}, \tag{III.5}$$

where $\{\{\cdot,\cdot\}\}$ describes the Moyal bracket.

Moyal's equation extends the Liouville equation $\partial_t f + \{f,\mathcal{H}\} = 0$ for a classical Hamiltonian $\mathcal{H}(q,p)$ to quantum mechanics.

[b] This is based on the wave functions. For the transform of the density operator, see Section A.i (Equation A.2).

2. About Tunneling in Phase-Space

At this point, a review of the theory concerning quantum tunneling in phase-space would be in order. However, researching the available literature shows that there is no closed theory.

Reference [32] features a brief review of the literature and the various methods therein and points to numerous further references. It can be used as a starting point. Most publications focus on specific problems (*e. g.* barrier types) or take the asymptotic approach of scattering theory. Both features are not particularly useful here.

On a classical phase-space, the time evolution of distribution functions obeys the *Liouville* equation and can be described as an incompressible flow along the trajectories, in accordance with Liouville's theorem. Moyal's equation contains the Liouville equation as an approximation in the zeroth order and extends it through higher orders of $\hbar$, adding the quantum corrections. On the quantum phase-space the flow of a distribution can thereby not be considered incompressible and does not necessarily follow the trajectories. Distributions can spread in accordance with the uncertainty principle and can flow across trajectories, possibly into classically forbidden regions.

Further considerations concerning quantum tunneling are discussed in the context of the following simulations.

Overview for the Presentation of Results

The following sections III.b and III.c will examine Wigner functions of the various models.

Additionally the marginal distributions $\rho(q)$ and $\sigma(p)$ and the probability P_Ω over a phase-space region Ω can be obtained from $W(q,p)$ through integration.

$\rho(q) = |\psi(q)|^2$ was a subject of the previous chapter and $\sigma(p) = |\phi(p)|^2$ was shown for the two decay models.

Not every method will be used for every system, but rather where they are informative.

The models of rectangular tunneling and barrier raising will serve as test cases, with ρ and σ shown for each models with both numerical method.

In addition to the marginal distributions the probability will be discussed for the barrier raising model because it features a time-dependent separatrix that confines a phase-space region Ω both in q and p.

A probability curve computed with the Phase-Space Evolution scheme was already shown in Figure II.11 for comparison. A discussion thereof will be picked up in the context of the numerical scheme and the resulting Wigner function.

III.b. Revisiting the Introductory Models in Phase-Space

In this section the wave functions of the previous chapter are transformed with the Wigner-Ville[33] transformation[c], which is directly based on Equation III.1 and utilizes a *fast Fourier transform* (FFT) algorithm to expand the one-dimensional problems to the two-dimensional phase-space.

The models therefore use the same parameters and initial states as the Crank-Nicolson simulations.

The depictions of the Wigner functions feature additional trajectories, based on the classical relation $p_{\pm}(E,q) = \pm\sqrt{2(E-V(q))}$ for arbitrary energies E, with the separatrix $p_{\pm,\mathrm{sep}}$ for $E \equiv V_{\max}$. These trajectories are on accordance with the the Liouville equation and are hence regarded as first order approximations of the Moyal equation. The higher order terms in the quantum evolution can lead to deviations from the classical trajectories.

1. Barrier Penetration

For these simulations the Gaussian wave packet of Equation II.17 was chosen as a representation of the free particle because of its minimal uncertainty. In phase-space this has the additional benefit that it transforms into a superposition of Gaussian distribution in q and p.

The time evolution is shown in Figure III.1, given by six plots at different times. The classical trajectories take the form of straight lines up to the barrier, where they go to zero and almost coincide with the separatrices. Because of the Gaussian form of the barrier the trajectories are densely packed there, but do not overlap.

As the initial Gaussian distribution moves towards the barrier it slightly deforms due to different traveling speeds, which is how the spreading of a wave packet presents in phase-space.

As the foremost part of the distribution encounters the barrier it spreads to higher and lower momenta along the edge of the barrier. Additionally a pattern of lines with alternating positive and negative values starts to show around $p = 0$ to the left (incoming side) of the barrier.

A part of the distribution is reflected, stretching along the separatrix to negative momenta. But another part is transmitted through the barrier, seemingly ignoring the separatrix. As the transmitted part moves away, the stripe pattern occurs on the right side as well.

Two bulks of distribution emerge from the barrier, one with positive momentum on the right side representing a tunneled particle and one with negative momentum on the left side representing a reflected particle. Both move freely away from the barrier. The pattern of lines centered around $(q,p) = (0,0)$ persists as an interference pattern of the two distributions indicating a superposition[d] of both possibilities.

[c] For more information on the implementation, see Appendix B.iii.

[d] Such an interference can be seen in [28] for a pair of Gaussian wave packets.

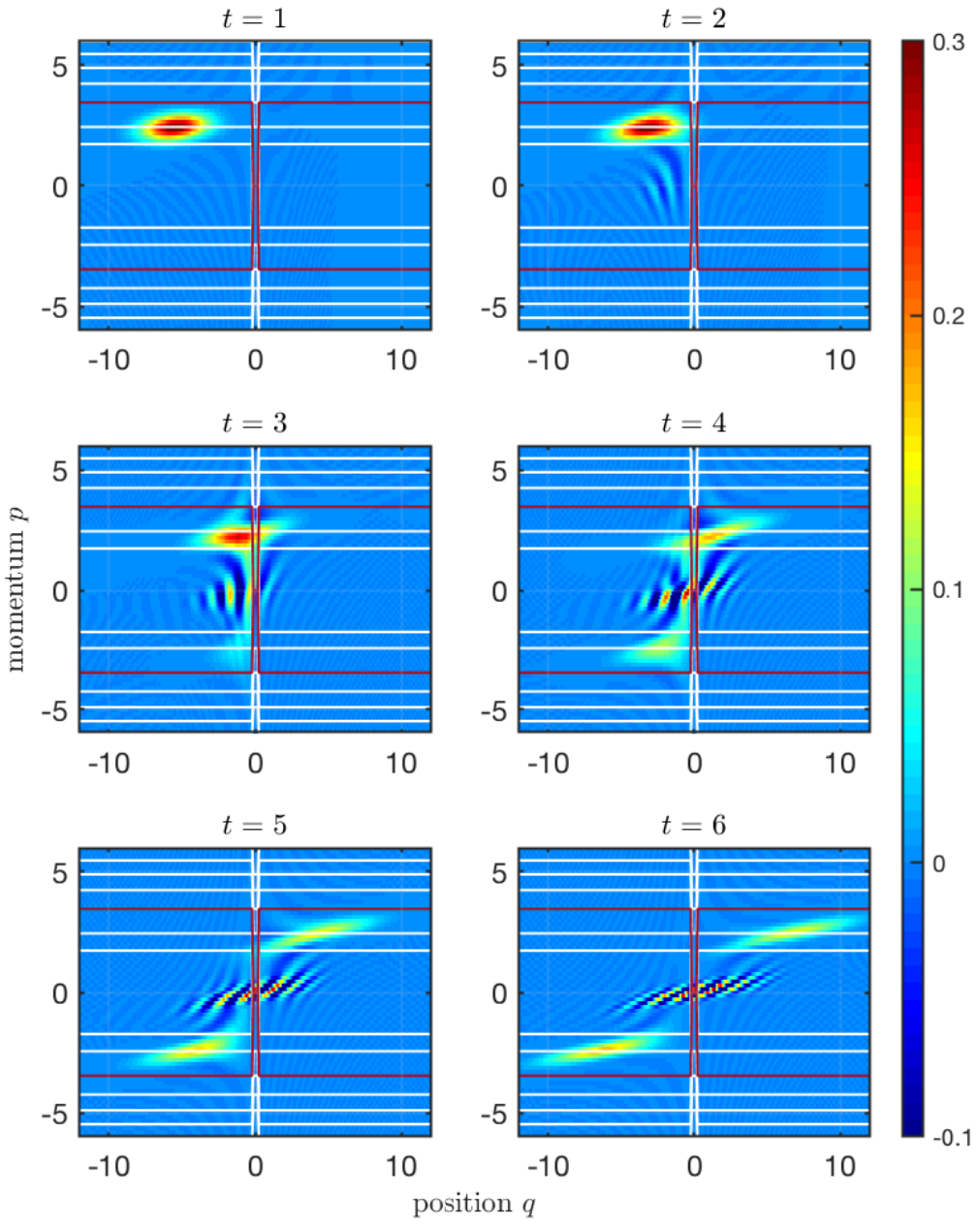

Figure III.1.: The Wigner function of the rectangular scattering model with parameters of case (b) in Figure II.6 at six time instances, depicting the phase-space evolution.
The system parameters are: $q_0 = -8$, $\Delta_q = 2$, $V_0 = 6$, $w = 0.4$, $E_i = 3$ ($p_0 = 1.73$). The additional lines represent classical trajectories, with the separatrix in red.

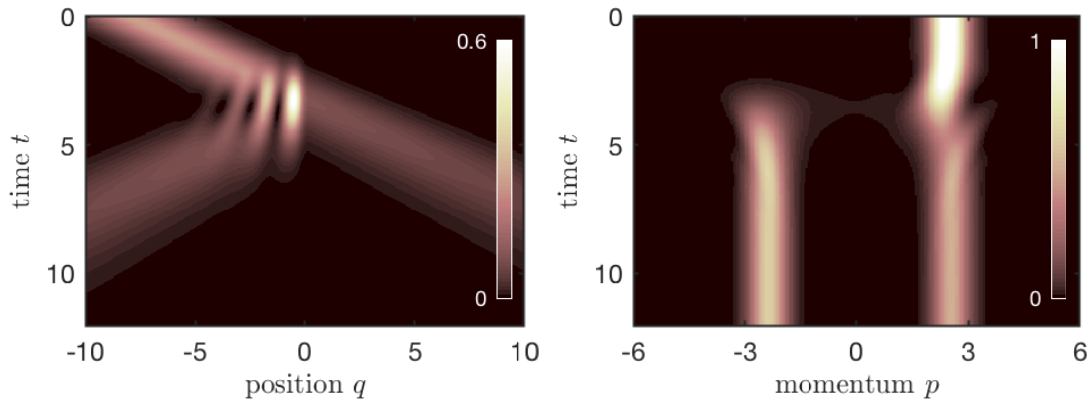

(a) distribution $\rho(q)$ (b) distribution $\sigma(p)$

Figure III.2.: Marginal distributions of Wigner functions computed with the *Wigner-Ville* transform for the tunneling model; compare to Figure III.9. *(a)* The spatial distribution reproduces Figure II.6. *(b)* The momentum distribution shows the change in p for the reflected particle and the spread during the interaction with the barrier.

The initial distribution in Figure III.1 is located almost completely beneath the separatrix and this distribution of momentum remains after the interaction. Thus there are no classically allowed trajectories for the particle to get to the other side.

As stated beforehand the marginal distributions $\rho(q)$ and $\sigma(p)$ where obtained according to Equation III.2a. The result is shown in Figure III.2.

The spatial distribution ρ is the same as in Figure II.6 given by the wave functions. This is as expected, since the Wigner function $W[\psi]$ here is directly computed from these wave functions. Computing ρ with the Wigner-Ville transform is therefore a more complicated way of performing $|\psi|^2$.

$\sigma(p)$ however delivers additional information. But it could be gained the same way as for the decay models before in Section II.b.2 instead, so this is basically a Fourier transform of the wave function with extra steps.

At first the wave packet moves towards the barrier with a momentum distribution around p_0.

Upon encountering the barrier, the distribution spreads in p to higher and lower values, whereas the main part steers to $p = 0$. At that point a second distribution emerges around $-p_0$, which is spread out at first as well, but then focuses to a straight line along time similar to the incoming wave packet before. This represents the reflected particle traveling backwards without a change in momentum.

The transmitted wave packet moves onwards from the initial incoming distribution, but it forms partly from higher momentum during barrier interaction.

How can quantum tunneling be understood in this numerical model?

It presents itself as a spreading in the momentum distribution close to the edge of

the barrier and a smearing of the Wigner function around the trajectories, enabling it to take a classically allowed path over the barrier.

2. Decay of Quasi-Stationary States

Rectangular Barrier

The time evolution for this model is shown in Figure III.3 on the basis of six time instances. The classical trajectories take the same form as in the tunneling model with the rectangular barrier[e], except they are not open to the left of the barrier, but cut off and set to zero at $q = 0$ because of the wall.

The Wigner function is initially contained with in the separatrix, except for small tails along the edges of the well extending to high (and low) momentum, similar to the free particle approaching the barrier in Figure III.1. Such an extension is also seen in the energy distribution $\omega(E)$ (compare Figure II.9) and gives an initial probability for the particle to be unbound.

The distribution flows partially through the barrier, crossing the separatrix similar to the tunneling model (Figure III.1).

The bulk of the tunneled distribution flows away. Interference patterns form, exhibiting negative values in small areas. This pattern stays mostly unaltered over time indicating the continued, almost stationary, flow away from the well. The density within the well sinks steadily and the oscillations of the bound distribution die down. The momentum of the distribution flowing away decreases over time.

For the most part this shows the expected behavior: A particle's distribution function is located either in the well, where it oscillates or it penetrates the barrier and moves away from it on the other side.

Quantum Pendulum Barrier

The Wigner function for the quantum pendulum barrier is shown in Figure III.4. The bound trajectories form closed orbits that do not extend to the separatrices because of the energy-dependent width of the potential well (compare Figure II.13).

Overall, the behavior is very similar to the rectangular model, especially for the free particle beyond the barrier.

The initial distribution is more confined in q, but also with more prominent tails and large negative values between them. These tails stretch to higher momenta, giving the indication that this extension along p is a result of the uncertainty principle.

The parts of the distribution at high momentum vanish fast and form a complex pattern of positive and negative values above the separatrix.

[e] compare to Figure III.1

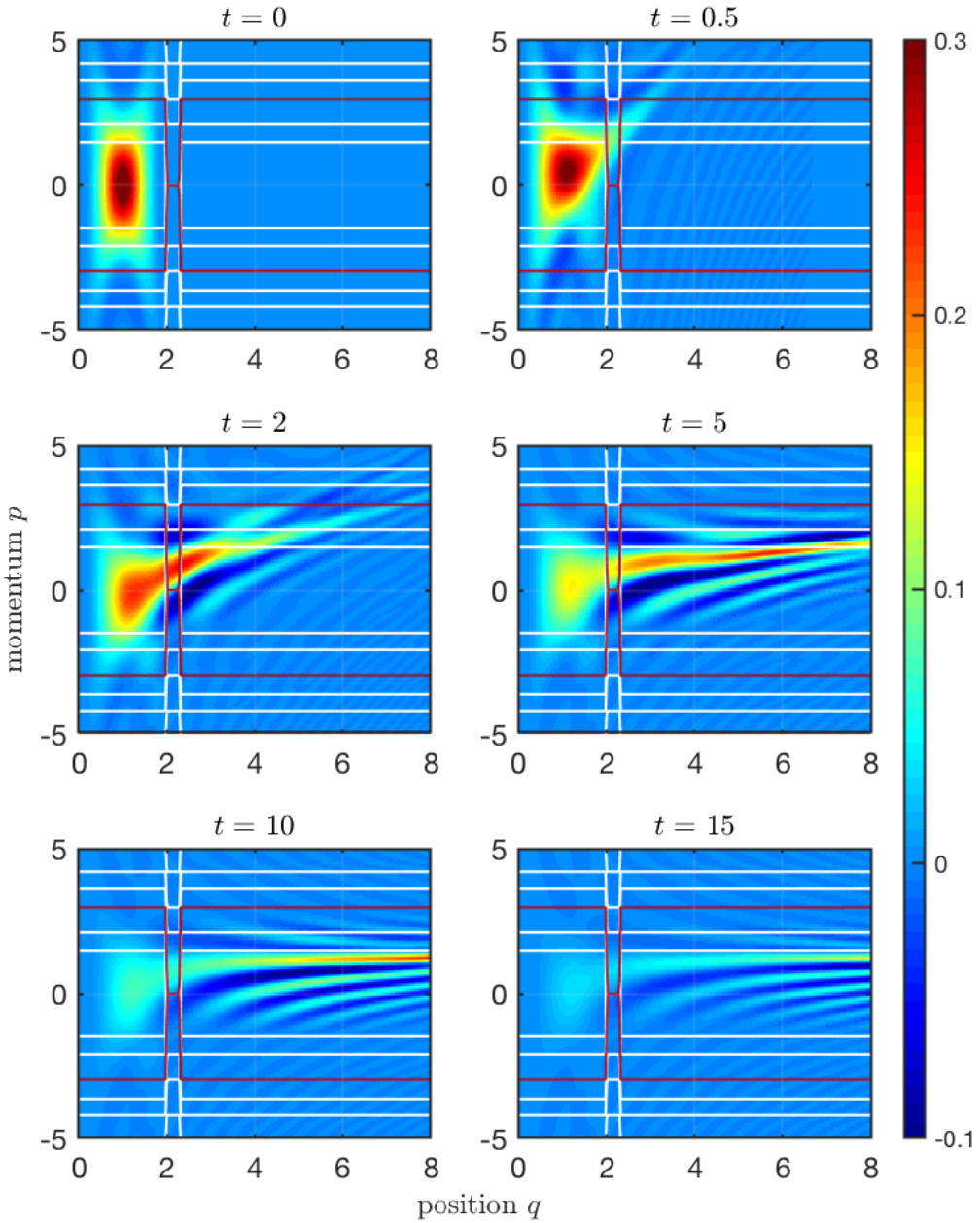

Figure III.3.: Plots of the Wigner function for Figure II.10 at six time instances depicting the evolution in phase-space for the rectangular decay problem. The system parameters are: $a = 2$, $w = 0.3$ and $V_0 = 4.4$, $\Gamma = 0.27$, $\mathcal{E} = 0.28$. The additional lines represent classical trajectories, with the separatrix in red.

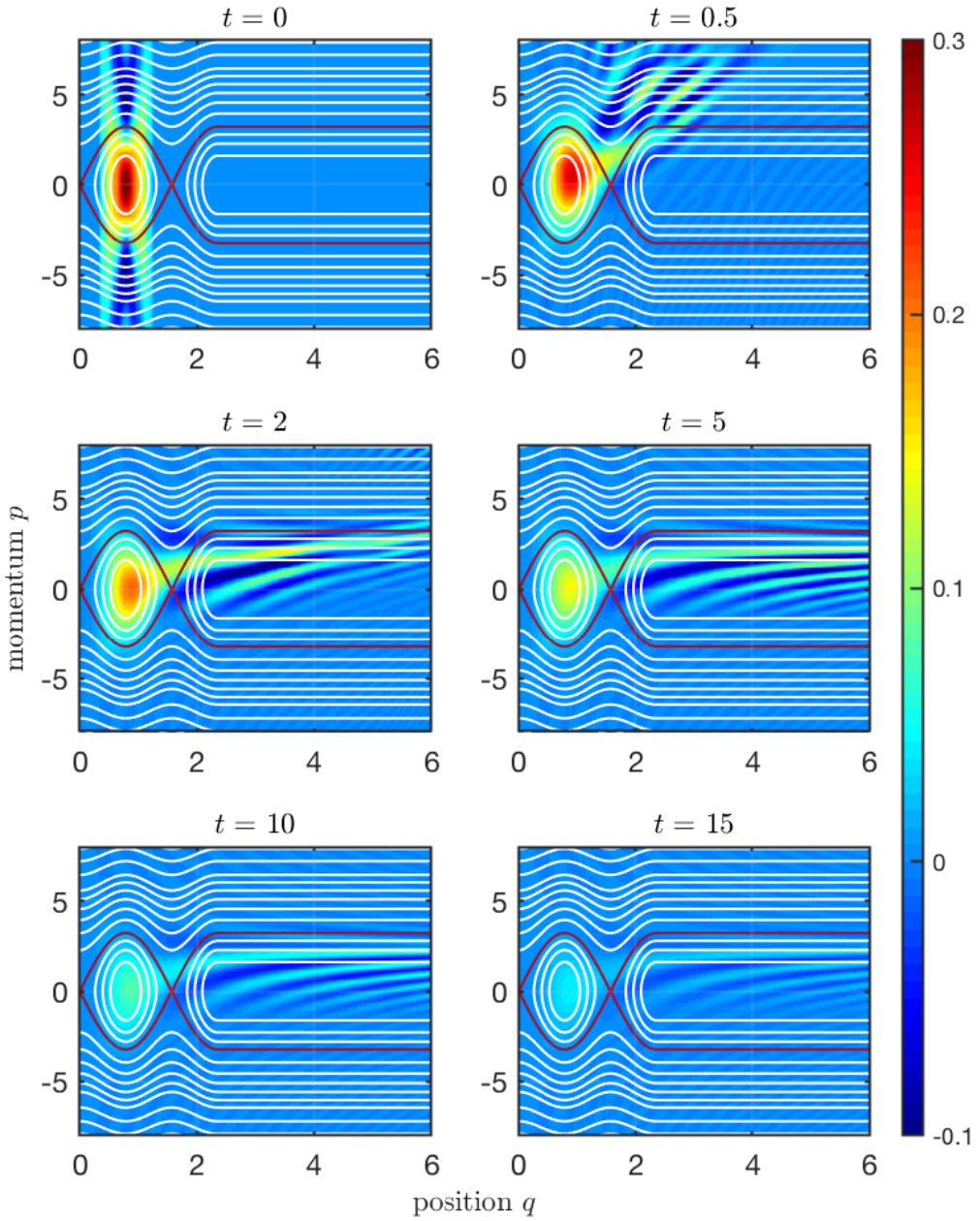

Figure III.4.: Plots of the Wigner function for Figure II.14 at six time instances depicting the evolution in phase-space for the quantum pendulum decay problem. The system parameters are: $a = \frac{\pi}{2}$, $b = \frac{3}{4}\pi$, $V_0 = 5.2$, $\Gamma = 0.28$, $\mathcal{E} = 0.69$. The additional lines represent classical trajectories, with the separatrix in red.

The relaxation phase is rather brief and oscillations of the bound distribution are only discernible for a short initial time interval.

Afterwards the stationary flow pattern is quickly established and the bound distribution diminishes in density. With this it is also more confined to the inner orbits, except for the outward flow.

The similarities between the time evolution of both systems of quasi-stationary decay show that the qualitative behavior is not dependent on the shape of the barrier, but it influences quantitative measures, especially concerning time.

Remembering the theory of Section II.a.2, the parameters defining the barrier determine the decay width Γ (see Equation II.14) and thereby the time scale of the evolution through the half-life of the system $t_{1/2} = \frac{1}{\Gamma}$.

The time scales of both systems are close because of the choice for the parameters resulting in closely matching decay widths.

3. Particle Capture

Capture Through Tunneling

This model shows the resonant case of particle capture through tunneling. The Wigner functions in Figure III.5 show the particle moving towards and encountering the barrier. In the beginning the distribution representing the free particle is localized beneath the separatrix in regards to the momentum, thus no movement over the barrier is expected, at least classically.

In the interaction with the barrier the particle can be reflected or transmitted. The transmitted part is then reflected by the wall and encounters the barrier again.

In summary this means that there are three possibilities of how the system evolves:

- reflection on the outside of the barrier,
- tunneling through the barrier twice – into and out of the well – and
- tunneling just once into the well, where the particle is trapped.

The first two possibilities result in a particle that moves away freely, while the third possibility develops a quasi-bound state which will subsequently decay.

Of course, all of these possibilities appear in Figure III.5 concurrently. The time evolution of the Wigner function basically presents itself as a combination of the tunneling model (Figure III.1), especially the reflected part, and the decay model, especially the stationary flow phase.

The Wigner function also makes it possible to look at the momentum with which a particle is more likely to tunnel through the barrier. Initially, the distribution is approximately centered around the innermost trajectory. The part of the distribution moving away has higher average momentum, as it is located between two trajectories now, while the decaying distribution moving away is now at a lower momentum beneath the trajectory.

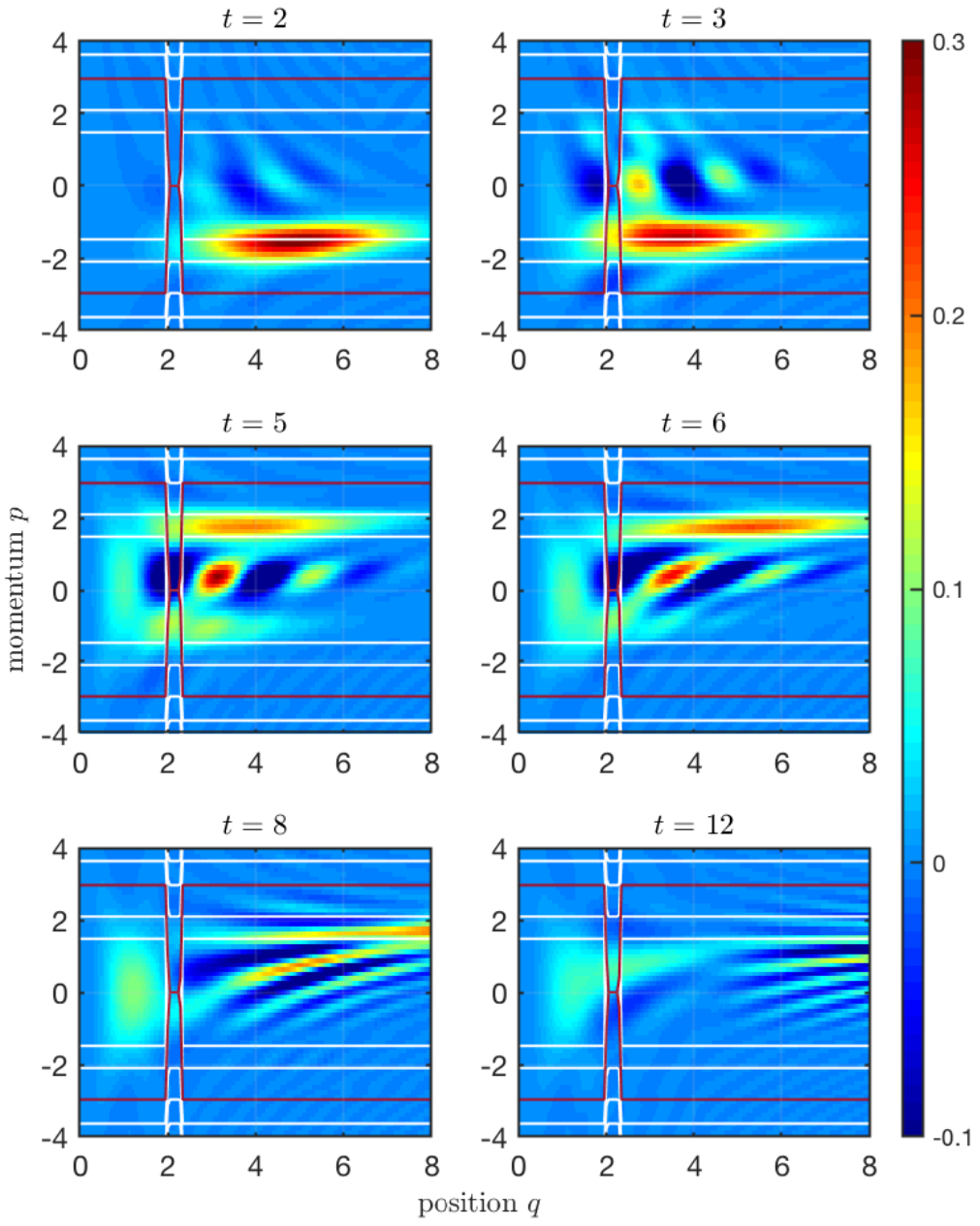

Figure III.5.: Plots of the Wigner function at six time instances depicting the phase-space evolution for the capture of a particle through tunneling in the resonant case of Figure II.16a.
The system parameters are: $V_0 = 4.4$, $w = 0.3$, $q_0 = -8$, $\Delta_q = 2$, $\mathcal{E} = 0.28$ ($p_0 = -\frac{\pi}{2}$). The additional lines represent classical trajectories, with the separatrix in red.

In Section I.b.3 of the introduction the post-adiabatic effects of a time-dependent separatrix were said to be the important part of transitioning into a different dynamical region of phase-space, *i. e.* the particle capture here.

But this model features a separatrix with a fixed area that does not change over time.

How is the particle capture possible? The difference here is that this model is a quantum system. It obeys the Moyal equation – not Liouville's theorem on which Kruskal's theorem is based – and therefore the Wigner function does not necessarily exhibit an incompressible phase-space flow.

This can lead to quantum tunneling, where the phase-space distribution flows into the separatrix area through the classically forbidden region. This indicates corrections to the classical theory of Liouvillian control via separatrices.

Capture Through Barrier Raising

The Wigner functions of the raising barrier model are shown in Figure III.6. This is the second test case showcasing the marginal distributions $\rho(q)$ and $\sigma(p)$. These are presented in Figure III.7. ρ just reproduces $|\psi|^2$ of Figure II.18 as before.

This model now features something not seen in the other models before: a time-dependent separatrix with increasing area, given by the rise of the barrier height over time. It is a simple example for the capture through separatrix growth introduced in Section I.b.3.

In the beginning the barrier is low and the separatrix still has a small area. As the barrier rises and the separatrix grows, a small part of the distribution at low momentum is deterred by it, but the bigger part moves towards the wall and a reflection pattern due to the two possibilities for the particle interfering with each other. The distribution is reflected by the wall and encounters the barrier again, but by now the separatrix has crossed over it. The particle can now tunnel through or be reflected by the barrier.

The distribution caught inside the well is oscillating, split up into one part in the center of the well and another part moving around the center further out at higher momentum.

The barrier interaction can be seen in σ at $t \approx 2$. The distribution spreads in the momentum, similar to the tunneling problem (see Figure III.2b). Undulations occur around p_0 and additionally around $p = 0$, indicating the oscillations within the well. The corresponding curve around the positive momentum is superimposed with several different streaks distinguishable by momentum. In turn, they correspond with different flows away from the barrier. This than be seen by direct comparison with $\rho(q)$ in Figure III.7b.

III.c. Introduction of the Phase-Space Evolution Scheme

The previous section (Section III.b) showed Wigner functions obtained by transforming numerical wave functions.

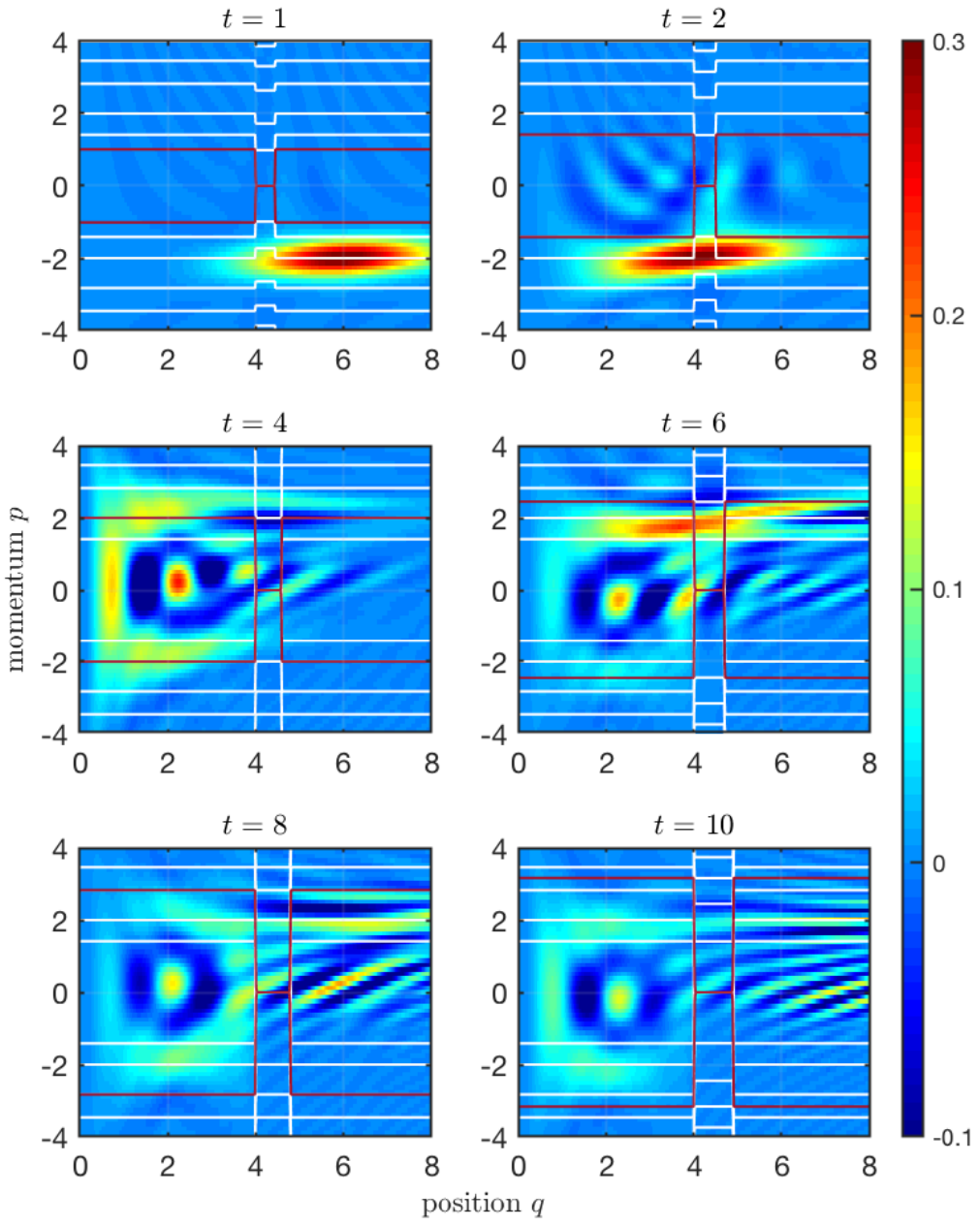

Figure III.6.: Plots of the Wigner function at six time instances depicting the phase-space evolution for the capture in a growing separatrix.
The system parameters are the same as for Figure II.18: $a = 4$, $w_i = 0.4$ to $w_f = 1$, $V_i = 0$ to $V_f = 12$, $q_0 = -8$, $\Delta_q = 2$, $E_{\text{kin}} = 0.31$ ($p_0 = -0.79$). The additional lines represent classical trajectories, with the separatrix in red.

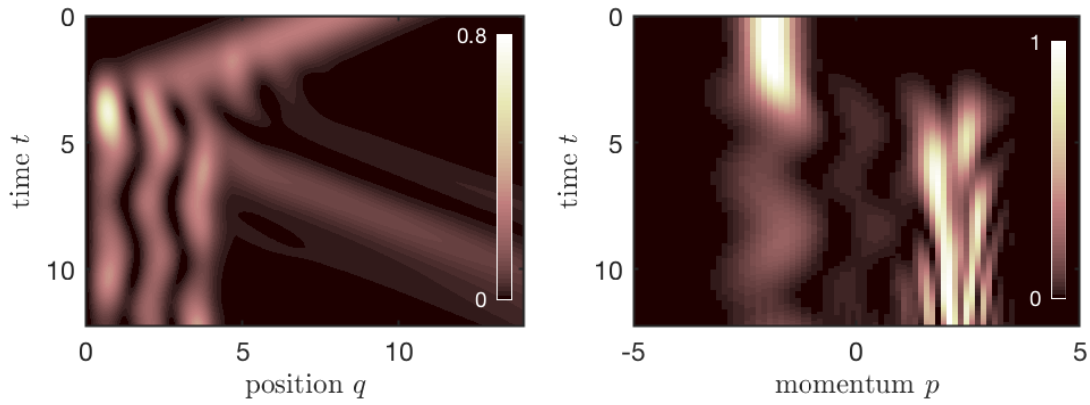

(a) distribution $\rho(q)$ (b) distribution $\sigma(p)$

Figure III.7.: Marginal distributions of the Wigner function for the raising barrier model.
(a) The spatial distribution reproduces Figure II.18. *(b)* The momentum distribution shows the change in p for the reflected particle and the oscillations of the bound particle.

Here a method is introduced to simulate the time evolution of phase-space distributions directly. This means that Wigner functions are evolved in time as native phase-space distributions via Moyal's equation. This numerical method will be termed the *Phase-Space Evolution scheme*.

More of the theoretical background[34,35] is derived in Appendix A.iii and the technicalities of the numerical scheme[36] are presented in Appendix B.ii.

1. Equation of Motion for the Wigner Function

The basis lies in the Koopman-von Neumann[37–39] formalism, an operator method for classical mechanics, aiming at a unification of quantum and classical mechanics by rewriting the latter in terms of operators on a Hilbert space.

First classical operators are introduced for position and momentum:

$$\hat{\mathbf{q}} = \hat{q} - \tfrac{\hbar}{2}\hat{\theta}, \quad \hat{\mathbf{p}} = \hat{p} + \tfrac{\hbar}{2}\hat{\lambda}. \tag{III.6}$$

These must commute because of their assumed classicality. $\hat{\theta}$ and $\hat{\lambda}$ are known as *Bopp operators*[40] which facilitate the Bopp shifts used to evaluate the $\star$-product (*e. g.* Equation A.6).

For the Moyal equation $i\hbar\,\partial_t W = H \star W - W \star H$ the Bopp shifts yield:

$$i\hbar\,\partial_t W = \left[H\left(q + i\frac{\hbar}{2}\,\partial_p,\, p - i\frac{\hbar}{2}\,\partial_q\right) - H\left(q + i\frac{\hbar}{2}\,\partial_p,\, p + i\frac{\hbar}{2}\,\partial_q\right)\right] W(q,p). \tag{III.7}$$

The differentials can be expressed through the operators $\hat{\theta}$ and $\hat{\lambda}$:

$$\hat{q} = q, \quad \hat{p} = p, \quad \hat{\lambda} = -i\partial_q, \quad \hat{\theta} = -i\partial_p \tag{III.8}$$

These are given in the q-p representation of the usual phase-space, where q and p are c-number functions. Three additional representations will be useful: q-θ, λ-θ and λ-q, which are are defined analogously to Equation III.8 and connected to each other via Fourier transforms.

Assuming Hamiltonians of the form $\hat{H} = \frac{1}{2m}\hat{p}^2 + V(\hat{q})$ Equation III.7 reads (in q-p):

$$i\hbar\,\partial_t W(q,p) = \left[-i\frac{\hbar}{m}p\partial_q + V^+ - V^-\right] W(q,p), \tag{III.9}$$

where: $V^{\pm} = V\left(q \pm \frac{i\hbar}{2}\partial_p\right)$.

Solutions are obtained by a spectral method with the time-evolution operator $\hat{U}_{dt}$:

$$\begin{gathered} W(t+dt) = \hat{U}_{dt}\, W(t) \\ \hat{U}_{dt} = \exp\left(-i\,dt\left[\frac{\hat{p}\hat{\lambda}}{m} + \frac{V^-(\hat{q},\hat{\theta}) - V^+(\hat{q},\hat{\theta})}{\hbar}\right]\right). \end{gathered} \tag{III.10}$$

For the purpose of numerical computations, Equation III.10 is evaluated using a split-operator method, giving the kinetic propagator $\hat{U}_{\text{kin}} = \exp\left(-i\frac{dt}{m}\hat{p}\hat{\lambda}\right)$ in p-λ representation and the potential propagator $\hat{U}_{\text{pot}} = \exp\left(-i\frac{dt}{\hbar}\left(V^- - V^+\right)\right)$ in q-θ, with *fast Fourier transforms* (FFT) between the different representations. As a side note, the use of the FFT leads to periodic boundary conditions.

The Hamiltonian leading to Equation III.9 is time-independent. For time dependent problems Equation III.10 can still give results, assuming the potential $V(\hat{q},t)$ only varies slowly in time is adequately approximated by instantaneous evaluations.

A comparison of the resulting Wigner functions to the Wigner-Ville transforms justifies the use of the Phase-Space Evolution scheme for time-dependent models.

2. Selected Problems in Tunneling, Capture and Decay

This sections mainly shows that the previously examined evolutions in phase-space can also be achieved by the Phase-Space Evolution scheme, but there are no further discoveries on the physical properties. Since the simulations show no behavior differing qualitatively from the Wigner functions of Section III.b, the models regarded here will be limited to the tunneling, decay and raising capture model, each with a rectangular barrier.

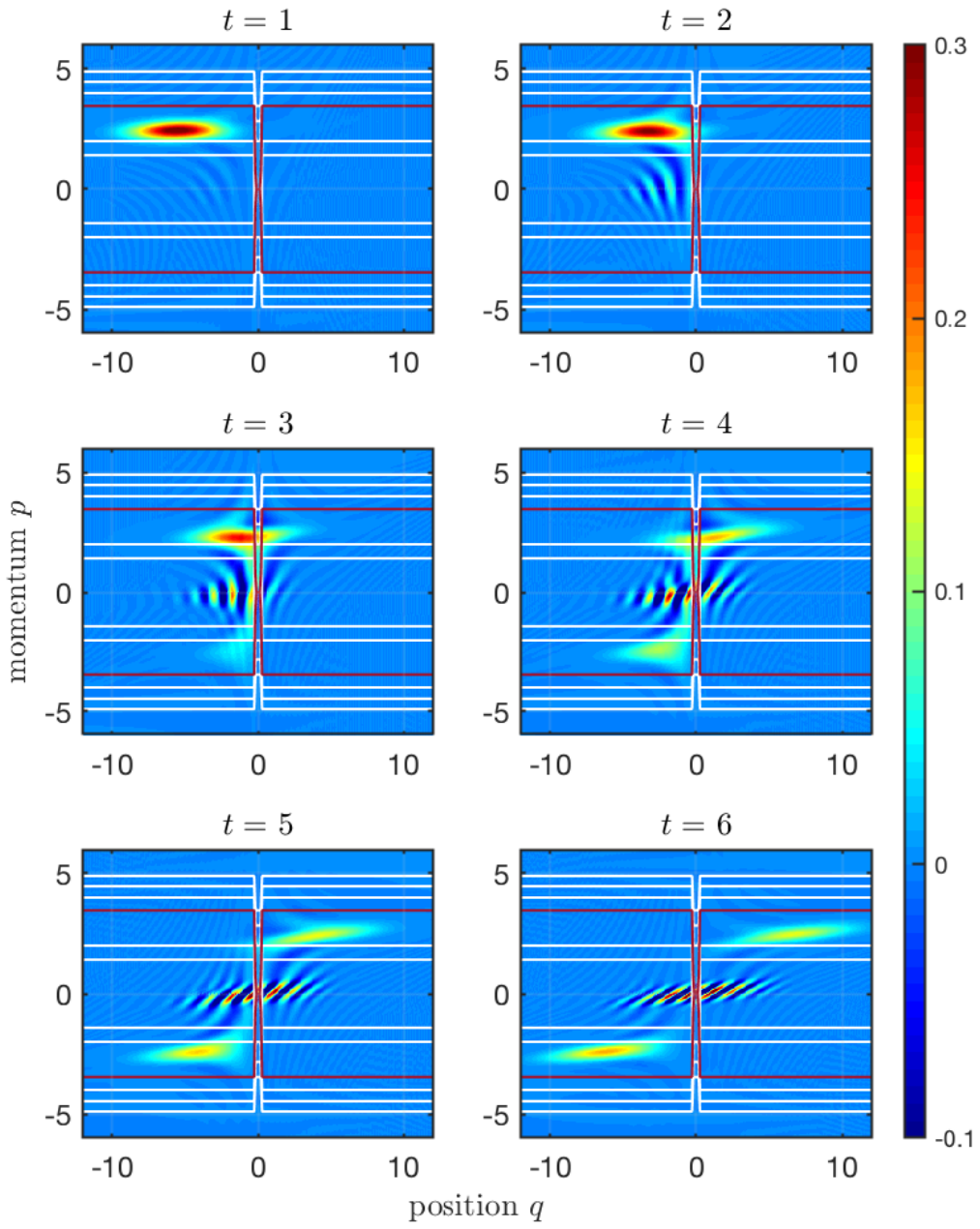

Figure III.8.: The evolution of the Wigner function at six time instances via the Phase-Space Evolution scheme for the rectangular scattering problem.
The setup is the same as in Figure III.1 with the parameters: $V_0 = 6$, $w = 0.4$, $p_0 = 2.45$, $\Delta_q = 2$, $\Delta_p = 1/2\Delta_q = 0.25$. The additional lines represent classical trajectories, with the separatrix in red.

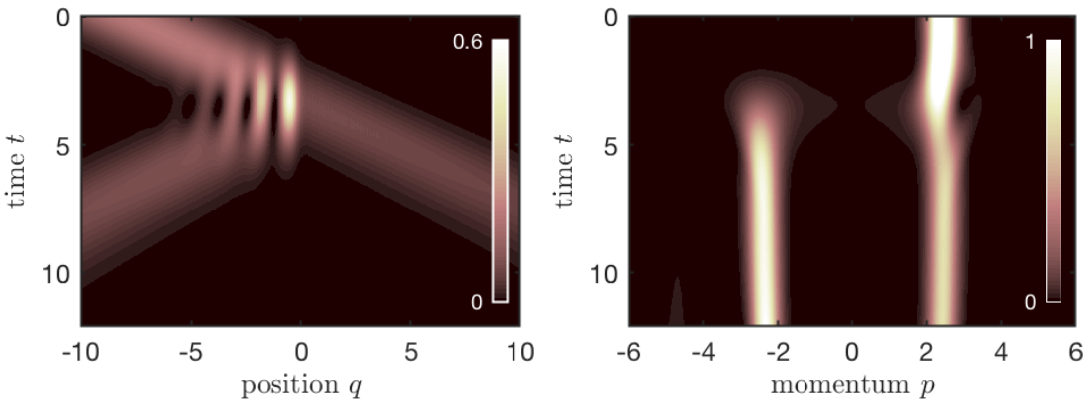

(a) distribution $\rho(q)$ (b) distribution $\sigma(p)$

Figure III.9.: Marginal distributions of Wigner functions computed with the *Phase-Space Evolution* scheme for the tunneling model; compare to Figure III.2. *(a)* The spatial distribution reproduces Figure II.6. *(b)* The momentum distribution shows the change in p for the reflected particle and the spread during the interaction with the barrier.

Barrier Penetration

The first system presented here that is simulated with the *Phase-Space Evolution scheme* is the particle tunneling through a rectangular barrier. The result is shown in Figure III.8, which can be directly compared to Figure III.1. The setup of the system is the same as showcased for the Wigner-Ville transform. Which also means that boundary conditions are not an issue for this model.

Since the problem is now two-dimensional, the initial distribution needs to be defined in q and p. The Wigner transform of a Gaussian wave packet can be regarded as a superposition of Gaussian distributions in q and in p. Thus the initial phase-space-distribution is given by:

$$W_0 = \frac{1}{2\pi\Delta_q\Delta_p} \exp\left(-\left(\frac{q-q_0}{\sqrt{2}\Delta_q}\right)^2 - \left(\frac{p-p_0}{\sqrt{2}\Delta_p}\right)^2\right). \tag{III.11}$$

q_0 and p_0 are the initial values for position and momentum. Δ describes the standard deviation in q or p. Due to the uncertainty principle the two are connected through: $\Delta_q\Delta_p \geqslant \frac{1}{2}$. For the simulation the minimum uncertainty was chosen.

The depictions in Figure III.8 shows almost the same development as the Wigner transforms in Figure III.1. One difference is the initial state, which is not quite identical. W_0 is slightly elongated along the q-direction. This leads to the distribution encountering the barrier sooner. But this difference runs through all the panels equally.

Another problem with the scheme is the density of the distribution. Initially it is normalized by $\iint \mathrm{d}q\,\mathrm{d}p\,W_0(q,p) = 1$. While the time evolution should be unitary

and thus norm conserving, this requires small step sizes in the grid. Computational restraints limiting the size of the grid and additional numerical errors introduced in the calculations lead to a decrease in the norm over the course of the simulation.

The distribution has therefore been renormalized after every time-step. However, this implies a decrease of the norm uniformly spread over the entire grid, but a localized decrease due interferences is a reasonable assumption.

Quasi-Stationary Decay

The time evolution is shown in Figure III.10, with the same parameters for the barrier and the initial state as in Figure III.3.

In the Crank-Nicolson method of Section II.b.2 the underlying grid ended at $q = 0$, with the corresponding boundary condition set to $\psi|_{q=0} = 0$, thus also defining the corresponding boundary values of the Wigner-Ville transforms. For the Phase-Space Evolution scheme the wall was approximated by a flank of the flat-topped gaussian[f] (see Equation II.22), which was also used for the rectangular barrier.

The initial state is given through $W[\psi_0]$, the Wigner transform of the initial wave function in Equation II.20. But there is still a difference between these distributions when directly compared, because the systems is discretized differently. W_0 in the t=0-panel of Figure III.10 is altogether less confined and more spread out to higher momenta.

Otherwise the behavior is very similar, especially after the initial relaxation, when a more stationary decay picture has established itself in the system. The relaxation shows more flow over the barrier due to the larger spread in momentum.

The spreading along the wall does occur as well, but the distributions seems to be less separated from it. The reason for this is found in the setup of the numerical system: the flank of the flat-topped gaussian makes less of a hard boundary and gives the possibility to move closer to $q = 0$. As such the cut-off in the Wigner-Ville model is steeper and the resulting Wigner function is more separated from the wall.

The Wigner functions also present the possibility to compute probabilities (see Equation III.2c). Figure II.11 already showed the curve of the non-decay probability that was obtained with the Phase-Space Evolution scheme. It was computed by numerically integration of the Wigner function at different time-steps over the well area, here defined as $q \in [-1, a]$ without limits in p. The extension to -1 is necessary because the flank of the wall does not strictly end at $q = 0$ for every energy. But beyond the wall the contributions to P_{nd} should still vanish.

Raising-Barrier Particle Capture

Lastly, the problem of the raising and widening barrier is discussed for the Phase-Space Evolution scheme. The resulting Wigner functions are shown in Figure III.12. This model features an example for a time-dependent potential.

[f] centered around -40 with height $V_0 = 10^{10}$ and half-width $w = 78.15$

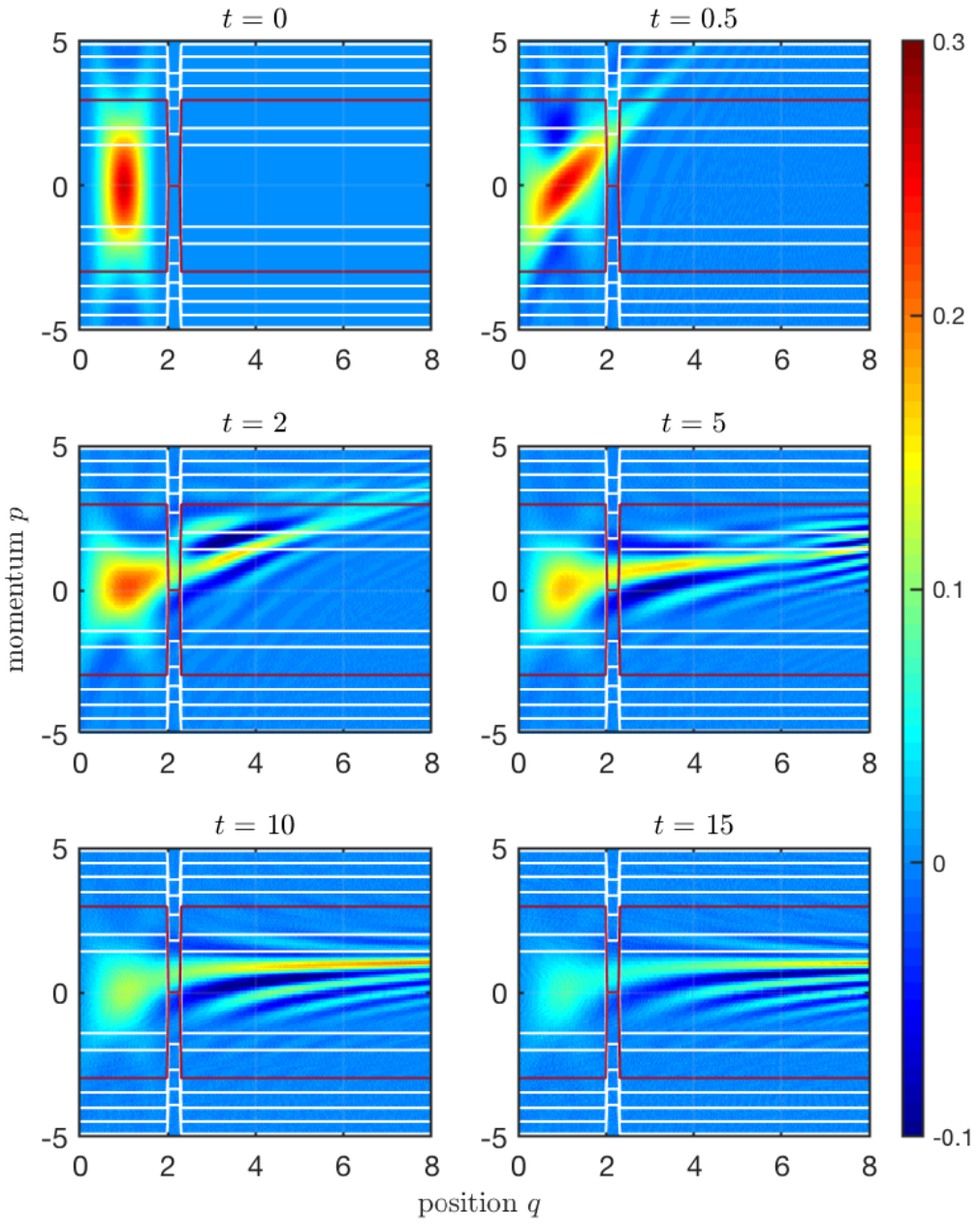

Figure III.10.: The evolution of the Wigner function at six time instances via the Phase-Space Evolution scheme for the quasi-stationary decay with a rectangular barrier.
The setup is the same as in Figure III.3. with the parameters: $a = 2$, $w = 0.3$ and $V_0 = 4.4$, $\Gamma = 0.27$, $\mathcal{E} = 0.28$. The additional lines represent classical trajectories, with the separatrix in red.

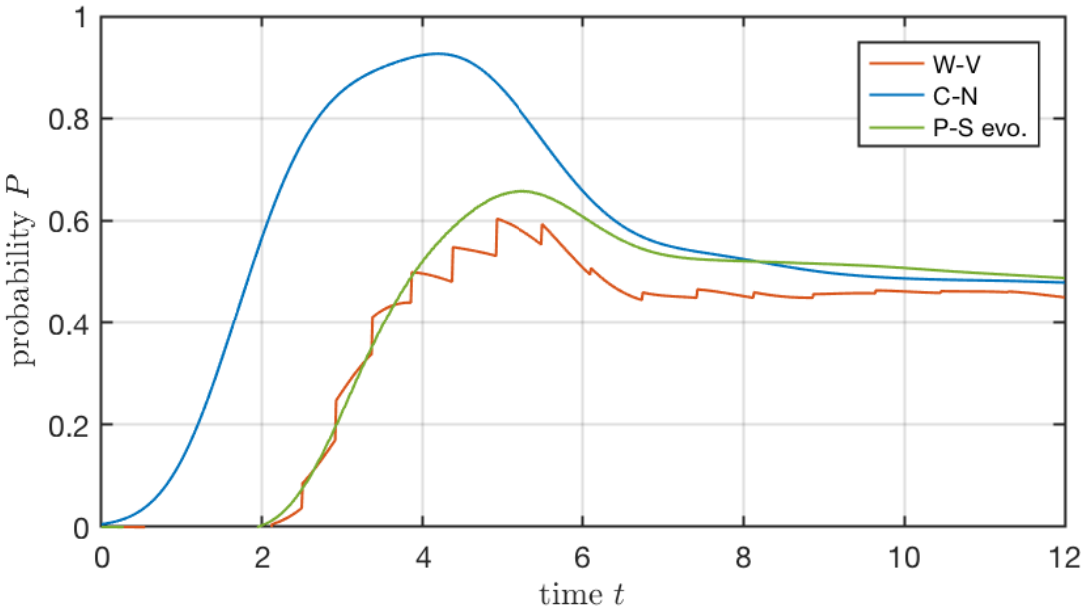

Figure III.11.: Comparison of the probabilities for a bound particle in the raising-barrier model obtained through the three different methods.
C-N: integration of $|\psi|^2$ over the well area without restrictions on the momentum; *W-V*: integration of the Wigner-Ville transform over the separatrix area; *P-S evo.*: same as W-V, but uses the Phase-Space Evolution scheme.

This simulation uses the same system parameters as the previous one shown in Figure III.6 Still, for some unknown reason the initial state does not match the one in the Wigner-Ville transform.

As with the other models the qualitative results are very similar. The Wigner functions show no problems or differences that could be attributed to a failure in the numerical scheme because of the time-dependent potential.

Within the well the negative areas between the rings of bound states are more prominent.

The distribution for $t = 10$ shows similarity to the initial bound state of the rectangular decay problem, underlining the possibility to gain bound states in this time variable potential.

At this point three different ways of computing probabilities are available: integrating the spatial probability distribution $\rho(q)$ gained from the Crank-Nicolson method or integrating the Wigner function gained from Wigner-Ville transforms or the Phase-Space Evolution scheme. Figure III.11 shows a comparison of these three methods for the raising barrier model.

Using only the wave functions in q for probabilities has the additional probability of an unbound particle moving across the well area and leaving it again, because there is

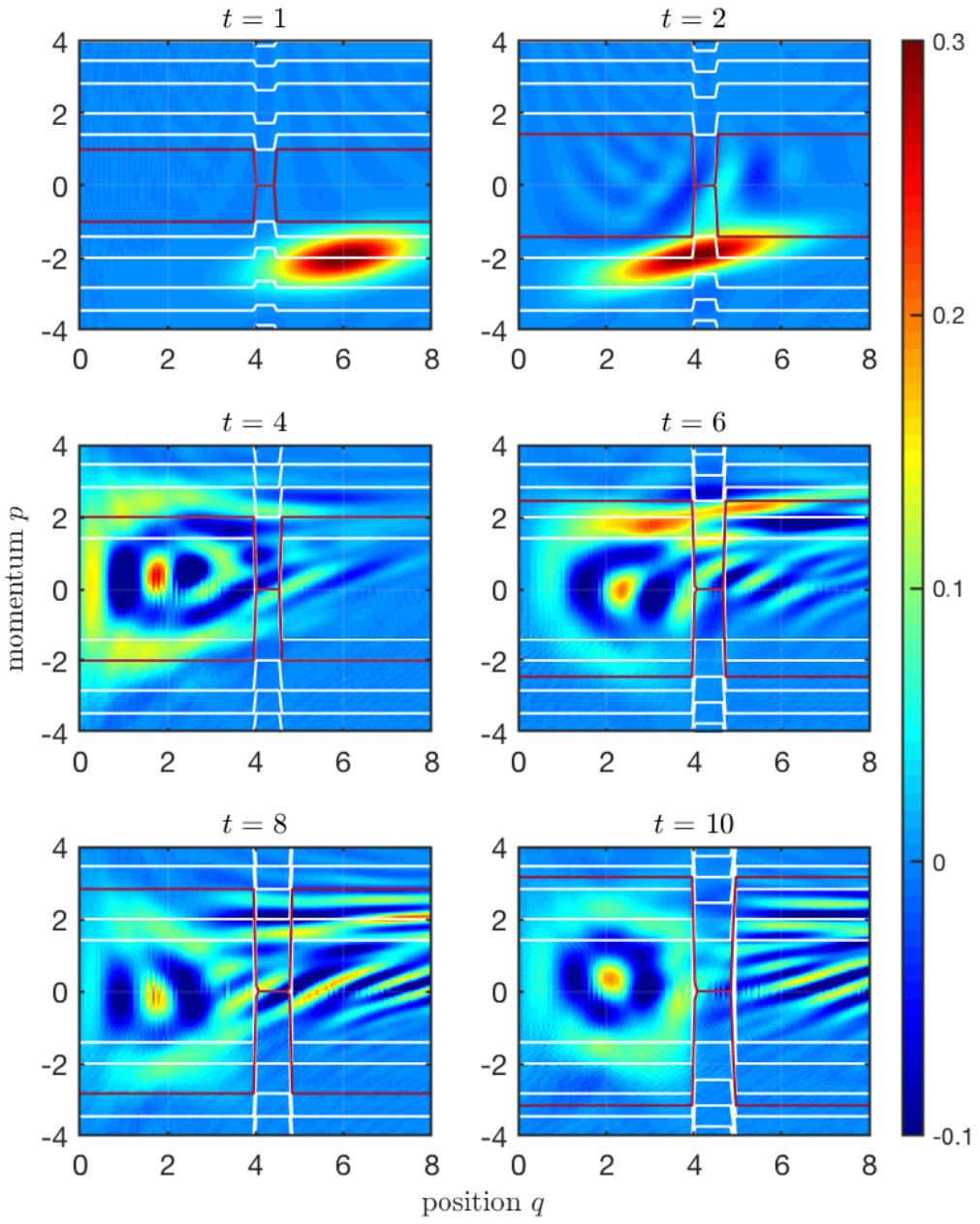

Figure III.12.: The evolution of the Wigner function at six time instances via the Phase-Space Evolution scheme for the capture with a raising barrier.
The setup is the same as in Figure III.6. with the parameters: $a = 4$, $w_i = 0.4$ to $w_f = 1$, $V_i = 0$ to $V_f = 12$, $q_0 = -8$, $\Delta_q = 2$, $E_{\text{kin}} = 0.31$ ($p_0 = -0.79$), $\Delta_p = 1/2\Delta_q = 0.25$. The additional lines represent classical trajectories, with the separatrix in red.

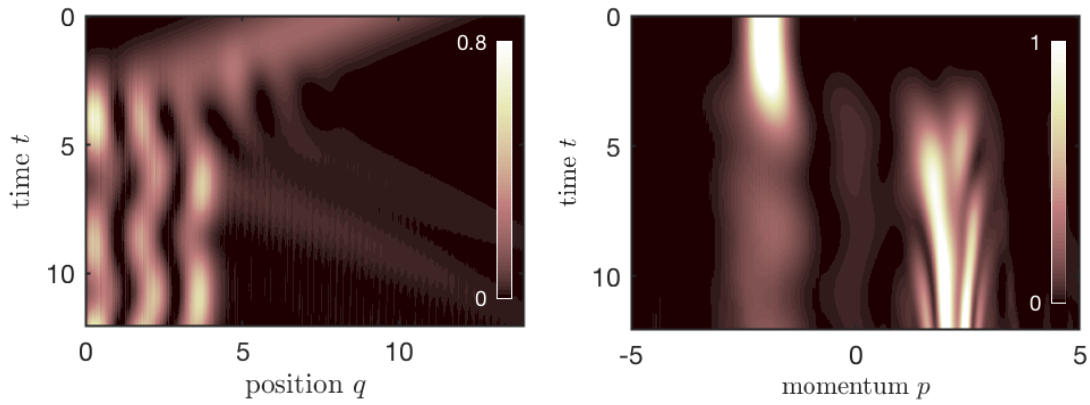

(a) distribution $\rho(q)$ (b) distribution $\sigma(p)$

Figure III.13.: Marginal distributions of the Wigner function for the raising barrier model.
(a) The spatial distribution reproduces the qualitative behavior seen in Figure II.18. *(b)* The momentum distribution shows the change in p for the reflected particle and the oscillations of the bound particle.

no additional condition for a trapped particle in $\psi(q)$. Therefore the Crank-Nicolson (C-N) curve starts to rise earlier and shows higher probability values until the unbound portion of the distribution has left the well area.

The Wigner functions $W(q, p)$ are two-dimensional and the separatrix gives additional limits in p for the integration. Thus only the part of the distribution within the separatrix contributes to the probability.

The integration can result in negative values if the Wigner function within the separatrix takes on mostly negative values. But this is only for a short time before the probability curve starts to rise. The orange curve is rather jagged. The reason for this is not clear. But it still has a similar shape compared to the green curve of the Phase-Space Evolution scheme. The difference in quantitative behavior of these two curves could be traced back to the different numerical methods and was also visible in the probabilities of the rectangular decay model (see Figure II.11).

III.d. Assessment of Phase-Space Methods in Quantum Mechanics

This chapter employed two different methods to obtain the time evolution of Wigner quasi-probability distributions numerically. Both of them deliver basically the same distribution in phase-space, at least qualitatively, which is a great feat since they are build upon very different schemes.

The *Wigner-Ville transform* translates wave functions into phase-space and is therefore dependent on a numerical method that solves the Schrödinger equation (*e. g.* the

Crank-Nicolson method) first. But if the wave functions are already given, this method can be used at any time step. It is not necessary to evolve an initial distribution.

The p-vector is defined by the sampling rate of the fast Fourier transform. A fine grid in q thus leads to a coarse grid in p and vice versa. Since the Wigner-Ville transform is used in signal processing there are implementations readily available[g].

The *Phase-Space Evolution scheme* utilizes a split-step method to find solutions to a wave equation-like equation of motion for the Wigner function derived from Moyal's equation. It therefore operates completely on the basis of a phase-space description. The p-vector is here defined directly, giving more control over the resolution in the momentum.

[g] *e. g.* the MATLAB function `wvd` in the Signal Processing Toolbox, introduced in version R2018b

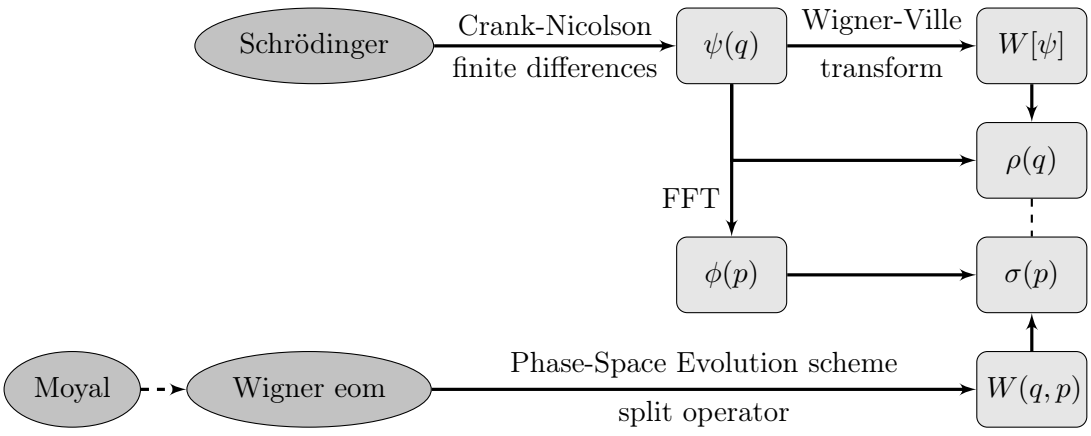

Figure III.14.: Illustration of the paths from equations to numerical results that are used in this thesis.

IV. The Tilted Lattice: A Simplified Approach to the Tilted Washboard Potential

The models so far introduced tunneling and particle capture in with wave functions as well as with Wigner functions in the phase-space-picture. Now, these are going to be used as a basis for the simulation of a *daemon system*.

Section IV.a introduces the model and explains the scaling.

Section IV.b presents the results of simulations of the wave function $\psi(q,t)$ via the Crank-Nicolson method and of the Wigner function $W(q,p;t)$ via the Phase-Space Evolution scheme. A discussion of the characteristics follows.

Section IV.c is concerned with quantum mapping. A quantum canonical transformation is given in analogy to classical Hamiltonian daemons. Further approaches for going beyond a simplified model are explored as well.

IV.a. Introduction to the Time-Dependent Tilted Lattice

The model presented here is termed the *tilted lattice*. While it has the sinusoidal structure of a tilted washboard[a], it is also simplified compared to the effective rescaled Hamiltonian in Equation I.4.

The tilted lattice exhibits possible bound states in a local potential well, *i. e.* a down-conversion phase, and time-dependent separatrix change, *i. e.* capture of phase-space points in the separatrix. It is therefore an example of a daemon system.

The Hamiltonian is given by[b]:

$$\begin{aligned} \hat{H}(q,t) &= \frac{1}{2}\hat{p}^2 + V(\hat{q},t) \\ V(\hat{q},t) &= \dot{\alpha}\hat{q} - \gamma\beta(t)\cos(s\hat{q}) \end{aligned} \tag{IV.1}$$

where s can scale the potential wells, γ gives the amplitude of the cosine, $\dot{\alpha}$ gives the tilt, so that γ and $\dot{\alpha}$ together determine the maximum depth of the potential wells.

[a] as introduced in Section I.b.2, also compare Figure I.5

[b] the quantum version of H_2 in [10]

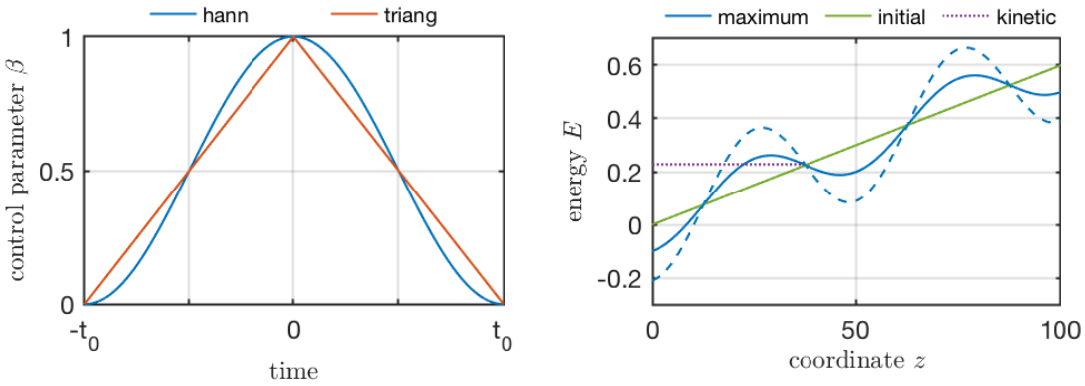

(a) control parameter β (b) potential energies

Figure IV.1.: (a) Development of the control parameter β over time. *Hann* was used in the simulations, with *triang*[c] given here for comparison.
(b) Potential of the tilted lattice model for the simulation depicted in Figure IV.2c and IV.2d.
Initial linear potential at $t = \pm 300$ in green and maximum depth of the wells at $t = 0$ in blue, with the solid curve for the scaling of shallow wells and the dashed curve for the semi-classical scaling. The dashed violet line indicates the kinetic energy $\frac{1}{2}p_0^2$ of the particle.
The potential is comparable to Figure I.5.

$\beta(t) \in [0, 1]$ is a time-dependent control parameter, modifying the potential depth, which enables the opening and closing of the local potential wells. Examples for the shape of β are given in Figure IV.1a. Different forms of β do not change the behavior qualitatively.

The tilted washboard Hamiltonian I.3 shows a $\sqrt{L^2 - L_z^2}$-prefactor of the cosine, which can be rescaled to $\sqrt{1 - F^2}$. The parameter β is used here as a simplification thereof. A momentum-dependent potential is difficult for numerical computations and adds complications in the quantization procedure of a classical Hamiltonian (see Section IV.c.3).

The control parameter governs the dynamical behavior by opening up the potential wells, or separatrices, and thus enabling a downconversion phase. With the change in the separatrix area it also enables the capture of the weight in a bound orbit.

This model is given in the comoving frame, meaning the critical velocity is shifted to $v_c = 0$. A captured particle is kept around a fixed height, so the downconversion phase acts against the falling of the particle.

[c]Both are window functions available in MATLAB's the signal processing toolbox.

Scaling of the System

The potential in Equation IV.1 is quasi-periodic with a quasi-period $\Pi = \frac{2\pi}{s}$. This sets the maximum width of the wells and barriers. The system parameters $\dot{\alpha}$ (measure of the adiabaticity) and γ (coupling strength) set the maximum depth of the wells. From this the semi-classical number of bound states N_{sc} can be computed by means of the Bohr-Sommerfeld quantization scheme.

A few assumptions ought to be made about the system:

- It should be rather small, measured in terms of Π, so that it can be considered as a quantum system.
- It should also be within the semi-classical regime with $N_{\mathrm{sc}} > 1$.
- There should be tunneling in the model in order to study it. Since larger systems also feature wide barriers which could hinder tunneling, the wells should be relatively shallow.
- Neighboring wells should show no overlap. Tunneling out of a well should lead to an unbound state in the examinations here.
- For convenience, the particle should only be bound in the least number of wells possible (*i. e.* one or two). For this, the uncertainties σ_q and σ_p as well as the initial momentum p_0 need to be regarded in relation to Π and the time scale of the evolution, otherwise the wave packet might not be localized but spread over the entire system.

Choosing parameters for the system without also scaling up the potential (*i. e.* $\Pi = 2\pi$) would mean only a slight incline with very shallow wells, basically giving a linear potential with small undulations, unless restricted to a very small region of q with only a few periods of the potential. Such a small region would be problematic, because the particle would be effectively delocalized quickly due to the spreading of the wave packet.

Furthermore this corresponds to the deep quantum regime. Increasing the depth of the wells on the other side leads to considerable overlap of the wells.

This gives a lower bound for a semi-classical system of $\Pi = 20$, where $N_{\mathrm{sc}} \approx 1.4$

Table IV.1.: Parameters of four systems at two different length scales.

(a)	*quantum scaling*:	$\Pi = 20, \quad \dot{\alpha} = 0.01, \quad \gamma = 0.08$ $\Rightarrow N_{\mathrm{sc}} = 0.5, \quad \Delta V = 0.07, \quad \delta V = -0.13$
(b)	*small scaling*:	$\Pi = 20, \quad \dot{\alpha} = 0.01, \quad \gamma = 0.14$ $\Rightarrow N_{\mathrm{sc}} = 1.4, \quad \Delta V = 0.19, \quad \delta V = -0.01$
(c)	*shallow scaling*:	$\Pi = 50, \quad \dot{\alpha} = 0.006, \quad \gamma = 0.1$ $\Rightarrow N_{\mathrm{sc}} = 1.8, \quad \Delta V = 0.07, \quad \delta V = -0.23$
(d)	*semi-classical scaling*:	$\Pi = 50, \quad \dot{\alpha} = 0.006, \quad \gamma = 0.21$ $\Rightarrow N_{\mathrm{sc}} = 5.6, \quad \Delta V = 0.28, \quad \delta V = -0.02$

for the maximum depth of non-overlapping wells. At this scale lies the border to the quantum regime.

Additionally a further scale-up can be considered. With $\Pi = 50$ the range of N_{sc} is given approximately from 1.8 to 5.6. These considerations lead to four scales of the model regarded here: *quantum* (shallow wells) and *small* (deep wells) scale with $\Pi = 20$ and *shallow* (shallow wells) and *semi-classical* (deep wells) scale with $\Pi = 50$. The parameters for these systems are given in Table IV.1.

ΔV refers to the maximum depth of a potential well, given by the difference of the potential energy at the unstable fixpoint and at the stable fixpoint for $t = 0$: $\Delta V = V(q_{i,\max}, t = 0) - V(q_{i,\min}, t = 0)$.

δV indicates the overlap of two neighboring wells through the difference of the potential energy at the unstable fixpoint and at the stable fixpoint of the next higher order: $\Delta V = V(q_{i,\max}, t = 0) - V(q_{i-1,\min}, t = 0)$. A negative value indicates the absence of overlap.

IV.b. The Time Evolution of the Tilted Lattice

All of the numerical tools of the previous chapters have been used to examine the tilted lattice Hamiltonian (IV.1). First the different plots of ρ, σ, P and W are described, then the time evolution is discussed in detail. The focus is on the larger systems with $\Pi = 50$.

1. Numerical Results of the Tilted Lattice

Spatial Probability Densities $\rho(q)$

The particle is initially launched upwards with momentum p_0. It keeps close to the classical parabola, albeit spread out in q. As β increases the wells open up, and it becomes possible for the particle to be trapped. But there is also a chance for a continued fall.

In the beginning of the downconversion phase a focusing of the probability density occurs as the particle is guided into the well. There is a chance to leave the well quickly after. In Figure IV.2a a division in the initial parabolic distribution can be seen, where the upper part with higher momentum is delayed from falling by the local deepening of the potential, whereas the lower part accelerated by the local raising of the barrier. Otherwise the particle is captured in the well. It is eventually released as the wells shrink and close up, ending the downconversion phase.

At the smaller scaling of $\Pi = 20$ the spreading of the wave packet appears more pronounced in relation to the wells, even on the shorter time scale. This leads to the probability density being dispersed over two or three wells. The initial values p_0 and σ_q where chosen to feature one main well with a lesser likelihood for the lower neighbor thereof.

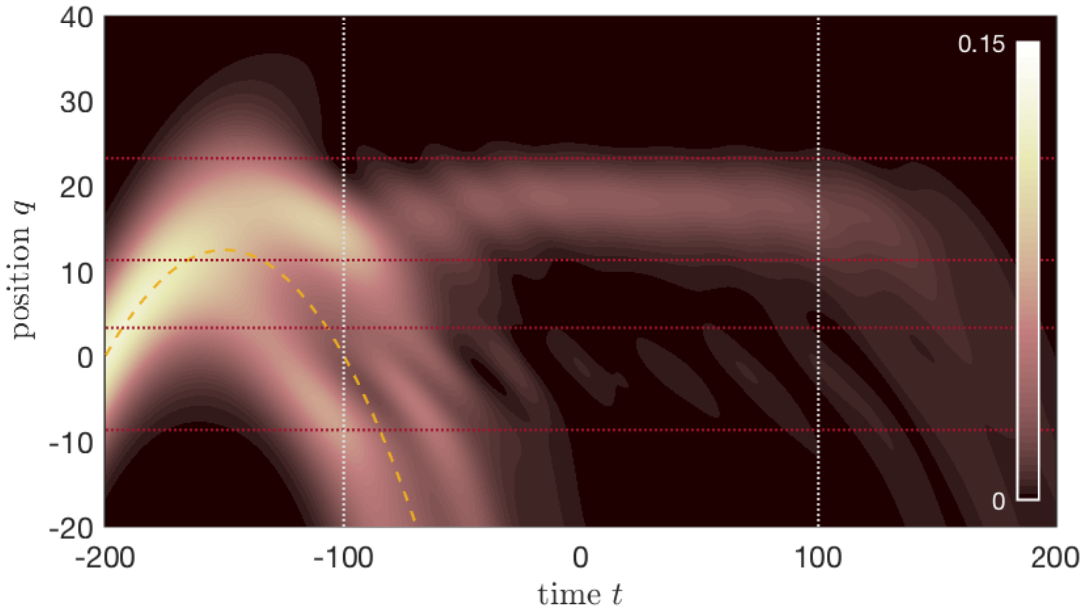

(a) quantum scaling

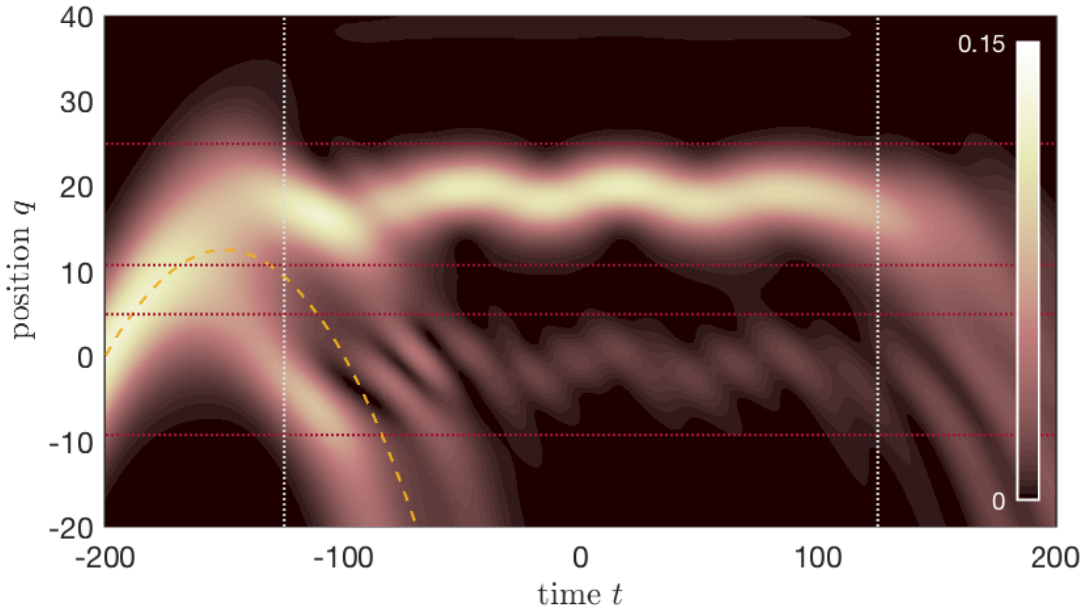

(b) small scaling

Figure IV.2.: Time probability densities $\rho(q) = |\psi(q)|^2$ for the tilted lattice model. The dotted yellow line shows the classical trajectory of the weight in a linear potential. This represents the initially decoupled particle
The parameters are given in Table IV.1, (a) and (b) show $\Pi = 20$ for times $t \in [-200, 200]$, (c) and (d) show $\Pi = 50$ for times $t \in [-300, 300]$ (next page).

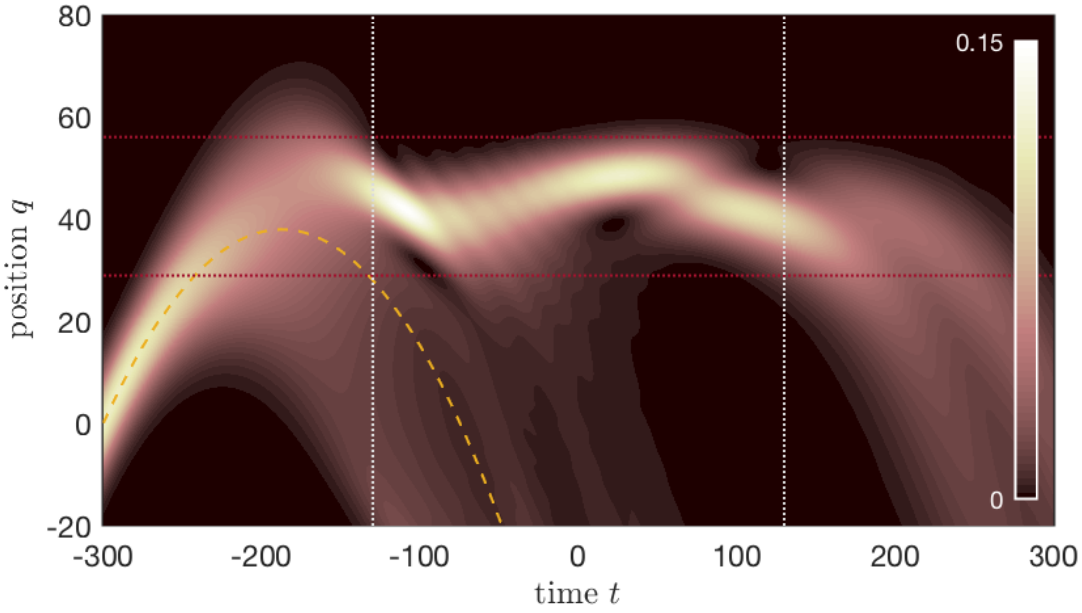

(c) shallow scaling

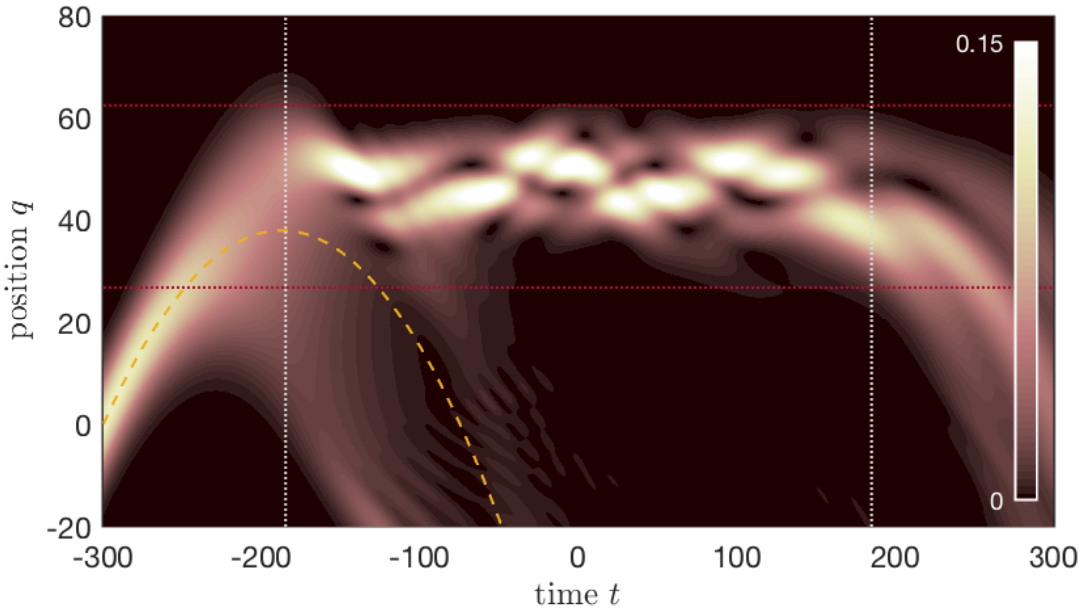

(d) semi-classical scaling

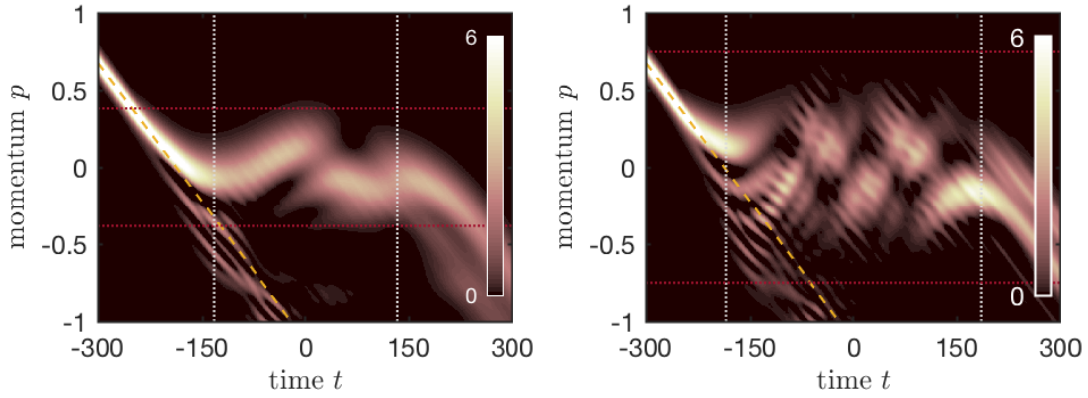

(a) $\sigma(p)$ in shallow scaling

(b) $\sigma(p)$ in semi-classical scaling

Figure IV.3.: Momentum distributions of the Wigner function for the tilted lattice model in *(a)* shallow and *(b)* semi-classical scaling.
The momentum distribution shows the decoupling phase as a straight line. The dashed yellow line illustrates this for the initial trajectory of the free particle. The dotted grey lines mark the start and end of the downconversion phase (compare Figure IV.4). The dotted red lines show the limits of p for bound states in the potential, given by $|p| \leqslant \sqrt{(2\Delta V)}$ (see Table IV.1). The downconversion phase presents as oscillations around $p = 0$.

With the larger scaling of $\Pi = 50$ the particle can be lead into one well[d]. The probability density seems to split up into multiple "stripes", indicating a superposition of different oscillation modes. This is much more prominent in the semi-classical scaling (Figure IV.2d).

Tunneling can be seen in these systems. Both the quantum and the shallow scaling show a continued flow of the probability density away from the bound distribution.

Momentum Probability Distributions σ

The momentum probability distributions for the shallow and semi-classical scaling are shown in Figure IV.3. These were obtained with the Phase-Space Evolution scheme[e].

Initially the momentum decreases linearly from p_0 because of the linear potential. This is indicated by the dotted yellow line, which corresponds directly to the classical trajectory marked in Figure IV.2. With the onset of the downconversion phase the distribution is divided. The part of the distribution pertaining to lower momentum keeps moving downwards. However, most of the distribution deviates from the free fall towards

[d] The probability to capture the particle in a neighboring well does not vanish entirely, but is considered to be insignificant and not visible in Figure IV.2c or IV.2d due to the color scaling of the pseudo-color plot.

[e] It should be noted that inaccuracies in the numerical evaluation lead to negative values in the distributions, occurring in the continued fall for $p < 0$ and $t > -150$.

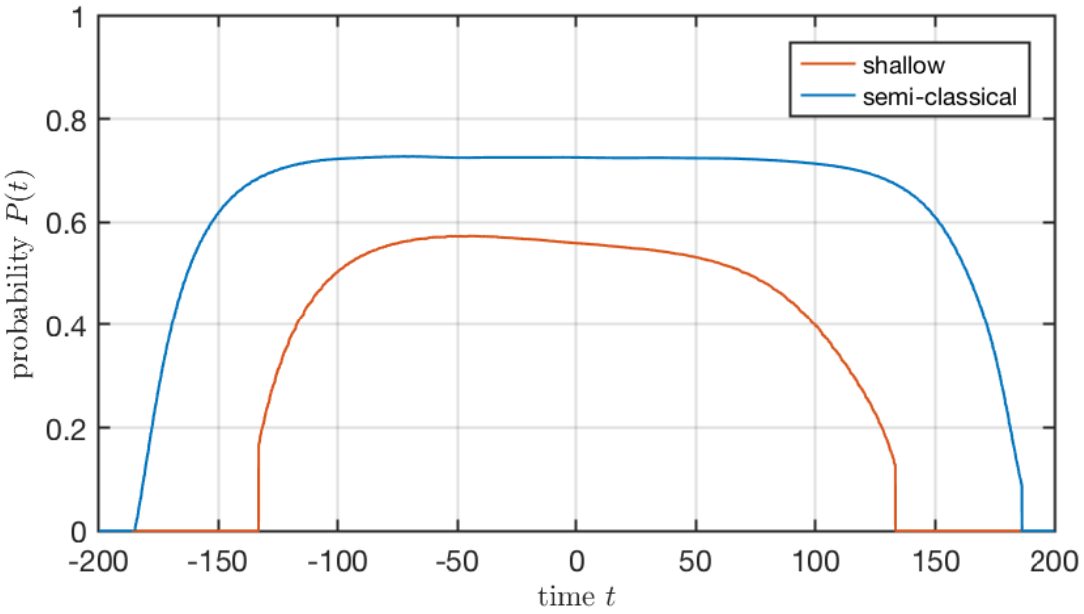

Figure IV.4.: Probability to find the particle inside the well, *i. e.* undergoing downconversion, for the shallow and semi-classical scaling in Figure IV.2c and IV.2d using the Wigner-Ville transform. Start and end of the downconversion phase are clearly visible.

$p \sim 0$ and shows oscillations, indicating the bound particle in the downconversion phase.

From the energy difference ΔV, between the top of the barrier and the bottom of the well, the limits of the momentum for a bound particle can be calculated, indicated by dotted red lines in Figure IV.3.

In the semi-classical scaling the momentum reaches a maximum of $p_{\max} \approx 0.56$, clearly within the limits of $|p| \leqslant 0.75$ set by ΔV.

In the shallow scaling the maximum is $p_{\max} \approx 0.40$, which exceeds the limits of $|p| \leqslant 0.38$ for some times.

After the downconversion phase ends the particle again transitions to the free fall of the decoupled phase.

Capture Probabilities

The probability curves in Figure IV.4 were computed using the Wigner-Ville transform of the wave functions for the shallow and semi-classical scaling with $\Pi = 50$. They show the probability for a captured particle within the well, or within the separatrix if regarded in terms of the phase-space.

The probability is equal to zero as long as no bound states are possible. It is therefore possible to see the beginning (t_i) and the end (t_f) of the downconversion phase, where $t_i = -t_f$ because of the symmetry of $\beta(t)$.

For the semi-classical scaling this transition happens at $t_{i/f} \approx \pm 185$. The probability

quickly rises and reaches a maximum of $P = 0.72$ at $t \approx -100$. The curve stays at this value until an initially slow decline sets in at $t \approx 65$.

For the shallow scaling the downconversion lasts between $t_{i/f} \approx \pm 130$. A maximum value of $P = 0.57$ is reached around $t \approx -50$. But in this case the curve slowly declines, indicating a tunneling out of the well.

Phase-Space

The time evolution shown in Figure IV.5 features only one system: the shallow scaling. The other systems differ only in a few aspects. Most importantly, the semi-classical scaling does not show tunneling. Since the two $\Pi = 20$-systems have the probability for capture split between two wells, interference patterns appear of the Wigner functions in two separatrices appear, making it more difficult to visually discern important features.

The Wigner functions were obtained with the Phase-Space Evolution scheme. The Wigner-Ville transforms of the numerical wave functions are very similar. They are not shown here for brevity.

The trajectories are initially parabolic curves that gradually form into separatrices, then back to parabolas. The particle moves in the potential along these trajectories and spreads out, changing into a crescent shape.

When the separatrix forms a loop, the distribution is already present in that area of phase-space. The part of the Wigner function to the right of the separatrix cannot be captured and moves away, as it stays in the decoupled phase. The distribution moves slowly ($v \sim 0$) and the growing separatrix crosses over more of it. But the distribution is still partly outside, moving slowly away outside the separatrix.

The bound distribution starts to oscillate slowly, but keeps close to the separatrix. A continuous flow out of the separatrix shows the possible tunneling of the particle out of the well, comparable to the behavior seen in Figure III.4.

In the semi-classically scaled system the separatrix growth continues after the available distribution is already captured, leading to an increasing separation of the bound distribution from the separatrix. This effectively suppresses the tunneling of the particle. In this larger system the distribution is elongated as it moves around in phase-space and crosses the separatrix, forming a spiraled pattern. Due to the greater separatrix area it is able to persist longer. It also shows more distinct oscillations, apparently at different orbits giving these stripes seen in Figure IV.2d, when viewed as a projection on the q-direction.

When the separatrix area shrinks, the distribution eventually crosses over it and moves away along the classical trajectories.

This phase-space-picture shows the behavior of such a Daemon system very well and can be used to explain its distinct features that appear in the plots of the probability density and localization probabilities.

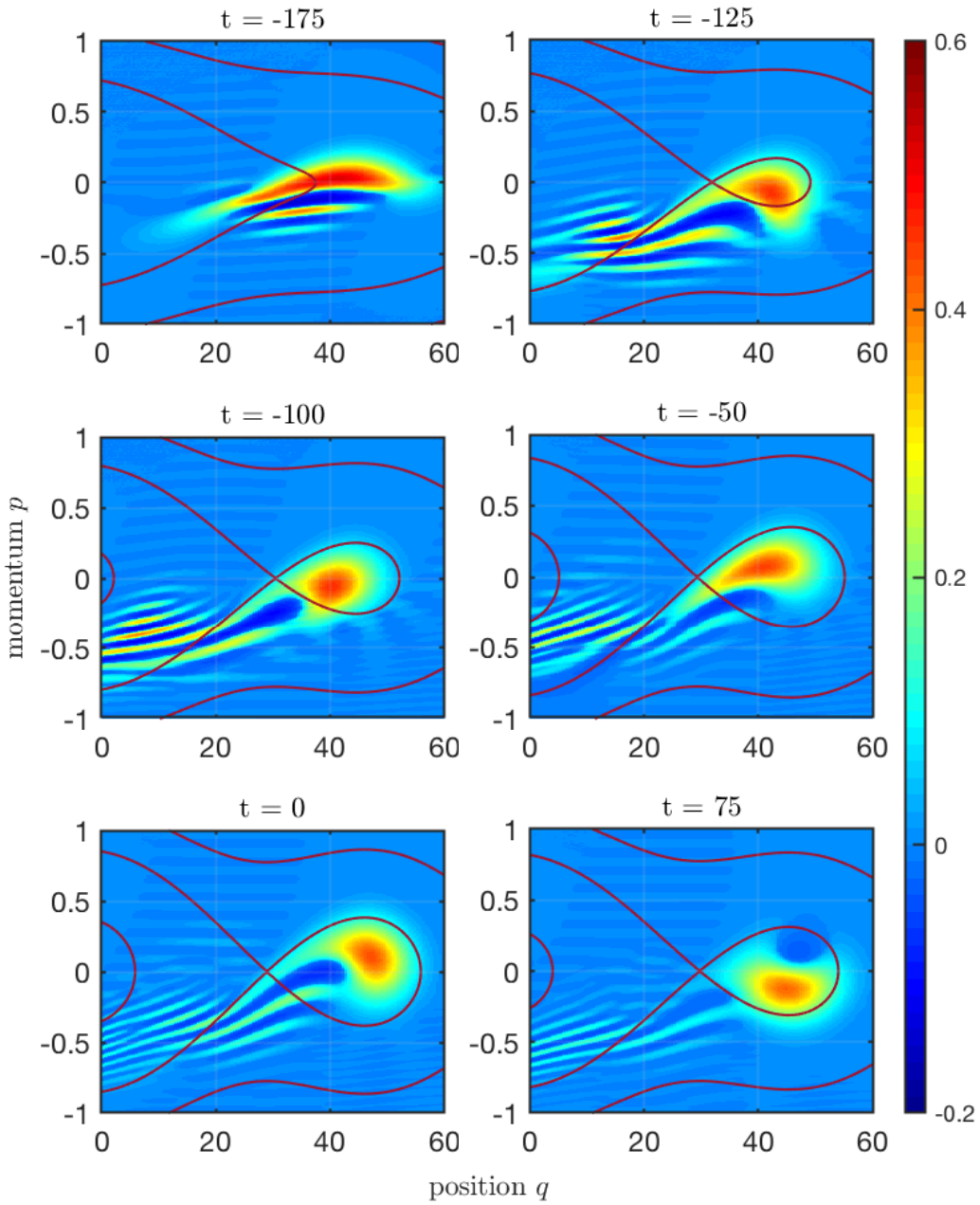

Figure IV.5.: The time evolution in phase-space of the tilted lattice with shallow wells at six time instances. The Wigner function was computed with the Phase-Space Evolution scheme.
The red lines indicate the separatrices.

2. Summary of the Time Evolution

On the basis of these numerical results the time evolution of the tilted lattice model is now examined. It shows behavior expected from a daemon system with a tilted washboard potential. It exhibits both dynamical phases: decoupling and downconversion.

Decoupling

The decoupled particle experiences free fall in the potential. This can be see in the density probabilities: in σ (Figure IV.3) as a declining straight line, corresponding to the downwards parabolic curves in ρ (Figure IV.2). In phase-space it is seen as basically anything outside an enclosed separatrix area.

By design the system is in the decoupled phase in the beginning and the end. In between the particle is decoupled either if it fails to transition to downconversion – the daemon motor does not to start – or if it tunnels out – corresponding to a premature stalling of the motor.

Transition

The transition to the downconversion phase sets in before the separatrix opens at t_i. This point in time is clearly visible in the probability curves (Figure IV.4) and marked accordingly in the ρ- and σ-plots. Deeper wells open comparatively faster, meaning that larger values for γ lead to smaller t_f.

Before that ($t < t_i$) the phase-space trajectories deform. The momentum distribution stays close to the critical speed $p \sim 0$ for an extended time if it is left[f] of the separatrix, or the fall is accelerated if the distribution is on the opposite side. In σ this is seen as a division. In a short period of time before t_i most of the distribution deviates from the straight line and reaches $p \approx 0$ at t_i. This is comparable to the behavior of the raising-barrier capture model in phase-space (Figure III.6), where the wave packet is partly reflected according to its momentum.

A difference in the transition process can be seen between smaller and larger values of γ, as in the the shallow respectively semi-classical scaling.

The semi-classical scaling shows the apex of the initial parabola – and thereby the zero-crossing of in the momentum – close to t_i. σ (Figure IV.3b) shows multiple streaks in the distribution at different values of p that curve towards downconversion, resulting in multiple modes of oscillations. It is possible to catch more regions of the distribution pertaining to lower momentum.

In the shallow scaling t_i is later, so the zero-crossing occurs long before that point in time. There is only one part of the distribution curving away from the decoupled fall, as no additional parts of the distribution have a momentum close enough to zero at t_i.

In phase-space the separatrix of the semi-classical scaling is larger and growing faster. It is therefore easier to catch the distribution before it moves away. The shallow scaling

[f] The trajectories are curved to the right in the mathematical sense.

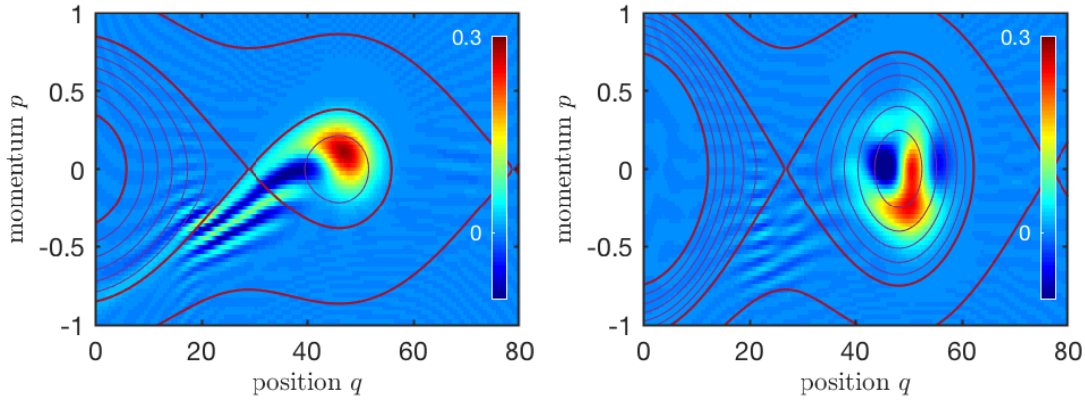

(a) $W(q,p)|_{t=0}$ in shallow scaling (b) $W(q,p)|_{t=0}$ in semi-classical scaling

Figure IV.6.: Comparison of Wigner function and trajectories at $t = 0$ for the shallow and semi-classical scaling in Figure IV.2c and IV.2d using the Wigner-Ville transform. The separatrix is in shown red. The additional classical trajectories[g] are evenly spaced with $\Delta E = 0.05$ in both cases.

also shows that a part of the distribution is simply outside of the separatrix due to its smaller area.

Generally speaking, the transition from the decoupled to the downconversion phase is more probable for deeper wells. This is clearly reflected in the plot of the probabilities: the curve of semi-classical scaling reaches a higher value ($P = 0.72$) than the shallow scaling ($P = 0.57$).

Downconversion

As expected from a tilted washboard potential, the downconversion phase appears as bound states. This is best seen in Figure IV.5, where all of the Wigner function within the separatrix exhibits downconversion. But both probability distributions ρ and σ the vastly different dynamics compared to the decoupled phase, with oscillations around a stable fixpoint instead of the free fall.

σ is similar to the previously published momentum distribution (compare Figure I.4), but without the jumps of the quantum regime. ρ can be compared to previous publications (Figure I.3) as well, but there are no bifurcations in the distribution with possibilities for a further rise (since $v_c = 0$ for the tilted lattice). However there is a chance for the decay of the (quasi-) bound state and tunneling is more likely to happen when the particle approaches the barrier. This can already be see in the decay model (*e. g.* Figure II.10).

The systems with differently scaled parameters (see Table IV.1) show different behavior, which is most distinct between smaller and larger values of γ. The quantum scaling (a) shows just one band of the spatial distribution within the wells, whereas the

[g] These are not Bohr-Sommerfeld orbits, although the number of additional curves lines up with N_{sc}.

small scaling (b) shows oscillations. This is similar for the $\Pi = 50$-systems, but the wells are larger in regards to q and allow for more movement of the bound particle. In the shallow scaling (c) small oscillations appear within the well, visible in both the ρ- and σ-plot. The semi-classical scaling (d) even exhibits multiple modes of oscillation, akin to an excited state. Figure IV.6b shows the Wigner function at $t = 0$. The distribution extends to the innermost region (around $p = 0$) as well as to a region of the separatrix further out (higher momentum). This can be regarded as two modes with partly overlapped distributions. In comparison the Wigner function in shallow scaling (Figure IV.6a) shows just one oscillating distribution. The inner region coincides with the separatrix as a whole.

Tunneling

Tunneling is present in systems of smaller γ (quantum and shallow scaling), but suppressed for larger γ (small and semi-classical scaling). This can be seen in Figure IV.6. The shallow scaling (left) shows a flow across the separatrix out of the region of down-conversion, as opposed to the semi-classical scaling (right), where the bound distribution is rather separated from the decoupled region. The probability curves in Figure IV.4 show this distinction. Such flow away from the well, apart form times around t_i, is also visible in the ρ-plots of the quantum (Figure IV.2a) and shallow (Figure IV.2c) scaling.

The suppression of tunneling in systems with deeper wells indicates a transition from the quantum to more classical behavior.

Flow and Capture in Phase-Space

The capture probability is given by the separatrix. The area determines how much of a distribution can be caught inside it at all. The growth rate competes with the flow of the distribution.

For this initial values are important. The parameters $\dot{\alpha}$ and γ determine the area and β the growth rate.

An unsuitable choice for the initial momentum p_0 of could mean the particle has already passed the area in phase-space relevant for capture, or it moves away outside the separatrix if it arrives to late. The distribution should be close to the stable fixpoint, once it emerges.

But a combination of parameters that leads to a successfully running daemon engine is not hard to find.

The behavior of the *tilted lattice model* in phase-space is similar to the description linked to *Kruskal's theorem* in Reference [10] – after all it is a quantum analog of the Hamiltonian H_2 in that publication. But in this case quantum corrections are present: tunneling out of the separatrix can occur, and tunneling into it as well, albeit much less likely. A quantum version of Kruskal's theorem could follow from an analytical description of this phase-space capture.

Simplified Daemon

Lastly some additions to this model regarding daemon systems are in order. There is no connection between different subsystems as such, *e. g.* no fuel, just parameters $\dot{\alpha}$ and γ which represent adiabaticity and coupling within the framework of daemon engines, but are chosen here somewhat arbitrarily, since no direct correlation with previous numerical examinations was possible. In part this is because of the methods employed here and in part due to the requirements formulated for and leading to the scaling of the systems.

All of the dynamical behavior comes from $\beta(t)$. This control parameter subsumes all of the time-dependence of more complex systems and the intricate interaction of the subsystems in a daemon engine.

IV.c. Beyond the Tilted Lattice Model

This section takes a look at quantum mapping and tries go beyond a simplified model.

First a quantum canonical transformation of the tilted lattice Hamiltonian is presented in analogy to the classical transformation in Reference [10].

Afterwards an exact quantum phase model representation is derived for a quantum daemon Hamiltonian.

Then some difficulties in dealing with quantum daemons are described.

1. Quantum Canonical Transformation of the Tilted Lattice

Separatrix engineering and control, based on Kruskal's theorem referenced in [10], was introduced in Section I.b.3 in the context of the classical Hamiltonian Daemon. The results of the previous section show that this could be extended to quantum dynamical descriptions within the description of phase-space quantum mechanics.

Furthermore Reference [10] describes a canonical transformation

$$\hat{q} \mapsto \hat{q}, \quad \hat{P} \mapsto \hat{p} = \hat{P} - \alpha(t) \tag{IV.2}$$

that shifts the momentum, changing the Hamiltonian:

$$H_1 = \frac{1}{2}\left(P - \alpha(t)\right)^2 - \beta^2(t)\cos(q) \tag{IV.3}$$

to the comoving Hamiltonian:

$$H_2 = \frac{1}{2}p^2 + \dot{\alpha}q - \beta^2(t)\cos(q). \tag{IV.4}$$

The tilted lattice Hamiltonian[h] $\hat{H}_{\mathrm{TL}}$ can be considered the quantum analog of H_2 by promoting the dynamic variables to operators. Now the quantum analogs of the transformation and the Hamiltonian H_1 are regarded.

[h] compare to Equation IV.1, with $\gamma\beta(t)$ substituted by $\beta^2(t)$ and the scaling by s dropped

Time-dependent Transformation of the Tilted Lattice

Here only the essentials needed to perform the transformation are given. Appendix A.ii contains more details on quantum canonical transformations in the WWGM-formalism and the reduction to ordinary exponentials.

The transformations are generally defined as:

$$\begin{aligned} \hat{F}(\hat{q},\hat{p})\,\hat{q}\,\hat{F}^{-1}(\hat{q},\hat{p}) &= \hat{Q}(\hat{q},\hat{p}) \\ \hat{F}(\hat{q},\hat{p})\,\hat{p}\,\hat{F}^{-1}(\hat{q},\hat{p}) &= \hat{P}(\hat{q},\hat{p}) \\ -i\,\left[\hat{Q},\hat{P}\right] &= 1 \end{aligned} \tag{IV.5}$$

where $\hat{F}$ is the generating function and $\hat{F}^{-1}$ its algebraic inverse.

Three elementary canonical transformations can be assumed, making others combinations thereof[i]:

1. gauge transformation
2. point transformation
3. interchange of position and momenta

Classically, the time-dependency of a transformation is considered by time-derivative of the generator. In the quantum case the description of the momentum operator in position space $\hat{p} \equiv \hat{p}_q = -i\,\partial_q$ is extended to time: $\hat{p}_t = -i\,\partial_t$ (the energy operator), which is then transformed as well. With this the Schrödinger equation reads $\hat{p}_t\,|\psi\rangle = \hat{H}\,|\psi\rangle$.

The specific type of transformation used here is the *one-variable similarity* (or *gauge*) transformation, given by:

$$\begin{aligned} \hat{q} \mapsto \hat{Q} &= e^{f}\,\hat{q}\,e^{-f} = \hat{q}, \\ \hat{p} \mapsto \hat{P} &= e^{f}\,\hat{p}\,e^{-f} = \hat{p} + i\partial_q f, \\ \hat{p}_t \mapsto \hat{P}_t &= e^{f}\,\hat{p}_t\,e^{-f} = \hat{p}_t + i\,\partial_t f, \end{aligned} \tag{IV.6}$$

with the generating function $\hat{F} = e^{-f(\hat{q},t)}$.

A function $g(\hat{q},\hat{p})$ transforms as: $g(\hat{q},\hat{p}) \mapsto e^{f}\,g\,e^{-f} = g(\hat{Q},\hat{P})$, thus the Hamiltonian is transformed:

$$\hat{H}(\hat{q},\hat{p}) \mapsto e^{f}\,\hat{H}\,e^{-f} = \hat{K}(\hat{Q},\hat{P}) \tag{IV.7}$$

where $\hat{K}$ is used for the transformed Hamiltonian, also called the *Kamiltonian*.

[i] This at least true for a large number of transformations.

At first a general case is considered, where $f = i\,\Theta(\hat{q}, t)$ is set for the generator. The transformation is time-dependent and unitary. An expression for Θ specific to the the tilted lattice is chosen later. The resulting transformations for the momentum operators are:

$$\hat{p} \mapsto \hat{p} - \Theta', \quad \hat{p}_t \mapsto \hat{p}_t - \dot{\Theta}. \tag{IV.8}$$

Now the *Schrödinger-operator* $\hat{\mathscr{H}} = \hat{H} - \hat{p}_t$ is regarded, which contains $\hat{p}_t$ and thereby takes the time-dependency into account. With this, the Schrödinger equation is shortened to $\hat{\mathscr{H}}\,|\psi\rangle = 0$.

The Schrödinger-operator transforms as:

$$\hat{\mathscr{H}} \mapsto \hat{\mathscr{K}} = \hat{K}(\hat{Q}, \hat{P}) - \hat{P}_t \tag{IV.9}$$

$$= -\hat{P}_t + \tfrac{1}{2}\hat{P}^2 + \dot{\alpha}\hat{q} + \beta^2(t)\cos(\hat{q}) \tag{IV.10}$$

$$= -\hat{p}_t - \dot{\Theta} + \tfrac{1}{2}\left(\hat{p} - \Theta'\right)^2 + \dot{\alpha}\hat{q} + \beta^2(t)\cos(\hat{q}). \tag{IV.11}$$

This works, if β^2 does not depend on $\hat{p}$. Otherwise it would have to be transformed as well: $\beta^2(\hat{p}, t) \mapsto \tilde{\beta}^2(\hat{P}, t)$

The tilt can be eliminated by choosing $\dot{\Theta} = \dot{\alpha}\,\hat{q}$. From this follows:

$$\Theta = \dot{\alpha}\,(t - t_0)\;\hat{q} = \alpha(t)\,\hat{q}. \tag{IV.12}$$

For this gauge transformation here, the generating function $\hat{F}_G = e^{i\int \mathrm{d}q\,\theta(\hat{q},t)}$ has the effect of a transformation $\hat{p} \mapsto \hat{p} + \theta(\hat{q}, t)$ with $\theta = \dot{\alpha}(t - t_0) = \Theta'$, resulting in:

$$\Theta = \alpha(t)\,\hat{q}, \qquad \Theta' = \alpha(t), \qquad \dot{\Theta} = \dot{\alpha}\,\hat{q}, \tag{IV.13}$$

which can be put in Equation IV.11.

The complete transformation of the tilted lattice Hamiltonian now reads:

$$\hat{F}_G = e^{i\alpha(t)\hat{q}} \tag{IV.14}$$

$$\hat{q} \mapsto \hat{q}, \qquad \hat{p} \mapsto \hat{p} - \alpha(t), \tag{IV.15}$$

$$\hat{H}_{\mathrm{TL}} \mapsto \hat{K}_{\mathrm{TL}} = \frac{1}{2}\left(\hat{p} - \alpha(t)\right)^2 + \beta^2(t)\cos(\hat{q}). \tag{IV.16}$$

The transformed Hamiltonian $\hat{K}_{\mathrm{TL}}$ (IV.16) can be seen as the quantum version of H_1 (IV.3). The transformation in Equation IV.15 is then the quantum analogue of the classical canonical transformation from the perturbed pendulum H_1 to the tilted washboard H_2 in [10].

The quadratic term in $\hat{K}_{\mathrm{TL}}$ can be expanded:

$$(\hat{p} - \alpha)^2 = \hat{p}^2 - 2\alpha\hat{p} + \alpha^2. \tag{IV.17}$$

In position basis $\hat{p} = -i\partial_q$, introducing an additional derivative to the Schrödinger equation. The Crank-Nicolson method is not well suited for this type of equation and the Phase-Space Evolution scheme would require a different propagator. The transformed system was therefore not examined numerically.

In the following section such systems will be briefly introduced as advection-diffusion systems.

2. Exact Quantum Phase Model of the Quantum Daemon Engine

The *exact quantum phase model* (EQPM) is based on Reference [41]. It was developed in the context of Josephson Junctions, but it is used here to describe the Hamiltonian daemon engine. It starts from a two-mode *Bose-Hubbard* model – which is also a possible model for the description of the fuel system in Hamiltonian daemons – and treats the phase term ϕ as a quantum mechanical coordinate.

The idea is to take the quantum Hamiltonian and rewrite it to eliminate the angular momentum operators from the potential. For that purpose the EQPM replaces the annihilation and creation operators by their action on states via associated functions.

In the end, the approach did not prove to be fruitful, therefore only an overview with the important results is presented here. Derivations and other technical details and can be found in Appendix C.iv.

Starting point is the the quantum Hamiltonian (Equation I.5):

$$\hat{H} = \frac{1}{2M}\hat{P}^2 + Mg\hat{\Omega} + \Omega\hat{L}_z - \frac{\gamma}{2}\left(\hat{L}_- e^{ik\hat{q}} + \hat{L}_+ e^{-ik\hat{q}}\right), \tag{IV.18}$$

which can be rewritten for this problem as the *quantum engine Hamiltonian*:

$$\hat{H}_{\mathrm{qe}} = \frac{1}{2}\left(\hat{S}_z - \hat{\alpha}\right)^2 + \frac{1}{2}\gamma_0\left(\hat{S}_- + \hat{S}_-^\dagger\right) \tag{IV.19}$$

by defining $\alpha(t) = \dot{\alpha}(t - t_0)$ with $\dot{\alpha} = \frac{mg}{k}$ and rescaling to dimensionless variables and quantities. Furthermore the annihilation operators $\hat{a}_-$ are substituted by $\hat{b}_- = \hat{a}_- e^{-ik\hat{y}}$. This also changes the $\hat{L}$-operators to in Equation IV.18 to the corresponding $\hat{S}$-operators to in Equation IV.19.

With these substitutions it can be seen that the quantum engine Hamiltonian resembles the effective daemon Hamiltonian (Equation I.6). A more complete derivation is given in Appendix C.iii.

Applying the representations of the EQPM to Equation IV.19 results in the Hamiltonian:

$$\hat{H}_{\mathrm{EQPM}} = -\frac{1}{2}\partial_\phi^2 + (\gamma_0 \sin(\phi) - i\alpha)\,\partial_\phi + \alpha^2 + \frac{1}{2}\gamma_0\,(N+2)\cos(\phi), \tag{IV.20}$$

where the time-dependence is given by $\alpha(t) = \dot{\alpha}(t - t_0)$ and the quantum mechanical coordinate ϕ. This already resembles the Hamiltonian of a daemon system. By shifting the representations in the EQPM the states and heir inner product are changed as well[41] as well. The inner product then features a cutoff at the finite particle number N, depending on the particular system, which matches the tank system of a daemon engine, which consists of N particles.

Additionally the Schrödinger equation $\hat{H}_{\mathrm{EQPM}}\,|\psi\rangle = i\partial_t\,|\psi\rangle$ can be regarded. Transforming the states via $|\psi\rangle = e^{-\arg}\,|\Psi\rangle$ effectively changes the Hamiltonian in order to achieve different properties of the model.

Here, two choices for the argument $\mathcal{A}$ are presented that aim at different goals:

The first attempt aims at eliminating the ∂_ϕ-term, since it could prove bothersome for numerical computations. The choice for the argument is:

$$\mathcal{A}_1(\phi, t) = -\left(\gamma_0 \cos(\phi) + i\alpha(t)\phi\right), \tag{IV.21}$$

which results in the Hamiltonian:

$$\begin{aligned} \hat{H} &= \frac{1}{2}\hat{p}^2 + \tilde{V}(\phi, t), \\ \tilde{V}_1 &= 2\gamma^2 \sin^2(\phi) + \gamma_N \cos(\phi) - \frac{\epsilon^2}{2} + 2\gamma\epsilon \sin(\phi) + 2\dot{\epsilon}\phi, \end{aligned} \tag{IV.22}$$

where $\dot{\epsilon} = i\dot{\alpha}$, $\gamma = \frac{1}{2}\gamma_0$, and $\gamma_N = \gamma N$.

The Hamiltonian shows the tilt and the time-dependent wells in the potential akin to a tilted washboard. However, the time-dependence is now imaginary and the resulting Schrödinger equation proves to be non-hermitian and non-$\mathcal{PT}$-symmetric[42,43] and is therefore not likely to lead to a physically relevant system.

From this follows the second aim: gaining a hermitian Schrödinger equation. The transformation is performed with the argument

$$\mathcal{A} = -\gamma \cos(\phi) + i\lambda(\phi + 2\lambda - 2\sin(\phi)), \tag{IV.23}$$

which now gives:

$$\begin{aligned} \hat{H}_{\mathrm{ADR}} &= \frac{1}{2}\hat{p}^2 + C(\phi, t)\,\hat{p} + \tilde{V}(\phi, t), \\ C(\phi, t) &= 4\gamma\alpha \cos(\phi), \end{aligned} \tag{IV.24}$$

$$\tilde{V}_2(\phi, t) = \dot{\alpha}\phi + \gamma_N \cos(\phi) + 2\gamma^2 \sin^2(\phi) - 4\gamma\dot{\alpha} \sin(\phi) + \alpha^2(8\gamma^2 \cos^2(\phi) + 1),$$

where $\gamma = \frac{1}{2}\gamma_0$ and $\gamma_N = \gamma(N-1)$. However, this transformation is not unitary.

This will be called the advection-diffusion-reaction Hamiltonian (ADR). The terminology resorts to classical problems involving advection[44] (or convection), where the ∂_ϕ^2-term describes *diffusion*, the ∂_ϕ-term describes *advection* or *drift* with a coefficient C and the last term, *i. e.* the potential, describes *reactions* as sources or sinks. The Schrödinger equation corresponding to $\hat{H}_{\text{ADR}}$ is not in the usual form of advection-diffusion equations. The advection coefficient $C = 2i\gamma\,\alpha(t)\cos(\phi)$ in Equation IV.24 is a function in ϕ and t.

In addition to the advection-term[j] the potential also shows the properties of a tilted washboard.

This model was briefly numerically examined. For this purpose a finite difference scheme on the basis of the general *Crank-Nicolson*-ansatz has been developed.

The initial results did show the decoupling- and downconversion-phase, strongly resembling the dynamics of the classical daemon. But two major problems with the numerics did arise. The results changed drastically with variations in the underlying grid. Additionally, the phase-space-picture showed odd behavior, where the Wigner functions showed oscillations wildly crossing the separatrix areas. The numerical results are therefore not presented here.

A further analysis in search for the correct form of the phase-space-trajectories then lead to examination of canonical transformations of the system.

A quantum canonical transformation can eliminate the advection term by shifting the momentum (see C.v):

$$\begin{aligned} \hat{q} \mapsto \hat{q}, \quad \hat{p} \mapsto \hat{P} = \hat{p} + C(\hat{q}, t), \\ \hat{H} = \frac{1}{2}\hat{p}^2 + C\,\hat{p} + V \;\mapsto\; \hat{K} = \frac{1}{2}\hat{P}^2 + U, \end{aligned} \tag{IV.25}$$

where the transformed potential $U = W + i\Gamma$ now exhibits an imaginary part that results from the commutator of $\hat{p}$ and $C(\hat{q}, t)$.

Applying this transformation to the ADR-Hamiltonian of Equation IV.24 results in the potential:

$$U = \dot{\alpha} + \gamma_N \cos(\phi) + 2\gamma^2 \sin^2(\phi) - 8\gamma^2\alpha^2 \cos^2(\phi) - 2i\gamma\alpha \sin(\phi) + \alpha^2, \tag{IV.26}$$

which can be further reduced to:

$$U_{\text{r}} = \dot{\alpha} + \gamma_N \cos(\phi) + 2\left(2\gamma\alpha\cos(\phi)\right)^2 - 2i\gamma\alpha\sin(\phi) \tag{IV.27}$$

by leaving out terms that would not contribute to the dynamical behavior of the system. This potential now clearly describes the tilt and the washboard-like wells, but with an additional imaginary term.

The problems with this model so far have been:

[j] The p-dependent term already appears in $\hat{K}_{\text{TL}}$ IV.16 or classical daemon Hamiltonians with $(p-\alpha)^2$.s

- questions about the nature of the wave functions and the inner product,
- the hermiticity of Hamiltonians and the unitarity of transformations,
- instabilities in the numerical computations and
- the emergence of an imaginary term in the potential after the canonical transformation.

Furthermore, the transformed Hamiltonian resembles the *tilted lattice* model which has been examined in this thesis.

There could be ways to treat this model with different techniques, both analytical and numerical. This is picked up briefly in Section VI.b.

3. Difficulties with the Treatment of Quantum Daemons

The study of further – more complex – systems within the scope of this thesis and its methodology proved to be rather difficult. Several approaches were discarded as they were considered as unfeasible.

The effective Hamiltonians describing a daemon engine (Equation I.4 or I.3) involve momentum-dependent potentials or other additional terms that scale with p or some angular momentum J through the action F. Simply taking a classical Hamiltonian $\mathcal{H}(q,p;t)$ with a p-dependent potential $V(q,p;t)$ raises the question of the correct quantization procedure. Can the usual approach of $q \to \hat{q}, p \to \hat{p}$ work?

The quantum canonical transformation of the tilted lattice shows that there exist simple quantum analogs of classical systems in which even the canonical transformation works. The quantization of classical Hamiltonians should work as usual[k].

But the problems with handling momentum-dependent potentials remains, especially in numerical evaluations.

Taking the genuine quantum Hamiltonian lead to the exact quantum phase model representation to get rid of problematic terms. This approach itself turned out to be not quite successful.

[k] The correspondence of classical and quantum daemon Hamiltonians is also seen based on [7] in conjunction with [6].

V. Uniting Hamiltonian Daemons in Semi-Classical Phase-Space

This chapter strives to find a unifying theory for Hamiltonian daemons that can describe both the classical and quantum behavior. To this end, the classical phase-space is quantized and characteristics of daemons in the deep quantum regime are connected to phenomena in such a phase-space.

A first step of bringing together classical and quantum daemons is the phase-space formalism of quantum mechanics. It was introduced in chapter III and the model of chapter IV showed its potential for the description of quantum daemons. The tilted lattice model showed quantum behavior for small systems and a suppression of quantum effects (*i. e.* tunneling) in larger systems. Additionally an extension to a quantum Kruskal theorem was hinted at. The WWGM-formalism contains the classical Liouville equation as the limiting case of the Moyal equation.

V.a. Summary of Classical and Quantum Daemons

As stated in the introduction to Hamiltonian daemons (see Section I.b.3) the dynamical behavior of the classical daemon engine can be well described in terms of the phase-space as shown in Figure V.1. The downconversion phase is seen as bound orbits around a stable fixpoint, enclosed by a separatrix. The fixpoint drifts toward lower fuel levels and transports the separatrix and the orbits with it. The unbound trajectories exhibit adiabatic decoupling. They can cross over to downconversion through post-adiabatic effects near a time-dependent separatrix.

In contrast, the canonical formulation of quantum mechanics does not allow a phase-space description. Instead the energy transfer between the subsystems of a quantum daemon engine is described by a series of avoided crossings in the instantaneous eigenspectrum of the Hamiltonian, as depicted in Figure V.2 or I.8a. These crossings are described by adiabatic Landau-Zener transitions.

V.b. The Semi-Classical Phase-Space and Dynamical Tunneling

1. The Quantized Phase-Space

A semi-classical phase-space would mean a combined theory of adiabatic transport in Hamiltonian engines, that contains the description of classical as well as quantum behavior and allows to revert to phase-space quantities.

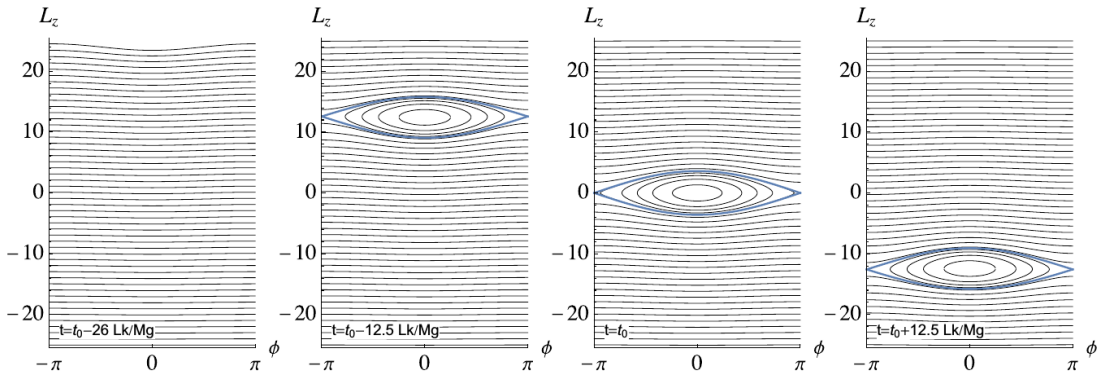

Figure V.1.: from [7]; Contours of constant instantaneous eigenenergies given by the classical limit in the horizontally periodic (ϕ, L_z)-plane at different times. L_z corresponds to the fuel variable F in Figure I.6. The separatrix is shown in blue. The other contours are given by semi-classical Bohr-Sommerfeld energy levels.

Two issues need to be clarified:

1. the movement and the growth of the separatrix area in the classical regime, and
2. the transition (or tunneling) between different $|m\rangle$-states in the quantum regime.

Dynamical tunneling serves as a description of transitions between regions in phase-space.

But first a quantization of the classical phase-space is needed in order to find a connection to the quantum states.

The Hamiltonian is expressed in terms of action-angle-variables (ϕ, F) (see the rescaled effective Hamiltonian in I.4). The action F is now quantized via the Bohr-Sommerfeld method which gives rules for the allowed orbits. Such a procedure was already described in [7] and the result (in the classical limit) is shown in Figure V.1.

From the quantum description of daemons follows a direct correlation of the relative occupation numbers m to the action F. Within the separatrix are quantized bound orbits, outside the free trajectories.

The probability for fuel numbers (compare Figure I.8) indicates the possibility to use the expectation value of the fuel occupation numbers as a (quasi-) continuous spectrum, in line with the F-axis of the classical phase-space.

This concludes the introduction of the semi-classical phase-space. For the dynamical description the behavior of the separatrix and the diabatic transitions have to be discussed.

2. Transitions as Dynamical Tunneling

The separatrix is defined analogously to the classical theory. Its increasing area can sustain a growing number of bound orbits. The downwards movement then transports

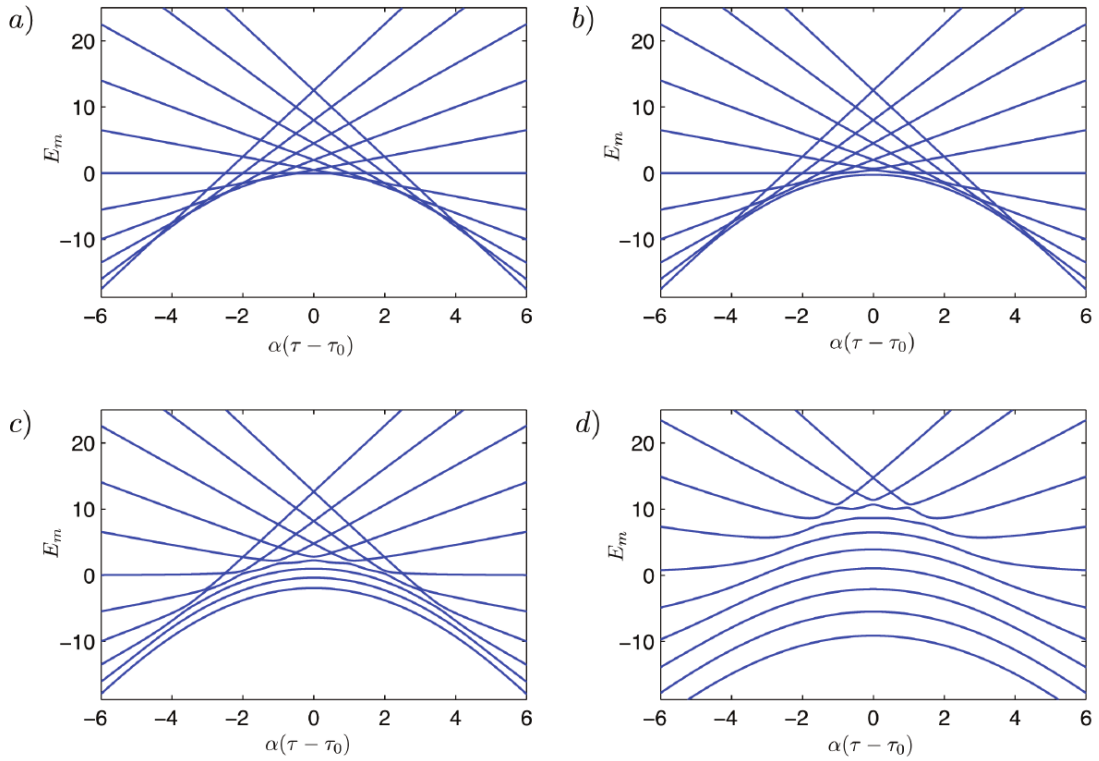

Figure V.2.: from [8]; multiple eigenspectra of quantum Hamiltonian showing possible crossings of instantaneous energy levels E_m belonging to different states $|m\rangle_f$. The panels show different degrees of adiabaticity, lifting the degeneracy of the crossings.

the bound orbits with it.

A particle, described by a phase-space distribution, moving along a free trajectory, can be captured on a bound orbit by crossing over the separatrix. The additional orbits due to separatrix growth then isolate this bound particle. The basics of such an isolation were already seen in the phase-space picture of the semi-classically scaled tilted lattice simulation (Figure IV.6), where it lead to a suppression of tunneling. The difference between classical and quantum behavior would then be given by the separatrix area[a] and the separation of bound particles and free trajectories. Orbits further out from the stable fixpoint correspond to systems that are not fully excited initially, leading to higher order crossings[b].

So far, capture and transport can be explained without resorting to quantum theory. However, it comes into play when describing tunneling: leaving a bound orbit prematurely and transitioning to an unbound trajectory.

For this tunneling is not just limited to the penetration of a potential barrier. It

[a] This was already used in the introduction to define the *deep quantum regime*.
[b] regarded in [8]

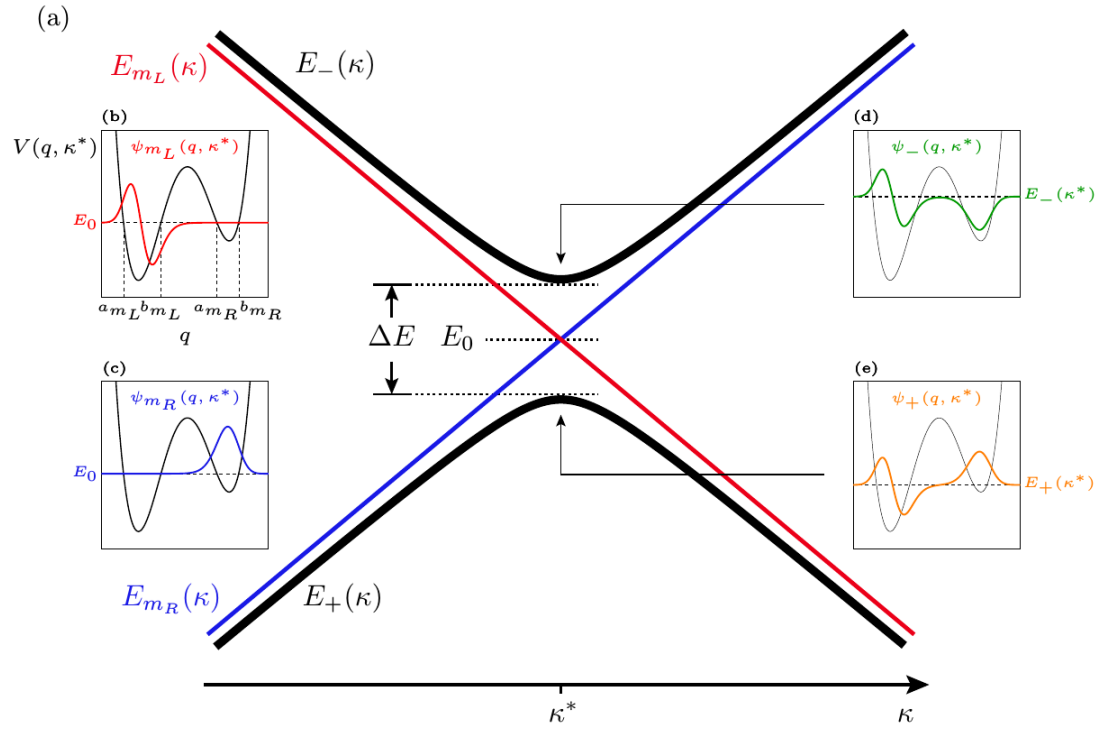

Figure V.3.: from [45]; The tunneling in a double well potential is connected to avoided crossings in the energy spectrum.

is extended to *dynamical tunneling*, which describes transitions between any separate dynamical regions – like the different regions of the decoupled and the downconversion in the phase-space of Hamiltonian daemons. The description commonly involves a *regular island* – *i. e.* bound orbits of the downconversion phase – embedded in a *chaotic sea* – the trajectories showing adiabatic decoupling.

But the connection between Hamiltonian daemons and quantum chaos is not clear. The answer could lie in the *Chirikov standard map*[46] or the examination of a perturbed pendulum system[45]. Both are standard examples of the corresponding literature on dynamical tunneling and bear resemblance to the description of daemons.

Assuming such a connection could be stated, Hamiltonian daemons could then be described as a mixed regular-chaotic system and resonant regular-to-chaotic tunneling processes[47] would be a suiting description[c] of the transition from a bound state to the surrounding chaos.

The link between avoided crossings and dynamical tunneling, however, has been established in literature[45]. To illustrate this, the example of a double well potential is used (see Figure V.3). The wave functions in the left and right well cannot be treated independently. These wave functions can be coupled symmetrically and an anti-symmetrically. The corresponding energies $E_{m_L}(\kappa)$ (left) and $E_{m_R}(\kappa)$ (right) cross at κ^*, but the cou-

[c] or at least starting point

pled energies $E_{-}(\kappa)$ and $E_{-}(\kappa)$ avoid the crossing and exhibit an energy splitting ΔE. This splitting indicates a tunneling probability. Thus a tunneling between two wells in a potential is directly connected to an avoided crossing, which presents as dynamical tunneling between different dynamical regions in phase-space.

V.c. Proposed Characteristics of a Unified Theory

These bits and pieces will now be summed up and arranged more clearly.

The phase-space is quantized semi-classically according to the Bohr-Sommerfeld procedure. This couples the orbits to occupation numbers of the fuel subsystem.

This phase-space is then mapped to a different representation, usually involving regular islands within a chaotic sea, that facilitates a description of dynamical tunneling processes. These processes portray the transitions from a bound orbit to an unbound state.

The *separatrix* moves through phase-space towards lower fuel values. The fixpoint indicates the m-value, and the orbits around it are quantized in units of F.

An additional growth of the separatrix area can sustain more orbits, leading to more distance between the innermost orbit and the separatrix. Thus tunneling is more prevalent in the early evolution and increasingly suppressed afterwards, comparable to the change in the probability of Landau-Zener transitions.

The *adiabatic evolution* of a particle in such a system corresponds to a transport within the separatrix on the innermost orbit. Diabatic transitions then correspond to a dynamical tunneling process out of the regular region. Higher order crossings are correlated to orbits closer to the separatrix.

Still open is the connection, respectively mapping, of Hamiltonian daemons to the chaotic quantum systems that form a basis of dynamical tunneling descriptions. Aside from that the theoretical background and mathematical elaboration of such systems need clarification.

The gain could be semi-classical description of daemons on the basis of phase-space quantities and processes. A confirmation of this proposal could unify the classical and quantum mechanical behavior of Hamiltonian daemons.

VI. Concluding Remarks

VI.a. Summary

Numerical Methods

Two different methods were employed for numerical results.

1. The *Crank-Nicolson method* (Section II.b) finds solutions to the Schrödinger equation with a finite difference approximation.
   Additionally the resulting wave functions $\psi(q)$ were transformed to Wigner functions $W[\psi](q,p)$ by the *Wigner-Ville transform* (Section III.b).

2. The *Phase-Space Evolution scheme* (Section III.c) computes the time evolution of Wigner functions according to the Moyal equation by using a split operator method.

The results of the Crank-Nicolson method are expectedly good – as it is an established numerical scheme for the Schrödinger equation – and are generally in agreement with theoretical predictions. Problems arose with the discretization. Especially the decay model with the cosine-barrier needed a rather fine grid. Reflections due to the lack of adequate (*i. e.* transparent) boundary conditions commended the use of large spatial domains.

Both methods for Wigner functions deliver results that are in agreement with each other, although they are based on different equations for the time evolution and different numerical schemes (compare Figure III.14).

The Wigner-Ville transform is especially useful if wave functions are available, but it can be lacking adequate resolution in the momentum p.

The Phase-Space Evolution scheme still allows the computation of probability densities $\rho(q)$ and $\sigma(p)$ without the wave functions, but it can lead to problems with the normalization and negative values in the probability values and densities. However, it has great potential as it can be used with different propagators for other systems in phase-space, *e. g.* classical Liouvillian or open quantum systems.

Example Models

Numerical results were obtained for several introductory models:

- the tunneling through a barrier,
- the decay of quasi-stationary state and

- the capture of a particle in a potential well.

This showcased the methodology used later for the study of a Hamiltonian daemon.

The characteristics of these example systems and their time evolution were examined. The evolution of Wigner functions was of particular interest, since it extends the classical phase-space to a semi-classical framework and allows a first look at how quantum corrections emerge there.

These models all exhibited some behavior which also occurs in Hamiltonian daemons.

The tunneling model showed barrier interaction which is a substantial part of all the other models.

The decay models showed the time evolution of quasi-bound particles, which can move out of a potential well by tunneling through the barrier. This was in prepared the description of a mechanism for the premature stalling of a daemon engine and was accompanied by analytical expressions of system parameters, *i. e.* the decay width Γ and the the non-decay probability.

The two capture models exemplified how bound states could be gained from an initially free wave packet.

Tunneling into a well showed how this could be achieved purely through a quantum effect. In classical phase-space this process violates Liouville's theorem, but the extension to quantum mechanics and the Moyal equation enables the phase-space distribution describing the particle to cross over the separatrix into the bound region.

For daemon systems a more classically inclined mechanism showed to be of greater impact. A time-dependent barrier makes it possible to capture parts of a phase-space distribution in a growing separatrix area.

These models showed that certain phenomena of semi-classical Hamiltonian daemons can be examined in simpler models, with the possibility for analytic descriptions.

Tilted Lattice Model

The tilted lattice was studied as a simplified version of a daemon system's Hamiltonian. It can be regarded as the quantum analog of a classical Hamiltonian in a previous publication.

Four systems with differently scaled parameters were examined. The tools that were devised alongside the example models were employed for this purpose.

The numerical results show the typical behavior of a daemon engine with a tilted washboard potential. A free particle can be trapped in local potential wells, thereby transitioning from the decoupled to the downconversion phase. Tunneling can be observed depending on the system parameters. This can lead to corrections of the engine's runtime.

The phase-space picture is very well suited for the evaluation of the time evolution. It indicates the possibility to extend Kruskal's theorem into the (semi-classical) quantum regime.

Going beyond the simplified model proved to be difficult. A representation of a quantum daemon Hamiltonian in the exact quantum phase model was obtained, but it showed several problems.

Daemons in Semi-Classical Phase-Space

The last chapter introduced the possibility of unification of classical and quantum daemons on the basis of a semi-classical phase-space description. Some aspects of this proposal were already published previously and put together here.

The phase-space is quantized by the Bohr-Sommerfeld procedure. Avoided crossings in the instantaneous energy spectrum of the deep quantum regime are connected to dynamical tunneling processes.

However, several parts of this approach are still unclear.

VI.b. Outlook

There are a couple of questions and approaches to problems left open, offering opportunities for future research.

The quantization of classical Hamiltonians with momentum-dependent potentials is still unclear. Using new techniques for the exact quantum phase representation could lead to further discoveries. Additionally the numerical evaluation of such Hamiltonians, as well as systems involving advective terms, needs different approaches.

The phase-space description of quantum daemons can be extended. The processes of capturing distributions in time-dependent separatrices was only seen in numerical simulations here. It lacks an analytical description, which means that a quantum version of Kruskal's theorem is needed.

The Phase-Space Evolution scheme that was introduced here has great potential for different types of systems. A direct comparison of classical and quantum behavior could be done, or open systems could be considered.

The representation of the Hamiltonian of a quantum daemon in the exact quantum phase model seemed to be unfeasible. But for the numerical treatment a different scheme could be employed. A finite difference approximation can be problematic for convective models, and a finite elements method would probably be better suited. Also, a further analytical examination could provide new insights, for example by searching for non-decay solutions for the imaginary potential or by looking further into the $\mathcal{PT}$ symmetry of the system, perhaps by splitting the Hamiltonian into parts of different symmetry.

Lastly, the unifying theory remains a hypothetical proposal. The relation of this semi-classical daemon in phase-space to quantum chaos needs to be explained.

Appendices

A. Alternative Formulations in the Theory of Mechanics

This part delves into the alternatives to the standard formulations of classical and quantum dynamics.

First, the WWGM-formalism is presented to describe the time evolution of quantum mechanical phase-space distributions. Second, a reformulation of classical mechanics is introduced, incorporating operators on a Hilbert space. This results in an operational approach to phase-space dynamics.

A.i. Quantum Mechanics on Phase-Space

There are several introductory texts on a phase-space description of quantum mechanics, among them References [28, 29, 48, 49], which form the basis for this section. Additionally, Reference [50] contains a section on selected publications.

Three autonomous ways of quantization have been formulated:

- operators acting on elements of a Hilbert space, the standard formulation,
- path integrals and
- the phase-space formulation, based on Weyl-quantization.

Quantum theory in phase-space is based on Wigner's quasi-probability distribution[51] and Weyl's correspondence[52], linking operators and ordinary c-number functions via representations in group theory.

The composition structure is given by the $\star$-product, formulated by Groenewold[30], and the dynamical evolution is described by Moyal's equation[31].

Thus, the framework of phase-space quantum mechanics will be referred to as the *Weyl-Wigner-Groenwold-Moyal-formalism* (WWGM-formalism).

The Weyl transform (or Weyl-map) maps phase-space functions to the corresponding operators in Hilbert space[28], whereas the Wigner transform (or Wigner-map) is its inverse[a].

[a] This does not seem to be used consistently in literature.

Framework of Weyl-Quantization

The Wigner quasi-probability distribution[29]

$$W(q,p) = \frac{1}{2\pi} \int \mathrm{d}y \left\langle q - \frac{\hbar}{2} y \right| e^{-iyp} \left| q + \frac{\hbar}{2} y \right\rangle \tag{A.1}$$

represents a system in a mixed state given by the density matrix $\hat{\rho}$.

For a pure state $|\psi\rangle$ this is given by $\hat{\rho} = |\psi\rangle \langle\psi|$. In the position basis it is expressed as $\langle q| \hat{\rho} |q'\rangle$. The density operator can easily be generalized to mixed states[48], leading to the definition:

$$W(q,p) = \frac{1}{2\pi} \int \mathrm{d}y \; \psi^* \left(q - \frac{\hbar}{2} y \right) e^{-iyp} \, \psi \left(q + \frac{\hbar}{2} y \right). \tag{A.2}$$

Some properties of the Wigner function $W(q,p)$ are:

- It is normalized: $\int \mathrm{d}q \; \mathrm{d}p \, W = 1$,
- It is real and bounded by: $-\frac{2}{\hbar} \leqslant W \leqslant \frac{2}{\hbar}$,
- Expectation values are given by: $\langle G \rangle = \int \mathrm{d}q \; \mathrm{d}p \, W(q,p) \, g(q,p)$ with a classical kernel g of G,
- The projections on q and p are positive, semi-definite probability distributions (marginal distributions):

$$\int \mathrm{d}p \, W = \rho(q), \quad \int \mathrm{d}q \, W = \sigma(p), \tag{A.3}$$

- Negative values occur in some areas of phase-space, but the areas are small.
- Smoothing of W is possible, e.g. with a phase-space Gaussian, resulting in the positive semi-definite Husimi Q-representation,
- W is the generator of all autocorrelation functions.

The Wigner function W for a given Hamiltonian H is found through Moyal's equation (where $f \equiv W$):

$$\partial_t f = \frac{1}{i\hbar} \left(H \star f - f \star H \right) = \{\{H, f\}\} \tag{A.4}$$

This can be regarded as the quantum mechanical extension of *Liouville's equation* in classical mechanics and is similar to Heisenberg's equation of motion.

The $\star$-product in Equation A.4 is defined as:

$$\star \equiv \exp\left(\frac{i\hbar}{2} \left(\overleftarrow{\partial_q} \overrightarrow{\partial_p} - \overleftarrow{\partial_p} \overrightarrow{\partial_q} \right) \right), \tag{A.5}$$

which itself is used to define the Moyal-bracket $\{\{\cdot,\cdot\}\}$, the quantum extension of the *Poisson-bracket*.

The $\star$-product is an exponential of differential operators and can be evaluated using *Bopp-shifts*[40,53]:

$$f(q,p)\star g(q,p) = f\left(q+\frac{i\hbar}{2}\overrightarrow{\partial}_p, p-\frac{i\hbar}{2}\overrightarrow{\partial}_q\right) g(q,p) \tag{A.6}$$

Moyal's equation is necessary but not sufficient to specify the Wigner function W for a system.

An additional functional equation is given by the $\star$-*genvalue* equation for a static W:

$$\begin{aligned} H(q,p)\star W(q,p) &= H\left(q+\frac{i\hbar}{2}\overrightarrow{\partial}_p, p-\frac{i\hbar}{2}\overrightarrow{\partial}_q\right) W(q,p) \\ &= W(q,p)\star H(q,p) = E\,W(q,p) \end{aligned} \tag{A.7}$$

This defines the energy eigenvalue E of the system with the same spectral properties as given in Hilbert space.

The time evolution of a system is given by solving Moyal's equation via the $\star$-*exponential*, a $\star$-unitary evolution operator defined as:

$$\begin{aligned} U_\star &= e_\star^{itH/\hbar} \\ &\equiv 1+\frac{it}{\hbar}H+\left(\frac{it}{\hbar}\right)^2 H\star H+\ldots \end{aligned} \tag{A.8}$$

Giving the time evolution for a function f in phase-space:

$$f(q,p;t) = U_\star^{-1}(q,p;t)\star f(q,p;t)\star U_\star(q,p;t) \tag{A.9}$$

As a conclusion, the *Weyl-quantization* of a c-number phase-space monomial $q^m p^n$ is given through the image in Hilbert space as a symmetrically ordered operator:

$$\hat{F}(\hat{q},\hat{p}) = (2\pi)^{-1/2}\int_{-\infty}^{+\infty} \mathrm{d}\sigma\,\mathrm{d}\tau\,\mathrm{d}q\,\mathrm{d}p\,F(q,p)\,\exp\left(\tfrac{i}{\hbar}\left[\sigma(\hat{q}-q)+\tau(\hat{p}-p)\right]\right) \tag{A.10}$$

For a given operator $\hat{F}(\hat{q},\hat{p})$ (symmetrically ordered) its phase-space kernel F(q,p) is given by the relation:

$$\hat{q}\mapsto q, \quad \hat{p}\mapsto p \tag{A.11}$$

with the $\star$-product as the operator product, resulting in the *Weyl-correspondence*, the general correspondence between Hilbert space operators and phase-space c-number functions:

$$\begin{aligned} F(q,p) &\leftrightarrow \hat{F}(\hat{q},\hat{p}) \\ F(q,p)\star G(q,p) &\leftrightarrow \hat{F}(\hat{q},\hat{p})\,\hat{G}(\hat{q},\hat{p}) \end{aligned} \tag{A.12}$$

A.ii. Quantum Canonical Transformations

In this section canonical transformations from classical mechanics are extended to quantum mechanics by utilizing the WWGM-formalism of phase-space quantum mechanics. Basis for this section is Reference [54].

Afterwards this description is reduced to ordinary exponentials and the gauge transformation needed for the tilted lattice model (Section IV.c.1) is constructed.

Quantum Canonical Transformation in WWGM-Formalism

The canonical transformation of phase-space coordinates (q, p) resulting in new coordinates (Q, P) is given through:

$$\begin{aligned} F(q,p) \star q \star F^{-1}(q,p) &= Q(q,p) \\ F(q,p) \star p \star F^{-1}(q,p) &= P(q,p) \end{aligned} \tag{A.13}$$

$$\{\{Q, P\}\} = i\hbar \tag{A.14}$$

$$F \star F^{-1} = F^{-1} \star F = 1 \tag{A.15}$$

$$\{\{F, q\}\} = i\hbar\, \partial_p F, \qquad \{\{F, p\}\} = -i\hbar\, \partial_q F \tag{A.16}$$

where F is the generating function with the algebraic inverse F^{-1}.

From this follows:

$$\begin{aligned} Q(q,p) &= q - i\hbar\, \partial_p F(q,p) \star F^{-1}(q,p) \\ P(q,p) &= p + i\hbar\, \partial_q F(q,p) \star F^{-1}(q,p) \end{aligned} \tag{A.17}$$

Now, three elementary transformations can be constructed: the *gauge* and *point* transformation and the *interchange* of position an momentum. Others are combinations of these.

gauge:

$$\begin{aligned} e_\star^{\lambda f(q)} \star q \star e_\star^{-\lambda f(q)} &= q \\ e_\star^{\lambda f(q)} \star p \star e_\star^{-\lambda f(q)} &= p + i\hbar\, \lambda \partial_q f \end{aligned} \tag{A.18}$$

point:

$$\begin{aligned} e_\star^{\lambda f(q) \star p} \star q \star e_\star^{-\lambda f(q) \star p} &= A(q) \\ e_\star^{\lambda f(q) \star p} \star p \star e_\star^{-\lambda f(q) \star p} &= (\partial_q A(q))^{-1} \star p \end{aligned} \tag{A.19}$$

interchange: to construct the generating function, take:

$$\begin{aligned} F_{\mathrm{I}}(q,p) \star q &= p \star F_{\mathrm{I}}(q,p) \\ F_{\mathrm{I}}(q,p) \star p &= -q \star F_{\mathrm{I}}(q,p) \end{aligned} \tag{A.20}$$

$$\Rightarrow F_{\mathrm{I}}(q,p) = e^{i/\hbar (q^2+p^2)} \tag{A.21}$$

with the $\star$-exponential as given in Equation A.8 and λ as a purely imaginary number.

Transformations with Ordinary Exponentials

Finding the generating functions can be simplified by employing ordinary exponentials instead of the starred forms.

Starting with a system of partial differential equations:

$$\begin{aligned} e^{\lambda f(q,p)} \star q &= Q(q,p) \star e^{\lambda f(q,p)} \\ e^{\lambda f(q,p)} \star p &= P(q,p) \star e^{\lambda f(q,p)} \end{aligned} \tag{A.22}$$

both the generating function and the coordinates (Q, P) can be found without the need for the inverse of the generator.

Expanding the transformation in Equation A.13 for a general function $u(q,p)$ gives[b]:

$$e_\star^{\lambda f(q,p)} \star u(q,p) \star e_\star^{-\lambda f(q,p)} = \sum_{n,r=0}^{\infty} \binom{n}{r} (-1)^r \frac{\lambda^{n+r}}{(n+r)!} f^n \star u \star f^r \tag{A.23}$$

It holds that $e^{-\lambda f}$ is always the inverse of $e^{\lambda f}$ and therefore the expansion (A.23) is equivalent to the partial differential equations (A.22), giving:

$$e_\star^{\lambda f} = e^{\lambda f}, \qquad (f\star)^n = f^n\star \tag{A.24}$$

With this, quantum canonical transformations can be defined with operators through the Weyl-correspondence (see Equation A.12):

$$\begin{aligned} \hat{F}\,(\hat{q},\hat{p})\,\hat{q}\,\hat{F}^{-1}(\hat{q},\hat{p}) &= \hat{Q}\,(\hat{q},\hat{p}) \\ \hat{F}\,(\hat{q},\hat{p})\,\hat{p}\,\hat{F}^{-1}(\hat{q},\hat{p}) &= \hat{P}\,(\hat{q},\hat{p}) \end{aligned} \tag{A.25}$$

$$\left[\hat{Q},\hat{P}\right] = i\hbar \tag{A.26}$$

The generating function is given by exponentials:

$$e^{\lambda \hat{f}}\,\hat{u}(\hat{q},\hat{p})e^{-\lambda \hat{f}} = \hat{u} + \lambda\left[\hat{f},\hat{u}\right] + \frac{\lambda^2}{2!}\left[\hat{f},\left[\hat{f},\hat{u}\right]\right] + \dots \tag{A.27}$$

The general forms of the elementary transformations read:

gauge:

$$\begin{aligned} e^{\lambda f(\hat{q})}\,\hat{q}\,e^{-\lambda f(\hat{q})} &= \hat{q} \\ e^{\lambda f(\hat{q})}\,\hat{p}\,e^{-\lambda f(\hat{q})} &= \hat{p} + i\hbar\,\partial_q f \end{aligned} \tag{A.28}$$

point:

$$\begin{aligned} e^{\lambda f(\hat{q})}\,\hat{q}\,e^{-\lambda f(\hat{q})} &= A(\hat{q}) \\ e^{\lambda f(\hat{q})}\,\hat{p}\,e^{-\lambda f(\hat{q})} &= (\partial_q A)^{-1}\,\hat{p} \end{aligned} \tag{A.29}$$

$$A(\hat{q}) = e^{-i\hbar\lambda f(\hat{q})\,\partial_q}\,\hat{q} \tag{A.30}$$

[b] This is always possible if $f(q,p) = f(q)$ or $f(p)$.

interchange:

$$\begin{aligned} \hat{I}\,\hat{q}\,\hat{I}^{-1} &= \hat{p} \\ \hat{I}\,\hat{p}\,\hat{I}^{-1} &= -\hat{q} \end{aligned} \tag{A.31}$$

$$\hat{I}^{\pm 1} f(\hat{q}) = (2\pi)^{-1/2} \int_{-\infty}^{+\infty} \mathrm{d}q'\, f(\hat{q}')e^{\pm\frac{i}{\hbar}qq'} \tag{A.32}$$

The ordinary exponentials can now be used to find the recipe for the gauge transformation used in Section IV.c.1. The other transformations are left out for brevity[c].

The gauge transformation is now given by:

$$\hat{Q} = \hat{q}, \quad \hat{P} = \hat{p} + u(\hat{q}) \tag{A.33}$$

with the generating function:

$$F_{\mathrm{G}} = e^{-\frac{i}{\hbar}\int \mathrm{d}q\, u(\hat{q})} \tag{A.34}$$

as a result of the solution to:

$$\begin{aligned} -\partial_q F_{\mathrm{G}} &= \partial_p F_{\mathrm{G}} \\ i\hbar\,\partial_q F_{\mathrm{G}} &= u(\hat{q} + i\tfrac{\hbar}{2}\,\partial_p)\, F_{\mathrm{G}} \end{aligned} \tag{A.35}$$

Implications for Functions

In addition, the effect of canonical transformations on functions in q and p and energy eigenvalues E should be considered in phase-space.

Functions change under a linear canonical transformation as:

$$F(q,p) \star u(q,p) \star F^{-1}(q,p) = u\left(FqF^{-1}, FpF^{-1}\right) \tag{A.36}$$

This holds for arbitrary phase-space functions u.

Especially for any gauge transformation it can be shown that:

$$p^2 \mapsto (p + i\hbar\lambda\,\partial_q f)^2 \quad \text{and} \quad p^{-1} \mapsto (p + i\hbar\lambda\,\partial_q f)^{-1} \tag{A.37}$$

The Hamiltonian is transformed accordingly:

$$\hat{H}(\hat{q},\hat{p}) \mapsto \hat{K}(\hat{Q},\hat{P}) \tag{A.38}$$

The energy eigenvalue can be considered by the $\star$-genvalue equation (A.7):
$H(q,p) \star W(q,p) = E\,W(q,p)$

$$\Rightarrow\ H'(q,p) \star W'(q,p) = E\,W'(q,p) \tag{A.39}$$

$$\text{where:} \quad \begin{aligned} H'(q,p) &= F(q,p) \star H(q,p) \star F^{-1}(q,p) \\ W'(q,p) &= F(q,p) \star W(q,p) \star F^{-1}(q,p) \end{aligned} \tag{A.40}$$

The transformation leaves the eigenenergies unchanged.

[c] for more, see [54]

Time-Dependent Transformations

So far no time-dependency has been regarded.

In order to do so, the time-component is effectively treated as the zeroth component in the $(1, n)$-dimensional *Minkowski* space. As such there is an momentum operator in time $\hat{p}_0$ or $\hat{p}_t = i\,\partial_t$, in addition to $\hat{p} = -i\,\partial_q$, that transforms as a momentum operator[d].

For the example of a gauge transformation this gives (compare A.28):

$$\hat{p}_t \mapsto \hat{P}_t = \hat{p}_t - i\hbar\lambda\,\partial_t f \tag{A.41}$$

For time-dependency not just the system's Hamiltonian is regarded, but the time-dependent Schrödinger equation.

$$\hat{H}\,\Psi = i\hbar\,\partial_t\Psi \quad \Leftrightarrow \quad \hat{\mathscr{H}}\,\Psi = 0 \tag{A.42}$$

$$\Rightarrow \quad \hat{\mathscr{H}} = \hat{H} - \hat{p}_t \tag{A.43}$$

where $\hat{\mathscr{H}}$ can be considered the *Schrödinger-operator*[55].

For explicitly time-dependent systems the transformation takes the form:

$$\hat{\mathscr{H}}\,(\hat{q}, \hat{p}; t) \mapsto \hat{\mathscr{K}}\,(\hat{Q}, \hat{P}; t) = \hat{K} - \hat{P}_t \tag{A.44}$$

and for the gauge transformation:

$$\hat{\mathscr{K}}\,(\hat{Q}, \hat{P}; t) = \hat{K} - \hat{p}_t + i\hbar\lambda\,\partial_t f \tag{A.45}$$

A.iii. Classical Mechanics in Hilbert Space

This section gives the theoretical basis for the Phase-Space Evolution scheme. While it does give Wigner functions as quantum mechanical phase-space distributions, it does so not by using Moyal's equation within the WWGM-formalism, but rather by employing a *Hilbert phase-space formalism*[35,56] that is closely related to the *Koopman-von Neumann formulation*[57] of classical mechanics.

Therefore a short introduction to Koopman-von Neumann mechanics will be given first, followed by the derivation of equation of motion producing the Wigner function within the Hilbert phase-space formalism.

[d] with regard to the metric signature of a Minkowski space

Mechanics in Operator Formulation

Classical and quantum mechanics are formulated with different tools: Where the formulation of *classical* mechanics uses phase-space and the Poisson-bracket to describe the dynamics of a system, *quantum* mechanics is defined in terms of states and operators on a Hilbert space.

To unify these two formulations, two approaches could be taken:

1) A reformulation of quantum mechanics in a "classical" language with phase-space distributions
→ *WWGM-formalism*, as described in a previous section

2) An operator method for classical mechanics on a Hilbert space
→ *Koopman-von Neumann classical mechanics*

The second approach was devised by Bernard Koopman[37] in 1931 and developed further by John von Neumann[38,39] in 1932.

It introduces a Hilbert space of square integrable complex-valued functions $\psi(q,p)$, with probability density $|\psi|^2 = \rho(q,p)$.

The following *postulates*[56] are given:

i) The *states* of a system are represented by normalized vectors $|\psi\rangle$ of a complex Hilbert space $\mathfrak{h}$.

ii) The *expectation value* of a measurable $\hat{A}$ is given by $\bar{A}(t) = \langle\psi(t)|\,\hat{A}\,|\psi(t)\rangle$ at time t.

iii) The *probability* for the measurement of $\hat{A}$ at time t to yield the result A is given by $|\langle A|\psi(t)\rangle|^2$, where $\hat{A}\,|A\rangle = A\,|A\rangle$.

iv) The state space of a composite system is the tensor product of the state spaces of the subsystems.

With these the state spaces, observables and equations of motion can be deduced by observable data.

The postulates are known from quantum mechanics, but in this formalism $|\psi\rangle$ encompasses classical and quantum behavior as a general state.

Equation of Motion for Wigner Functions

In the following the variables x and $\mathbf{x}$ will denote different entities, where x is a c-number coordinate in phase-space and $\mathbf{x}$ is a classical operator.

Starting point to derive an equation that determines the time evolution of the Wigner function is the unitary evolution for the density operator $\hat{\rho}$:

$$i\hbar\,\partial_t\hat{\rho} = \left[\hat{H}\,(\hat{\mathbf{q}},\hat{\mathbf{p}}),\,\hat{\rho}\right], \quad \left[\hat{\mathbf{q}},\hat{\mathbf{p}}\right] = i\hbar \tag{A.46}$$

or in the position representation for $\rho(\mathbf{q}, \mathbf{q}')$:

$$i\hbar\,\partial_t\hat{\rho} = \left[H(\mathbf{q}, -i\hbar\partial_{\mathbf{q}}), -H(\mathbf{q}', -i\hbar\partial_{\mathbf{q}'})\right]\hat{\rho} \tag{A.47}$$

With a change of variables:

$$\mathbf{q} = q - \tfrac{\hbar}{2}\theta, \quad \mathbf{q}' = q + \tfrac{\hbar}{2}\theta \tag{A.48}$$

this yields the function:

$$B(q,\theta) = \langle q - \tfrac{\hbar}{2}\theta|\,\rho\,|q + \tfrac{\hbar}{2}\theta\rangle \tag{A.49}$$

as a solution to the equation of motion[e]:

$$i\hbar\,\partial_t B(q,\theta) = \left[H\Big(q - \tfrac{\hbar}{2}\theta, i\left(\partial_\theta - \tfrac{\hbar}{2}\partial_q\right)\Big) - H\Big(q + \tfrac{\hbar}{2}\theta, i\left(\partial_\theta + \tfrac{\hbar}{2}\partial_q\right)\Big)\right] B(q,\theta) \tag{A.50}$$

Defining p as the conjugate to θ gives $W(q,p)$ as the Fourier transform of $B(q,\theta)$:

$$B(q,\theta) = \int \mathrm{d}p\, W(q,p)e^{-ip\theta}, \quad W(q,p) = \frac{1}{2\pi}\int \mathrm{d}\theta\, B(q,\theta)e^{ip\theta} \tag{A.51}$$

In general $B \in \mathbb{C}$ holds, thus $W \in \mathbb{R}$. Additionally, W is normalizable to 1.
In phase-space the equation of motion now reads:

$$i\hbar\,\partial_t W(q,p) = \left[H\left(q + i\tfrac{\hbar}{2}\partial_p, p - i\tfrac{\hbar}{2}\partial_q\right) - H\left(q - i\tfrac{\hbar}{2}\partial_p, p + i\tfrac{\hbar}{2}\partial_q\right)\right] W(q,p) \tag{A.52}$$

This can be rewritten with $\star$-products by utilizing *Bopp-shifts* (see Equation A.6):

$$i\hbar\,\partial_t W(q,p) = H(q,p)\star W(q,p) - W(q,p)\star H(q,p) \tag{A.53}$$

which is the *Moyal equation*.

Representations of the Hilbert Phase-Space Formulation

As mentioned in the introduction, the commuting operators $\hat{x}$ and $\hat{p}$ form the the basis of the Koopman-von Neumann representation of classical mechanics.

The additional operators $\hat{\lambda}$ and $\hat{\theta}$ are the *Bopp-operators*[40,53,58], related to the Bopp-shifts. This leads to the canonically conjugate position and momentum:

$$\hat{\mathbf{q}} = \hat{q} - \tfrac{\hbar}{2}\hat{\theta}, \quad \hat{\mathbf{p}} = \hat{p} + \tfrac{\hbar}{2}\hat{\lambda} \tag{A.54}$$

where $\left[\hat{\mathbf{q}}, \hat{\mathbf{p}}\right] = i\hbar$.

The four operators $\hat{q}$, $\hat{p}$, $\hat{\theta}$ and $\hat{\lambda}$ define a Hilbert space, thus leading to the terminology *Hilbert phase-space formalism*[35].

[e] called the double configuration space representation

The mirrored operators are defined as:

$$\begin{gathered}\hat{\mathbf{q}}' = \hat{q} + \tfrac{\hbar}{2}\hat{\theta}, \quad \hat{\mathbf{p}}' = \hat{p} - \tfrac{\hbar}{2}\hat{\lambda}, \\ \left[\hat{\mathbf{q}}, \hat{\mathbf{q}}'\right] = \left[\hat{\mathbf{p}}, \hat{\mathbf{p}}'\right] = \left[\hat{\mathbf{q}}, \hat{\mathbf{p}}'\right] = \left[\hat{\mathbf{p}}, \hat{\mathbf{q}}'\right] = 0\end{gathered} \tag{A.55}$$

A common orthonormal eigenbasis exists for $|q\,\theta\rangle$ (or $|\lambda\, p\rangle$), where $\langle q\,\theta|\lambda\, p\rangle = \frac{1}{2\pi} e^{i(p\theta - q\lambda)}$

Now the evolution of the quantum density operator in position space (Equation A.47) is given as:

$$i\hbar\, \mathrm{D}_t\, |\rho\rangle = \left[H\left(\hat{\bar{q}}, \hat{\bar{p}}\right) - H\left(\hat{\bar{q}}', \hat{\bar{p}}'\right)\right] |\rho\rangle \tag{A.56}$$

with $|\rho\rangle$ in the Hilbert phase-space.

$\hat{q}$, $\hat{p}$, $\hat{\theta}$, $\hat{\lambda}$ can be realized as differential operators, leading to different representations:

$$\hat{q} = q, \quad \hat{p} = p, \quad \hat{\lambda} = -i\partial_q, \quad \hat{\theta} = -i\partial_p \qquad q\text{-}p \text{ representation}$$

or:

$$\hat{q} = q, \quad \hat{p} = i\partial_\theta, \quad \hat{\lambda} = -i\partial_q, \quad \hat{\theta} = \theta \qquad q\text{-}\theta \text{ representation}$$

Considering Hamiltonians of the form $\hat{H} = \frac{1}{2m}\hat{\bar{p}}^2 + V(\hat{\bar{q}})$ the abstract formulation of the equation of motion can be written as:

$$i\hbar\, \mathrm{D}_t\, |\rho\rangle = \left[\frac{\hbar}{m}\hat{p}\hat{\lambda} + V\left(\hat{q} - \tfrac{\hbar}{2}\hat{\theta}\right) - V\left(\hat{q} + \tfrac{\hbar}{2}\hat{\theta}\right)\right] |\rho\rangle \tag{A.57}$$

or in the q-θ representation:

$$i\hbar\, \partial_t\, |\rho\rangle_{q\theta} = \left[\frac{\hbar}{m}\partial_q\partial_\theta + V\left(q - \tfrac{\hbar}{2}\theta\right) - V\left(q + \tfrac{\hbar}{2}\theta\right)\right] |\rho\rangle_{q\theta} \tag{A.58}$$

where: $|\rho\rangle_{q\theta} = \langle q\theta|p\rangle$

This is the same differential equation as Equation A.50, thereby:

$$B(q,\theta) = \frac{1}{\sqrt{\hbar}}\, |\rho\rangle_{q\theta} \tag{A.59}$$

Alternatively it can be written as:

$$i\hbar\, \partial_t\, |\rho\rangle_{qp} = \left[-i\frac{\hbar}{m}p\partial_q + V^+ - V^-\right] |\rho\rangle_{qp} \tag{A.60}$$

where: $V^\pm = V\left(q \pm \frac{i\hbar}{2}\partial_p\right)$, giving the Wigner functions with:

$$W(q,p) = \frac{1}{\sqrt{2\pi\hbar}}\, |\rho\rangle_{qp} \tag{A.61}$$

on the usual phase-space.

Thus, simply by choosing an appropriate representation, an integro-differential equation (Moyal equation in q-p) can be changed to a second order partial differential equation (equation of motion (A.57) in q-θ) with the same computational complexity as a two-dimensional Schrödinger equation.

Altogether there are four representations:

q-p: $W(q,p)$

q-θ: $B(q,p)$

λ-θ: $A(\lambda,\theta) = \int \mathrm{d}q\, B(q,\theta) e^{-i\lambda q}$

λ-q: $Z(\lambda,p) = \frac{1}{2\pi} \int \mathrm{d}q\, \mathrm{d}\theta\, B(q,\theta) e^{i(p\theta-\lambda q)}$

$A(\lambda,\theta)$ is the ambiguity function in signal processing and $Z(\lambda,p)$ can be called the double momentum space representation.

The different representations with respective functions are related by Fourier transforms. An overview of the functions and representations is depicted in Figure B.1.

This general formalism can be used for classical dynamics (*Liouville equation*), open systems (*Lindblad form master equation, Fokker-Planck equation*) and quantum dynamics in phase-space (*Moyal equation*).

Numerical solutions can be obtained with a split-operator method. Such a scheme is derived in Appendix B.ii.

B. Numerics

B.i. Crank-Nicolson Method

For numerically solving the Schrödinger equation, the Crank-Nicolson[23] method was implemented. It was initially proposed for solving the heat equation, but is now an established method for the Schrödinger equation as well.

An introduction is found in many textbooks on numerical methods, among them [24]. The overview in [59] proved useful as well.

Derivation of the Scheme

The Hamiltonian[a] for quantum problems is:

$$H(x,t) = -\frac{1}{2}\partial_x^2 + V(x,t) \tag{B.1}$$

giving the Schrödinger equation:

$$H\,\Psi = i\partial_t\,\Psi \tag{B.2}$$

For numerical computations the problem needs to be discretized:

- grid:

$$\begin{aligned} x_j &= j\,h, \quad 1 \leqslant j \leqslant J \\ t_n &= n\,k, \quad 1 \leqslant n \leqslant N \end{aligned}$$

  where $j, n \in \mathbb{N}$ number the grid and h, k are the step sizes;
- wave functions:

$$\Psi(x,t) \to \psi_j^n$$

- central differences instead of differentials:

$$\partial_x^2\Psi \to \frac{1}{h^2}\delta_0^{(2)}\psi_j = \frac{1}{h^2}\left(\psi_{j-1} + 2\psi_j + \psi_{j+1}\right)$$

$$\partial_t\Psi \to \frac{1}{k}\delta_+^{(1)}\psi^n = \frac{1}{k}\left(\psi^{n+1}\psi^n\right)$$

- Hamiltonian:

$$H(x,t) \to \eta_j^n = -1/2\delta_0^{(2)} + v_j^n$$

[a] Technically, H, x and p are operators but will not be specially denoted as such for brevity.

- Schrödinger equation:

$$\frac{i}{k}\delta_+^{(1)}\psi^n = \eta^n\psi^n \quad \forall j$$

The Schrödinger equation will be taken at the intermediate time-step[b] $n + 1/2$ by taking the average of the *rhs.*:

$$\frac{i}{k}\left(\psi^{n+1} + \psi^n\right) = \frac{1}{2}\left(\eta\,\psi^{n+1} + \eta\,\psi^n\right) \tag{B.3}$$

$$\Rightarrow \left(1 + \frac{ik}{2}\eta\right)\psi^{n+1} = \left(1 - \frac{ik}{2}\eta\right)\psi^n \tag{B.4}$$

This is the general ansatz for *Crank-Nicolson* schemes. The evolution operator is unitary, making this method numerically stable.

Matrix Algorithm

The next step is to take this ansatz and construct an implementable algorithm from it.

Define: $r = 4\frac{h^2}{k}$ and $w = 2h^2$ and take the potential at $n + 1/2$: $v^{n+1/2} = v^n + 1/2\left(v^{n+1} - v^n\right)$

Putting this in Equation B.3 or B.4 results in:

$$\begin{aligned} &-ir\left(\psi_j^{n+1} - \psi_j^n\right) \\ &\quad = \psi_{j-1}^{n+1} - 2\psi_j^{n+1} + \psi_{j+1}^{n+1} + \psi_{j-1}^n - 2\psi_j^n + \psi_{j+1}^n - w\,v_j^{n+1/2}\left(\psi_j^{n+1} - \psi_j^n\right) \end{aligned} \tag{B.5}$$

Reorder terms with respect to time-steps:

$$-\psi_{j-1}^{n+1} + (2 - ir + w)\,\psi_j^{n+1} - \psi_{j+1}^{n+1} = \psi_{j-1}^n - (2 + ir + w)\,\psi_j^n + \psi_{j+1}^n \tag{B.6}$$

This can be written as a matrix equation, where $\underline{\underline{M}}$ denotes a matrix and $\underline{v}$ denotes a vector:

$$\underline{\underline{L}}^{n+1/2}\,\underline{\psi}^{n+1} = \underline{\underline{R}}^{n+1/2}\,\underline{\psi}^n, \tag{B.7}$$

where $\underline{\underline{L}} = \begin{pmatrix} a_1 & -1 & & 0 \\ -1 & a_2 & -1 & \\ & \ddots & \ddots & \ddots \\ 0 & & -1 & a_{J-1} & -1 \\ & & & -1 & a_J \end{pmatrix}$, $a_j^{n+1/2} = 2 - ir + v_j^{n+1/2}$ and $\underline{\underline{R}} = -\underline{\underline{L}}^*$

By taking v at the intermediate time-step it is used as an approximation[c] both for n and $n+1$. With this one of the coefficient matrices can be expressed through the other. This improves the computation speed significantly.

The system B.7 must be solved for all $n \geqslant 2$, but since $\underline{\underline{R}}$ and $\underline{\underline{L}}$ are *tri-diagonal* matrices this can be done numerically with good efficiency.

[b] The time-index for η is left out for the moment, but will effectively be taken at an intermediate time-step $n + 1/2$, effectively by averaging the potential appropriately.

[c] This is appropriate as long as k is small or V varies slowly in time.

B.ii. Split Operator Method for the Phase-Space Evolution Scheme

In Appendix A.iii the general method for solving the Moyal equation efficiently was derived.

Based on that, the focus here is on a numerical scheme to compute the time evolution of Wigner functions, which will be referred to as the *Phase-Space Evolution* scheme.

The equation of motion (see Equation A.60) for the Wigner function on the usual phase-space is:

$$i\hbar\,\partial_t W(q,p) = \left[-i\frac{\hbar}{M}p\partial_q + V^+ - V^-\right] W(q,p) \tag{B.8}$$

where: $V^{\pm} = V\left(q \pm \frac{i\hbar}{2}\partial_p\right)$.

With a transformation to a different representation the differential operators are replaced by variables. In the q-θ representation for the potential term: $-i\partial_p$ is transformed to θ, and in the λ-p representation for the kinetic term: $-i\partial_p$ is likewise transformed to λ.

These changes in the representation are indicated in Figure B.1 by dashed arrows. The functions are given in their natural representation, with Fourier transforms between

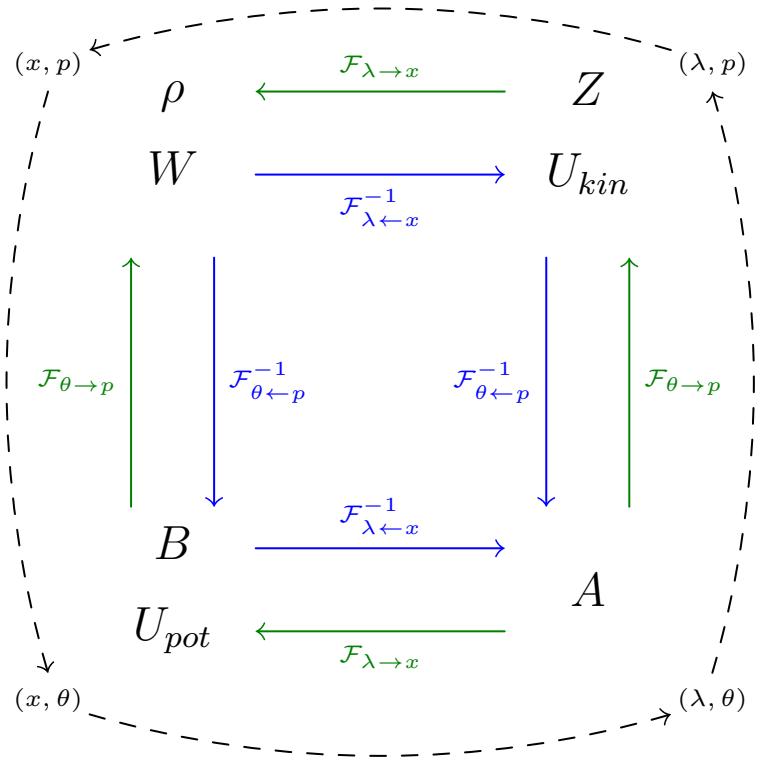

Figure B.1.: Schematic overview of the different representations and their relations through Fourier transforms in the Phase-Space Evolution scheme.

them.

The unitary time-evolution operator for an increment dt is given by:

$$U_{dt} = \exp\left(-i\,dt\left[\frac{\hat{p}\hat{\lambda}}{M} + \frac{V^- - V^+}{\hbar}\right]\right) \tag{B.9}$$

Using the Trotter product formula[60] this is approximated by:

$$U_{dt} = \exp\left(-i\frac{dt}{M}\hat{p}\hat{\lambda}\right)\exp\left(-i\frac{dt}{\hbar}\left(V^- - V^+\right)\right) + \mathcal{O}(dt^2) \tag{B.10}$$

This is the split-operator method and results in the first order scheme:

$$W(t+dt) = \mathcal{F}_{\lambda\to q}\,\exp\left(-i\frac{dt}{M}p\lambda\right)\mathcal{F}_{\theta\to p}\,\mathcal{F}_{q\to\lambda}\,\exp\left(-i\frac{dt}{\hbar}\left(V^- - V^+\right)\right)\mathcal{F}_{p\to\theta}\,W(t) \tag{B.11}$$

where: $\mathcal{F}_{a\to b}$ describes a Fourier transform (or its inverse) between a and b, acting on the terms to the right.

Numerically, these Fourier transforms can be implemented using *fast Fourier transforms* (FFT). An algorithm is presented in [36].

B.iii. Notes on Implementations

All numerical results were computed with MATLAB, version `9.3.0.713579` (R2017b).

For the Wigner-Ville transformation the command `tfrwv` from the *Time-Frequency Toolbox*[33] for MATLAB was used.

Characteristic values and special functions of the Mathieu equation were obtained from the *Mathieu Functions Toolbox v.1.0*[27].

The Crank-Nicolson method required large domains in q because of undefined – and thereby reflecting – boundary conditions. This would have been avoided with *transparent boundary conditions*. A method is described in Reference [61], but its implementation was not fully functional in time.

C. Additional Derivations

C.i. Eigenfunctions and -values of the Quantum Pendulum

The eigenfunctions and -values of the quantum pendulum, used in the simulations of Section II.b.2, will be derived.

Starting point is the Hamiltonian[a] of a pendulum $H = \frac{1}{2}p^2 - \gamma\cos(\theta)$, leading to the time-independent Schrödinger equation[25] $H\psi = E\psi$:

$$\left(-\frac{1}{2}\partial_\theta^2 - \gamma\,\cos(\theta) - E\right)\psi(\theta) = 0, \tag{C.1}$$

where the eigenfunctions ψ are 2π-periodic in θ: $\psi(\theta) = \psi(\theta + 2\pi)$.

This can be rewritten as the *Mathieu equation*[26]:

$$\frac{\mathrm{d}^2}{\mathrm{d}\nu^2}\psi(\nu) + (a - 2q\cos(2\nu))\,\psi(\nu) = 0, \tag{C.2}$$

by defining: $\theta \equiv 2\nu$, $q \equiv -\gamma$, $a \equiv 2E$.

The solutions of this differential equation are special functions: the Mathieu functions of even order[b]:

$$\begin{array}{ll} \text{Mathieu cosine:} & \mathrm{ce}_{2m}(\nu) \\ \text{Mathieu sine:} & \mathrm{se}_{2m}(\nu) \end{array} \quad \text{with } m = 0, 1, 2, \ldots \tag{C.3}$$

These functions do not a have simple analytic form, but they can be represented via a Fourier series. They were implemented using [27].

The Mathieu functions are usually defined for positive q, so a change of variable to $\frac{\pi}{2} - \nu$ is needed, resulting in the functions:

$$\begin{aligned} \mathrm{ce}_0(\nu, -q) &= \mathrm{ce}_0(\tfrac{\pi}{2} - \nu, q) \\ \mathrm{ce}_{2m}(\nu, -q) &= (-1)^m \mathrm{ce}_{2m}(\tfrac{\pi}{2} - \nu, q) \\ \mathrm{se}_{2m}(\nu, -q) &= (-1)^{m+1} \mathrm{se}_{2m}(\tfrac{\pi}{2} - \nu, q) \end{aligned} \tag{C.4}$$

[a] the general and unshifted variant of Equation II.23

[b] More solutions exist, but are disregarded because of the required periodicity.

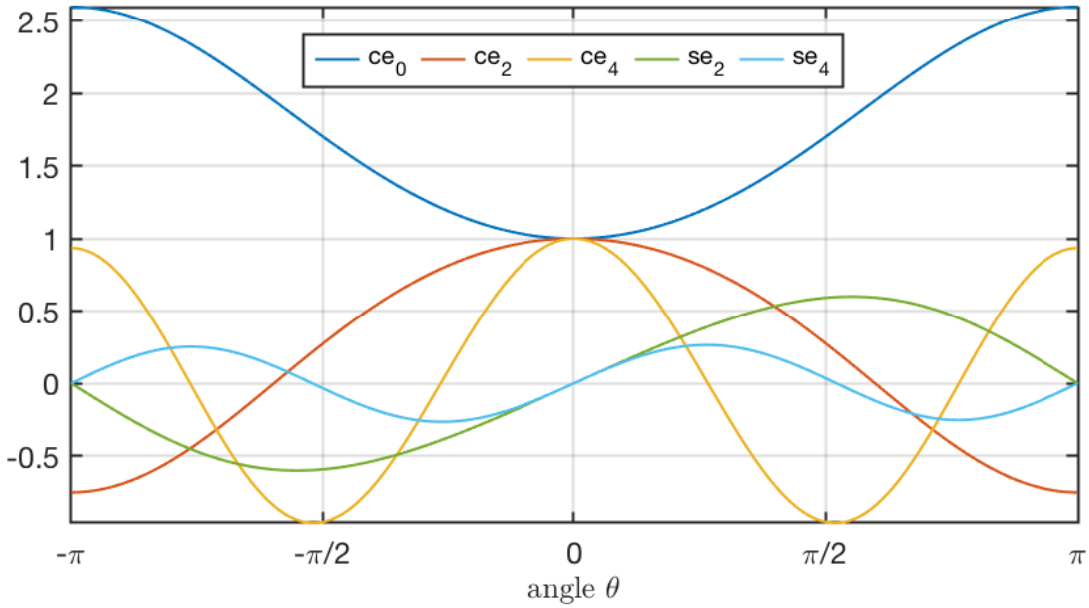

Figure C.1.: Mathieu functions of even order for $n = 2m \leqslant 4$.

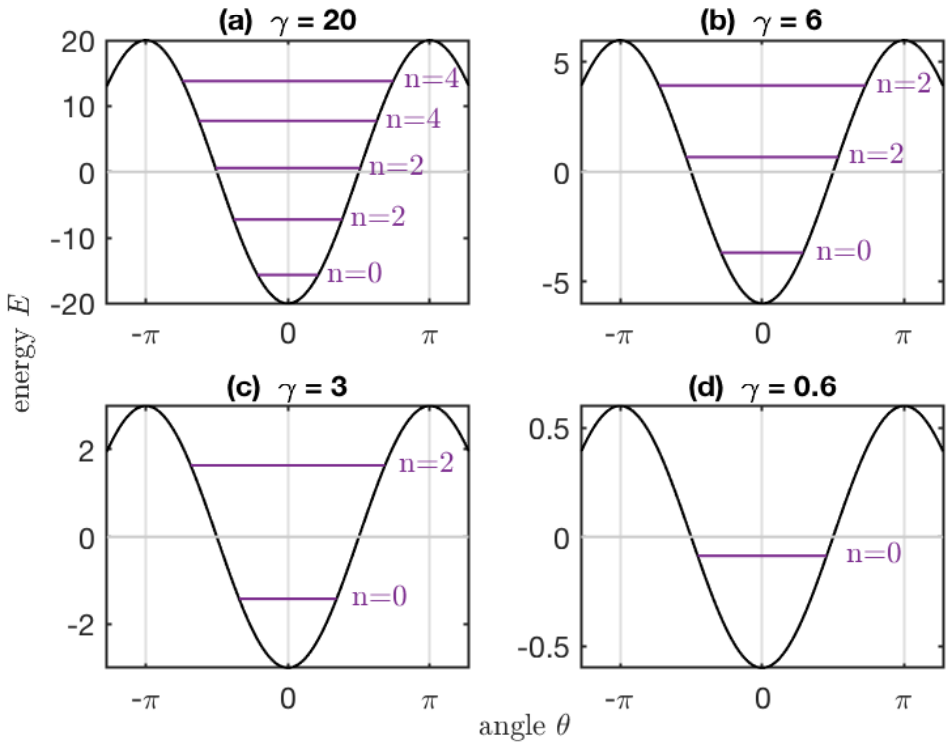

Figure C.2.: Characteristic values of the Mathieu equation corresponding to energy eigenvalues of bound states in the quantum pendulum. Values with the same number n correspond to even/odd pairs of eigenfunctions.

which are commonly normalized to π on the interval $(0, 2\pi)$.
The wave functions to the Schrödinger equation (C.1), normalized to 1, are then:

$$\begin{aligned}
\psi_0^{(e)}(\theta, -q) &= \tfrac{1}{\sqrt{2\pi}}\mathrm{ce}_0(\tfrac{\pi-\theta}{2}, q) \\
\psi_{2m}^{(e)}(\theta, -q) &= \tfrac{(-1)^m}{\sqrt{\pi}}\mathrm{ce}_{2m}(\tfrac{\pi-\theta}{2}, q) \qquad \text{(even)} \\
\psi_{2m}^{(o)}(\theta, -q) &= \tfrac{(-1)^{m+1}}{\sqrt{\pi}}\mathrm{se}_{2m}(\tfrac{\pi-\theta}{2}, q) \qquad \text{(odd)} \\
&\qquad\qquad \text{with } m = 1, 2, 3, \ldots
\end{aligned} \tag{C.5}$$

These are linearly independent and orthogonal.
The Mathieu cosine and sine for orders $n = 2m \leqslant 4$ are shown in Figure C.1. The cosine ce_0 of lowest order $n = 0$ corresponds to a delocalized wave function and is therefore disregarded for the decay simulations.

The characteristic values a lead to the eigenenergies E_m via:

$$E_m = \frac{1}{2}a. \tag{C.6}$$

Figure C.2 shows characteristic values corresponding to bound states in a quantum pendulum potential for four different values of γ. For very large γ the eigenvalues would effectively degenerate since pairs of even and odd values show little difference in their energies. Also at large γ the energies are approximately equidistant, but for lower values the difference increases with decreasing n. For very low γ there is only one possible eigenvalue with $n = 0$ left, which approaches zero. Thus there is always one bound state possible with the eigenfunction corresponding to the delocalized ce_0.

C.ii. Analytical Expression for the Decay Width

The decay width for a quasi-stationary state is given by[c]:

$$\begin{aligned}
\Gamma &= \frac{N}{4}\exp\left(-2\int_{r_1}^{r_2}\mathrm{d}r\,|p(r)|\right), \\
N^{-1} &= \int_{r_0}^{r_1}\tfrac{1}{p(r)}\cos^2\left(\int_{r_0}^{r}p(r')\,\mathrm{d}r' - \tfrac{\pi}{4}\right)\mathrm{d}r,
\end{aligned} \tag{C.7}$$

where $m \equiv 1$, $\hbar \equiv 1$ has been used.
The rectangular barrier has a ($\Rightarrow E_\mathrm{R}$), w, $b = a + w$, V_0 as system parameters. The momentum is given by:

$$p(r) = \begin{cases} \alpha = \sqrt{2(V_0 - E)}, & r \in B, \\ \kappa = \sqrt{2E}, & r \notin B, \end{cases} \tag{C.8}$$

[c] see Equation II.14

with the barrier $B = [a, b]$.

The integral $\int_{r_1}^{r_2} \mathrm{d}r\ |p(r)|$ gives the *Gamow factor*: $G = \alpha w$

$$\Rightarrow \Gamma = \frac{N}{4} \exp(-2\alpha w)$$

normalization constant N:

$$\int_a^r \mathrm{d}r'\, p(r') = k(r-a) \quad \Leftarrow p(r)|_{r \notin B} = k$$

$$\Rightarrow N^{-1} = \int_0^a \mathrm{d}r\, \tfrac{1}{p(r)} \cos^2\left(k(r-a) - \frac{\pi}{4}\right)$$

$$= \frac{1}{k} \int_0^a \mathrm{d}r\, \cos^2\left(k(r-a) - \frac{\pi}{4}\right)$$

Define: $k(r-a) - \frac{\pi}{4} = kr - \underbrace{ka - \frac{\pi}{4}}_{=:\delta} = kr - \delta$

$$\Rightarrow \cos^2(kr - \delta)$$

$$\Rightarrow N^{-1} = \frac{1}{k} \int_0^a \mathrm{d}r\, \cos^2(kr - \delta)$$

Substitute: $r \mapsto \rho = kr - \delta \Rightarrow \mathrm{d}r = \frac{\mathrm{d}\rho}{k}$

$$\Rightarrow \int_{\rho(a)}^{\rho(b)} \frac{1}{k}\, \mathrm{d}\rho\, \cos^2(\rho)$$

$$= \frac{1}{2k} \Big[\rho + \sin(\rho)\, \cos(\rho)\Big]_{-\delta}^{-\frac{\pi}{4}}$$

$$= \frac{a}{2} + \frac{1}{2k} \left(\sin(-\tfrac{\pi}{4})\, \cos(-\tfrac{\pi}{4}) - \sin(-\delta)\, \cos(-\delta)\right)$$

$$= \frac{a}{2} + \frac{1}{2k} \left(-\sin(\tfrac{\pi}{4})\, \cos(\tfrac{\pi}{4}) + \sin(ka + \tfrac{\pi}{4})\, \cos(ka - \tfrac{\pi}{4})\right)$$

$$= \frac{a}{2} + \frac{1}{2k} \left(\sin(ka)\, \cos(ka + \tfrac{\pi}{2})\right)$$

$$= \frac{a}{2} + \frac{1}{2k} \sin^2(ka)$$

The result is:

$$N^{-1} = \frac{1}{2k} \left(ka - \sin^2(ka)\right) \tag{C.9}$$

$$\Rightarrow \Gamma = 2k\, \frac{\exp(-2\alpha w)}{ka - \sin^2(ka)}. \tag{C.10}$$

With $k = \sqrt{2E}$ follows $\Gamma \sim \sqrt{E}$.

C.iii. Quantum Daemon Hamiltonian for the EQPM

The derivation of the quantum engine Hamiltonian that was used for the EQPM starts with the Hamiltonian in Equation I.5:

$$\hat{H} = \frac{1}{2M}\hat{p}^2 + Mg\hat{z} + \Omega_+\hat{a}_+^\dagger\hat{a}_+ + \Omega_-\hat{a}_-^\dagger\hat{a}_- + \frac{\gamma}{2}\left(\hat{a}_+\hat{a}_-^\dagger e^{ik\hat{z}} + \hat{a}_-\hat{a}_+^\dagger e^{-ik\hat{z}}\right), \quad \text{(C.11)}$$

with the angular momentum operators $\hat{L}$ written out in terms of $\hat{a}_\pm$ and $\hat{a}_\pm^\dagger$.

Define:

$$\hat{J} = \hat{p} + Mgt - k\hat{a}_-^\dagger\hat{a}_-, \quad \text{(C.12)}$$

where $[\hat{H}, \hat{J}] = iMg$, so that $\frac{\mathrm{d}}{\mathrm{d}t}\hat{J} = 0$, and $[\hat{J}, \hat{z}] = i$.

Furthermore the annihilation operator

$$\hat{b}_- = \hat{a}_-^\dagger e^{ik\hat{z}} \quad \text{(C.13)}$$

is defined, where $[\hat{J}, \hat{b}_-] = 0$. The number operators are: $\hat{n}_- = \hat{a}_-^\dagger\hat{a}_- = \hat{b}_-^\dagger\hat{b}_- \equiv \hat{m}_-$ and the total number operator $\hat{N} = \hat{n}_+ + \hat{n}_- = \hat{n}_+ + \hat{m}_-$ is conserved.

New angular momentum operators can now be defined with the operators $\hat{a}_+$ and $\hat{b}_-$:

$$\hat{S}_x = \frac{1}{2}\left(\hat{a}_+^\dagger\hat{b}_- + \hat{a}_+\hat{b}_-^\dagger\right), \quad \text{(C.14)}$$

$$\hat{S}_y = \frac{1}{2i}\left(\hat{a}_+^\dagger\hat{b}_- - \hat{a}_+\hat{b}_-^\dagger\right), \quad \text{(C.15)}$$

$$\hat{S}_z = \frac{1}{2}\left(\hat{n}_+ - \hat{m}_-\right), \quad \text{(C.16)}$$

and $\hat{S}_\mp = \hat{S}_x \pm i\hat{S}_y$.

Altogether the Hamiltonian can be written as

$$\hat{H} = \frac{1}{2M}\left(\hat{J} + \frac{1}{2}k\hat{N} - k\hat{S}_z - Mgt\right)^2 + \Omega_+\left(\frac{1}{2}\hat{N} + \hat{S}_z\right) + \Omega_-\left(\frac{1}{2}\hat{N} - \hat{S}_z\right) + \frac{1}{2}\gamma\left(\hat{S}_- + \hat{S}_-^\dagger\right). \quad \text{(C.17)}$$

This is now rearranged to

$$\hat{H} = \frac{k^2}{2M}\left(\hat{S}_z - \hat{\alpha}\right)^2 + \hat{H}_0 + \frac{1}{2}\gamma\left(\hat{S}_- - \hat{S}_-^\dagger\right) \quad \text{(C.18)}$$

with the additional identities:

$$\Delta\Omega = \Omega_+ - \Omega_-, \tag{C.19}$$

$$\hat{\alpha} = \frac{1}{k}\left(Mgt - \frac{M}{k}\Delta\Omega - \hat{J}\right) = \dot{\alpha}(t - \hat{t}_0), \tag{C.20}$$

$$\dot{\alpha} = \frac{Mg}{k}, \tag{C.21}$$

$$\hat{t}_0 = \frac{1}{Mg}\left(\hat{J} - \Delta\Omega\frac{M}{k}\right), \tag{C.22}$$

$$\hat{H}_0 = \Omega_+\hat{N} - \hat{\alpha}\,\Delta\Omega + \frac{M\Delta\Omega^2}{2k^2}. \tag{C.23}$$

The term $\hat{H}_0$ can be eliminated by defining the propagator $\hat{U} = \exp(i\int \mathrm{d}t\,\hat{H}_0)$ and shifting the states $|J, N; n_+\rangle$ to $\hat{U}\,|J, N; n_+\rangle \equiv |n_+\rangle$.

An additional rescaling to dimensionless time $\tau = \frac{k^2}{M}t$ and coupling $\gamma_0 = \gamma\frac{M}{k^2}$ finally results in the Hamiltonian

$$\hat{H} = \frac{1}{2}\left(\hat{S}_z - \hat{\alpha}\right)^2 + \frac{1}{2}\gamma_0\left(\hat{S}_- + \hat{S}_-^\dagger\right), \tag{C.24}$$

which is now in the form used for the EQPM in Section IV.c.2.

C.iv. Representations in the EQPM

The EQPM is used for Hamiltonians that contain annihilation $\hat{a}_j$, creation $\hat{a}_j^\dagger$ or number operators $\hat{n}_j$. For an arbitrary state $|\psi\rangle$ an associated function is defined by $f(\phi_+, \phi_-)\,|\phi_+, \phi_-\rangle$, with phase terms ϕ_+, ϕ_-.

The action of an operator on a state can now be replaced by the action on the associated function by using differential operators:

$$\begin{aligned} f(\phi_j)\hat{a}_j &\to e^{i\phi_j} f(\phi_j) \\ f(\phi_j)\hat{a}_j^\dagger &\to i\partial_{\phi_j}\left[e^{i\phi_j} f(\phi_j)\right] \\ f(\phi_j)\hat{n}_j &\to e^{i\phi_j} f(\phi_j) \end{aligned} \tag{C.25}$$

To exemplify this, an arbitrary number state $|\eta\rangle = \sum_{m=0}^{\infty}\int_{-\pi}^{+\pi}\mathrm{d}\theta\, e^{im\theta} f(\theta)\,|m\rangle$ is

considered. The effect of the number operator $\hat{n} = \hat{a}^\dagger \hat{a}$ on $|\eta\rangle$ is as expected:

$$\hat{a}^\dagger \hat{a} \, |\eta\rangle = \sum_{m=0}^{\infty} \int_{-\pi}^{+\pi} \mathrm{d}\theta \, e^{im\theta} f(\theta) \, \hat{a}^\dagger \hat{a} \, |m\rangle \tag{C.26}$$

$$= \sum_{m=0}^{\infty} \int_{-\pi}^{+\pi} \mathrm{d}\theta \, e^{im\theta} f(\theta) \, \sqrt{m} \, \hat{a}^\dagger \, |m-1\rangle \tag{C.27}$$

$$= \sum_{m=0}^{\infty} \int_{-\pi}^{+\pi} \mathrm{d}\theta \, e^{im\theta} f(\theta) \, m \, |m\rangle \tag{C.28}$$

Now, using representations instead results in:

$$\begin{aligned}
\hat{a}^\dagger \, |\eta\rangle &\longrightarrow \sum_{m=0}^{\infty} \int_{-\pi}^{+\pi} \mathrm{d}\theta \, e^{im\theta} i\partial_\theta \left[e^{-i\theta} f(\theta) \right] \, |m\rangle \\
&= e^{im\theta} e^{-i\theta} f(\theta) \Big|_{-\pi}^{+\pi} - i \sum_{m=0}^{\infty} \int_{-\pi}^{+\pi} \mathrm{d}\theta \, \left[\partial_\theta \, e^{im\theta} \right] e^{-i\theta} f(\theta) \, |m\rangle \\
&= \sum_{m=0}^{\infty} \int_{-\pi}^{+\pi} \mathrm{d}\theta \, e^{i(m-1)\theta} f(\theta) \, m \, |m\rangle \qquad \text{(C.29)} \\
\hat{a} \, |\eta\rangle &\longrightarrow \sum_{m=0}^{\infty} \int_{-\pi}^{+\pi} \mathrm{d}\theta \, e^{im\theta} e^{i\theta} f(\theta) \, |m\rangle \\
&= \sum_{m=0}^{\infty} \int_{-\pi}^{+\pi} \mathrm{d}\theta \, e^{i(m+1)\theta} f(\theta) \, \, |m\rangle \qquad \text{(C.30)} \\
\Rightarrow \hat{a}^\dagger \hat{a} \, |\eta\rangle &\longrightarrow \sum_{m=0}^{\infty} \int_{-\pi}^{+\pi} \mathrm{d}\theta \, e^{i(m+1)\theta} i \left[\partial_\theta \, e^{im\theta} f(\theta) \right] \, |m\rangle \\
&= \sum_{m=0}^{\infty} \int_{-\pi}^{+\pi} \mathrm{d}\theta \, e^{i(m+1)\theta} m \, e^{-i\theta} f(\theta) \, \, |m\rangle \\
&= \sum_{m=0}^{\infty} \int_{-\pi}^{+\pi} \mathrm{d}\theta \, e^{im\theta} f(\theta) \, m \, |m\rangle \qquad \text{(C.31)}
\end{aligned}$$

Thus, applying the operators $\hat{a}^\dagger \hat{a}$ to a state $|\eta\rangle$ has the same effect as using the representations. For $\hat{a}^\dagger$ (C.30), integration by parts was used. The boundary term vanishes, since $f(\theta)$ is assumed to be 2π-periodic, giving: $f(\theta)\Big|_{-\pi}^{+\pi} = 0$.

The average and relative phase terms are introduced:

$$\begin{aligned}
\phi_\pm &= \bar{\phi} \pm \tfrac{\phi}{2}, \\
\bar{\phi} &= \tfrac{1}{2}(\phi_+ + \phi_-), \\
\phi &= \phi_+ - \phi_-,
\end{aligned} \tag{C.32}$$

with their differentials:

$$\partial_{\phi_\pm} = \frac{1}{2}\partial_{\bar{\phi}} \pm \partial_\phi. \tag{C.33}$$

The states can now be given by Bargmann states with the associated functions:

$$|\psi\rangle_N = \frac{1}{2\pi}\int_{-\pi}^{+\pi} \mathrm{d}\phi\, \psi(\phi) \tag{C.34}$$

$$|\psi\rangle = \frac{1}{2\pi^2}\int_{-\pi}^{+\pi} \mathrm{d}\phi_1\, \mathrm{d}\phi_2\, f(\phi_1,\phi_2)\, |\phi_1,\phi_2\rangle \tag{C.35}$$

$$|\phi_1,\phi_2\rangle = \sum_{l,m=0}^{\infty} e^{i(l\phi_1+m\phi_2)}\, |l\rangle\, |m\rangle \tag{C.36}$$

$$\rightarrow f(\bar{\phi}+\tfrac{\phi}{2},\bar{\phi}-\tfrac{\phi}{2}) = e^{-iN\bar{\phi}}\psi(\phi). \tag{C.37}$$

The general approach is now:

- Multiply with $f(\phi_+,\phi_-)$ on left.
- Use the differential representations.
- Follow the calculations through, then reorder so that $f(\phi_+,\phi_-)$ is on the right and simplify.

$\Rightarrow$ EQPM representation of the Hamiltonian

Some additional identities will be useful:

$$\begin{aligned} e^{-i\phi_\pm} f(\phi_+,\phi_-) &= e^{-i\bar{\phi}\pm\frac{\phi}{2}}\ f(\phi_+,\phi_-) \\ &= e^{-i\bar{\phi}\pm\frac{\phi}{2}}\ e^{-iN\bar{\phi}}\ \psi(\phi) \\ &= e^{-i(N+1)\bar{\phi}}\ e^{\mp\frac{\phi}{2}}\ \psi(\phi) \end{aligned} \tag{C.38}$$

$$\partial_{\bar{\phi}} e^{-i(N+1)\bar{\phi}} e^{\mp\frac{\phi}{2}}\psi(\phi) = e^{-i\bar{\phi}\pm\frac{\phi}{2}}\ (-i(N+1))\ f(\phi_+,\phi_-) \tag{C.39}$$

$$\partial_{\phi} e^{-i(N+1)\bar{\phi}} e^{\mp\frac{\phi}{2}}\psi(\phi) = e^{-i\bar{\phi}\pm\frac{\phi}{2}}(\mp\tfrac{i}{2}+\partial_\phi)\ f(\phi_+,\phi_-) \tag{C.40}$$

This leads to a table of representations for occurring operators and their combinations:

$$f(\phi_+,\phi_-)\,\hat{a}_\pm \to\; e^{i\phi_\pm}\; f(\phi_+,\phi_-) \tag{C.41}$$

$$f(\phi_+,\phi_-)\,\hat{a}^\dagger_\pm \to\; i\partial_{\phi_\pm}\; \left[e^{-i\phi_\pm} f(\phi_+,\phi_-)\right] \tag{C.42}$$

$$f(\phi_+,\phi_-)\,\hat{n}_\pm \to\; i\partial_{\phi_\pm}\; f(\phi_+,\phi_-) \tag{C.43}$$

$$f(\phi_+,\phi_-)\,\hat{n}^2_\pm \to\; -i\partial^2_{\phi_\pm}\; f(\phi_+,\phi_-) \tag{C.44}$$

$$f(\phi_+,\phi_-)\,\hat{a}^\dagger_\pm\hat{a}_\mp \to\; e^{\mp i\phi}\; \left(\tfrac{N}{2}+1\pm i\partial_\phi\right) \tag{C.45}$$

$$f(\phi_+,\phi_-)\,(\hat{n}_+-\hat{n}_-)^2 \to\; -2\,\partial^2_\phi f(\phi_+,\phi_-) \tag{C.46}$$

$$f(\phi_+,\phi_-)\,(\hat{a}^\dagger_+\hat{a}_- + \hat{a}^\dagger_-\hat{a}_+) \to\; (N+2)\cos(\phi)+2\sin(\phi)\,\partial_\phi \tag{C.47}$$

Now these representations for the Hamiltonian's constituents can be used on the *quantum engine Hamiltonian* (IV.19):

$$\hat{H} = \frac{1}{2}\left(\hat{S}_z-\hat{\alpha}\right)^2 + \frac{1}{2}\gamma_0\left(\hat{S}_- + \hat{S}^\dagger_-\right). \tag{C.48}$$

Rewriting this a bit and using the representations leads to:

$$\begin{aligned}
\frac{\gamma_0}{2}(\hat{S}_- + \hat{S}^\dagger_-) &= \frac{\gamma_0}{2}(\hat{a}^\dagger_+\hat{b}_- + \hat{b}^\dagger_-\hat{a}_+)\\
&\to \frac{\gamma_0}{2}\left((N+2)\cos(\phi)+2\sin(\phi)\partial_\phi\right)\\
&= \gamma_0\left(\left(\tfrac{N}{2}+1\right)\cos(\phi)+\sin(\phi)\partial_\phi\right),
\end{aligned}$$

$$\begin{aligned}
\left(\hat{S}_z-\hat{\alpha}\right)^2 &= \hat{S}^2_z - \hat{S}_z\hat{\alpha} - \hat{\alpha}\,\hat{S}_z + \hat{\alpha}^2\\
&= \hat{S}^2_z - 2\hat{S}_z\hat{\alpha} + \hat{\alpha}^2\\
&= \tfrac{1}{4}(\hat{n}_+-\hat{m}_-)^2 - \dot{\alpha}(t-t_0)(\hat{n}_+-\hat{m}_-) + \dot{\alpha}^2(t-t_0)^2\\
&\to\; -\tfrac{1}{2}\partial^2_\phi - i\alpha\partial_\phi + \alpha^2.
\end{aligned}$$

From here follows the *Exact Quantum Phase Model Hamiltonian* of the Quantum Daemon engine:

$$\begin{aligned}
\hat{H}_{\mathrm{EQPM}} &= -\tfrac{1}{2}\partial^2_\phi - i\alpha\partial_\phi + \alpha^2 + \gamma_0\left(\left(\tfrac{N}{2}+1\right)\cos(\phi)+\sin(\phi)\partial_\phi\right)\\
&= -\tfrac{1}{2}\partial^2_\phi + (\gamma_0\sin(\phi) - i\alpha)\,\partial_\phi + \alpha^2 + \gamma_0\left(\left(\tfrac{N}{2}+1\right)\cos(\phi)\right)
\end{aligned} \tag{C.49}$$

C.v. Quantum Canonical Transformation of the ADR-Hamiltonian

Starting Point here is the general ADR-Hamiltonian:

$$\hat{H}_{\mathrm{ADR}}(\hat{q},\hat{p}) = \frac{1}{2}\hat{p}^2 + C(\hat{q},t)\,\hat{p} + V(\hat{q},t), \tag{C.50}$$

where $\hat{p} = -i\partial_q$ and $C, V \in \mathbb{R}$.

For the tilted washboard in the EQPM, the potential function is:

$$V(\hat{q}, t) = \dot{\lambda}\hat{q} - \tfrac{1}{2}\gamma\left(\cos(\hat{q}) + 4\dot{\lambda}\sin(\hat{q})\right) + \tfrac{1}{2}\gamma^2\left(\sin^2(\hat{q}) + 4\dot{\lambda}\sin(\hat{q})\right), \tag{C.51}$$

which can be reduced by leaving out terms that are not relevant for the dynamics:

$$V_{\mathrm{r}}(\hat{q}, t) = \dot{\lambda}\hat{q} + 2\left(\gamma\lambda(t)\cos(\hat{q})\right)^2 + \gamma_N\cos(\hat{q}). \tag{C.52}$$

The advection coefficient function is:

$$C(\hat{q}, t) = -2\gamma\lambda(t)\cos(\hat{q}). \tag{C.53}$$

First, the Hamiltonian function will be rearranged. In classical mechanics, the Hamiltonian $\mathcal{H} = \frac{p^2}{2} + Cp + V$ can easily be put into the form $\mathcal{H} = \frac{(p+C)^2}{2} + V - \frac{C^2}{2}$ by completing the square. In the quantum case the commutator $[C(\hat{q}, t), \hat{p}]$ has to be considered.

$$(\hat{p} + C)^2 = \hat{p}^2 + \hat{p}C + C\hat{p} + C^2 \tag{C.54}$$

$$[\hat{p}, C(\hat{q})] = \hat{p}C - C\hat{p} = -i\partial_q C \tag{C.55}$$

$$\Rightarrow \hat{p}C = C\hat{p} - iC' \tag{C.56}$$

$$\Rightarrow (\hat{p} + C)^2 = \hat{p}^2 + 2C\hat{p} + C^2 - iC' \tag{C.57}$$

For Equation C.50 this leads to:

$$H = \frac{1}{2}\hat{p}^2 + C\hat{p} + V = \frac{1}{2}\left(\hat{p}^2 + 2C\hat{p} + 2V\right) \tag{C.58}$$

$$= \frac{1}{2}\left(\hat{p}^2 + 2C\hat{p} + C^2 - iC' - C^2 + iC' + 2V\right) \tag{C.59}$$

$$= \frac{1}{2}(\hat{p} + C)^2 + V - \frac{1}{2}C^2 - \frac{i}{2}C' \tag{C.60}$$

A new potential can be defined by $U = V - \frac{C^2 + iC'}{2}$, resulting in the Hamiltonian:

$$\hat{H} = \frac{1}{2}(\hat{p} + C)^2 + U. \tag{C.61}$$

This suggests a one-variable similarity transformation – or gauge transformation – to shift the momentum:

$$q \mapsto q,\ p \mapsto \hat{P} = \hat{p} + C, \tag{C.62}$$

with the generator $\hat{F} = e^{-f(\hat{q},t)}$, leading to:

$$\hat{P} = e^{-f\hat{p}e^{f}} = \hat{p} - i\partial_q f \tag{C.63}$$

$$\Rightarrow C \stackrel{!}{=} -i\partial_q f \;\Rightarrow\; f(\hat{q},t) = i\int^{q} \mathrm{d}\xi\, C(\xi,t) =: i\gamma(\hat{q},t). \tag{C.64}$$

The time-dependency of the transformation is taken into account by:

$$\hat{p}_t \mapsto \hat{P}_t = \hat{p}_t + i\dot{f} = \hat{p}_t - \dot{\gamma}. \tag{C.65}$$

This transforms the Schrödinger operator:

$$\hat{\mathscr{H}} \mapsto \hat{\mathscr{K}} = \hat{P}_t + \frac{1}{2}\hat{P}^2 + \tilde{U} \tag{C.66}$$

with the transformed potential $\tilde{U}$:

$$\begin{aligned}\tilde{U} &= V - \frac{C^2}{2} - \frac{\hat{P}C}{2} \\ &= V - \frac{C^2}{2} - \frac{1}{2}(\hat{p}+C)C \\ &= V - C^2 - \frac{i}{2}C'.\end{aligned} \tag{C.67}$$

The transformed Schrödinger operator $\hat{\mathscr{K}}$ now reads:

$$\begin{aligned}\hat{\mathscr{K}} &= \hat{P}_t + \frac{1}{2}\hat{P}^2 + V - C^2 - \frac{i}{2}C' \\ &= \hat{p}_t + \frac{1}{2}\hat{P}^2 + V - \left(C^2 + \frac{i}{2}C' + \dot{\gamma}\right) \\ &= \hat{p}_t + \frac{1}{2}\hat{P}^2 + V - w,\end{aligned} \tag{C.68}$$

where: $w = C^2 + \frac{i}{2}C' + \dot{\gamma} = (\gamma')^2 + \frac{i}{2}\gamma'' + \dot{\gamma}$.

From this follows the Kamiltonian as:

$$\hat{K} = \frac{1}{2}(\hat{p}+C)^2 + V - w. \tag{C.69}$$

Taking a closer look at the transformed potential $\tilde{V} = V - w$ shows an imaginary part:

$$\begin{aligned}\mathrm{Im}(\tilde{V}) &= \frac{1}{2}\gamma'' =: \Gamma, \\ \mathrm{Re}(\tilde{V}) &= V - (\gamma')^2 - \dot{\gamma} =: W\end{aligned} \tag{C.70}$$

$$\Rightarrow\; \hat{K} = \frac{1}{2}(\hat{p}+C)^2 + W + i\Gamma. \tag{C.71}$$

Γ is connected to the commutator of $\hat{p}$ and $C(\hat{q},t)$, which was introduced by rearranging the Hamiltonian.

Bibliography

1. Schumacher, K. & Krebs, M. The V-ATPase: small cargo, large effects. *Current Opinion in Plant Biology* **13,** 724–730. ISSN: 13695266. https://linkinghub.elsevier.com/retrieve/pii/S1369526610001007 (2019) (Dec. 2010).
2. Schliwa, M. & Woehlke, G. Molecular motors. *Nature* **422,** 759–765. ISSN: 0028-0836, 1476-4687. http://www.nature.com/articles/nature01601 (2019) (Apr. 2003).
3. Nelson, N. *et al.* The cellular biology of proton-motive force generation by V-ATPases. *Journal of Experimental Biology* **203,** 89. http://jeb.biologists.org/content/203/1/89.abstract (Jan. 1, 2000).
4. Pänke, O. & Rumberg, B. Energy and entropy balance of ATP synthesis. *Biochimica et Biophysica Acta (BBA) - Bioenergetics* **1322,** 183–194. ISSN: 00052728. https://linkinghub.elsevier.com/retrieve/pii/S0005272897000790 (2019) (Dec. 1997).
5. Nakanishi-Matsui, M., Sekiya, M., Nakamoto, R. K. & Futai, M. The mechanism of rotating proton pumping ATPases. *Biochimica et Biophysica Acta (BBA) - Bioenergetics* **1797,** 1343–1352. ISSN: 00052728. https://linkinghub.elsevier.com/retrieve/pii/S000527281000068X (2019) (Aug. 2010).
6. Gilz, L., Thesing, E. & Anglin, J. R. Hamiltonian analogs of combustion engines: A systematic exception to adiabatic decoupling. *Physical Review E* **94.** ISSN: 2470-0045 (Oct. 21, 2016).
7. Thesing, E. P., Gilz, L. & Anglin, J. R. Quantum Hamiltonian daemons: Unitary analogs of combustion engines. *Physical Review E* **96.** ISSN: 2470-0045, 2470-0053. http://link.aps.org/doi/10.1103/PhysRevE.96.012119 (2018) (July 11, 2017).
8. Gilz, L. *Understanding more with less - Small model systems for non-equilibrium processes* PhD thesis (TU Kaiserslautern, Kaiserslautern, Nov. 11, 2014).
9. Thesing, E. *Towards a Hamiltonian Description of Thermodynamic Phenomena* PhD thesis (TU Kaiserslautern, Kaiserslautern, Mar. 7, 2017).
10. Eichmann, T., Thesing, E. P. & Anglin, J. R. Engineering separatrix volume as a control technique for dynamical transitions. *Physical Review E* **98.** ISSN: 2470-0045, 2470-0053. https://link.aps.org/doi/10.1103/PhysRevE.98.052216 (2019) (Nov. 19, 2018).
11. Dobrott, D. Probability of Trapping-State Transitions in a Toroidal Device. *Physics of Fluids* **14,** 1525. ISSN: 00319171. https://aip.scitation.org/doi/10.1063/1.1693639 (2019) (1971).

12. Nolting, W. *Grundkurs Theoretische Physik 5/1* ISBN: 978-3-540-68869-3. http://link.springer.com/10.1007/978-3-540-68869-3 (2019) (Springer Berlin Heidelberg, Berlin, Heidelberg, 2009).

13. Gurney, R. W. & Condon, E. U. Wave Mechanics and Radioactive Disintegration. *Nature* **122,** 439–439. ISSN: 1476-4687. https://doi.org/10.1038/122439a0 (Sept. 1, 1928).

14. Fonda, L., Ghirardi, G. C. & Rimini, A. Decay theory of unstable quantum systems. *Reports on Progress in Physics* **41,** 587–631. ISSN: 0034-4885, 1361-6633. http://stacks.iop.org/0034-4885/41/i=4/a=003?key=crossref.f2753cffba41e218512d914caf410bc6 (2019) (Apr. 1, 1978).

15. Breit, G. & Wigner, E. Capture of Slow Neutrons. *Physical Review* **49,** 519–531. ISSN: 0031-899X. https://link.aps.org/doi/10.1103/PhysRev.49.519 (2019) (Apr. 1, 1936).

16. Rennert, P., Chassé, A. & Hergert, W. *Einführung in die Quantenphysik* OCLC: 846995409. ISBN: 978-3-658-00770-6 (Springer Spektrum, Wiesbaden, 2013).

17. Khalfin, L. A. Contribution to the Decay Theory of a Quasi-Stationary State. *Soviet Phys. JETP* **Vol: 6.** https://www.osti.gov/biblio/4318804 (2019) (June 1, 1958).

18. Razavy, M. *Quantum theory of tunneling* 2nd edition. ISBN: 978-981-4525-00-8 (World Scientific, New Jersey, 2014).

19. Bartelmann, M. *et al. Theoretische Physik* in collab. with Modler, F. & Kreh, M. OCLC: 896809458. ISBN: 978-3-642-54618-1 (Springer Spektrum, Berlin Heidelberg, 2015).

20. Gamow, G. Zur Quantentheorie des Atomkernes. *Zeitschrift für Physik* **51,** 204–212. ISSN: 1434-6001, 1434-601X. http://link.springer.com/10.1007/BF01343196 (2019) (Mar. 1928).

21. Gurvitz, S. A. & Kalbermann, G. Decay width and the shift of a quasistationary state. *Physical Review Letters* **59,** 262–265. ISSN: 0031-9007. https://link.aps.org/doi/10.1103/PhysRevLett.59.262 (2019) (July 20, 1987).

22. Gurvitz, S. A. Novel approach to tunneling problems. *Physical Review A* **38,** 1747–1759. ISSN: 0556-2791 (Aug. 1, 1988).

23. Crank, J. & Nicolson, P. A practical method for numerical evaluation of solutions of partial differential equations of the heat-conduction type. *Mathematical Proceedings of the Cambridge Philosophical Society* **43,** 50–67. ISSN: 1469-8064, 0305-0041. https://www.cambridge.org/core/journals/mathematical-proceedings-of-the-cambridge-philosophical-society/article/practical-method-for-numerical-evaluation-of-solutions-of-partial-differential-equations-of-the-heatconduction-type/B3230893A53384D418228AB39D41A451 (2019) (Jan. 1947).

24. Schwarz, H. R. & Köckler, N. *Numerische Mathematik* 8., aktualisierte Aufl. OCLC: 729948453. 591 pp. ISBN: 978-3-8348-1551-4 (Vieweg + Teubner, Wiesbaden, 2011).

25. Aldrovandi, R. & Ferreira, P. L. Quantum pendulum. *American Journal of Physics* **48,** 660–664. ISSN: 0002-9505, 1943-2909. http://aapt.scitation.org/doi/10.1119/1.12332 (2018) (Aug. 1980).

26. Mechel, F. P. *Mathieu functions: formulas, generation, use* ISBN: 978-3-7776-0810-5 (S. Hirzel Verlag, Stuttgart, 1997).

27. Cojocaru, E. Mathieu functions computational toolbox implemented in Matlab. *arXiv:0811.1970 [math-ph, physics:physics].* arXiv: 0811.1970. https://mathworks.com/matlabcentral/fileexchange/22081-mathieu-functions-toolbox-v-1-0 (2019) (Nov. 13, 2008).

28. Curtright, T., Fairlie, D. & Zachos, C. *A concise treatise on quantum mechanics in phase space* ISBN: 978-981-4520-43-0 (World Scientific, New Jersey, 2014).

29. Hillery, M., O'Connell, R. F., Scully, M. O. & Wigner, E. P. Distribution functions in physics: Fundamentals. *Physics Reports* **106,** 121–167. ISSN: 0370-1573. http://www.sciencedirect.com/science/article/pii/0370157384901601 (2019) (Apr. 1, 1984).

30. Groenewold, H. On the principles of elementary quantum mechanics. *Physica* **12,** 405–460. ISSN: 00318914. https://linkinghub.elsevier.com/retrieve/pii/S0031891446800594 (2019) (Oct. 1946).

31. Moyal, J. E. Quantum mechanics as a statistical theory. *Mathematical Proceedings of the Cambridge Philosophical Society* **45,** 99–124. ISSN: 0305-0041, 1469-8064. https://www.cambridge.org/core/product/identifier/S0305004100000487/type/journal_article (2019) (Jan. 1949).

32. Marinov, M. S. & Segev, B. Quantum tunneling in the Wigner representation. *Physical Review A* **54,** 4752–4762. ISSN: 1050-2947 (Dec. 1, 1996).

33. Auger, F., Flandrin, P., Gonçalves, P. & Lemoine, O. Time-frequency toolbox tutorial. *CNRS (France), Rice U.(USA).* http://tftb.nongnu.org/ (Jan. 1, 2005).

34. Bondar, D. I., Cabrera, R., Zhdanov, D. V. & Rabitz, H. A. Wigner phase space distribution as a wave function. *Physical Review A* **88,** 052108. ISSN: 1050-2947, 1094-1622. arXiv: 1202.3628. http://arxiv.org/abs/1202.3628 (2019) (Nov. 11, 2013).

35. Cabrera, R., Bondar, D. I., Jacobs, K. & Rabitz, H. A. Efficient method to generate time evolution of the Wigner function for open quantum systems. *Physical Review A* **92,** 042122. ISSN: 1050-2947, 1094-1622. arXiv: 1212.3406. http://arxiv.org/abs/1212.3406 (2019) (Oct. 28, 2015).

36. Cabrera, R., Bondar, D. I., Jacobs, K. & Rabitz, H. A. Wigner function's exact and numerically effective propagator. *Physical Review A* **92,** 042122. ISSN: 1050-2947, 1094-1622. arXiv: 1212.3406. http://arxiv.org/abs/1212.3406v2 (2019) (Oct. 28, 2015).

37. Koopman, B. O. Hamiltonian Systems and Transformation in Hilbert Space. *Proceedings of the National Academy of Sciences* **17,** 315–318. ISSN: 0027-8424, 1091-6490. http://www.pnas.org/cgi/doi/10.1073/pnas.17.5.315 (2019) (May 1, 1931).

38. Von Neumann, J. Zur Operatorenmethode In Der Klassischen Mechanik. *The Annals of Mathematics* **33,** 587. ISSN: 0003486X. https://www.jstor.org/stable/1968537?origin=crossref (2019) (July 1932).

39. Von Neumann, J. Zusatze Zur Arbeit „Zur Operatorenmethode... *The Annals of Mathematics* **33,** 789. ISSN: 0003486X. https://www.jstor.org/stable/1968225?origin=crossref (2019) (Oct. 1932).

40. Kubo, R. Wigner Representation of Quantum Operators and Its Applications to Electrons in a Magnetic Field. *Journal of the Physical Society of Japan* **19,** 2127–2139. ISSN: 0031-9015, 1347-4073. http://journals.jps.jp/doi/10.1143/JPSJ.19.2127 (2019) (Nov. 15, 1964).

41. Anglin, J. R., Drummond, P. & Smerzi, A. Exact quantum phase model for mesoscopic Josephson junctions. *Physical Review A* **64.** ISSN: 1050-2947, 1094-1622. https://link.aps.org/doi/10.1103/PhysRevA.64.063605 (2019) (Nov. 13, 2001).

42. Bender, C. M. Introduction to PT-Symmetric Quantum Theory. *arXiv:quant-ph/0501052.* http://arxiv.org/abs/quant-ph/0501052 (2019) (Jan. 11, 2005).

43. Bender, C. M. Making sense of non-Hermitian Hamiltonians. *Reports on Progress in Physics* **70,** 947–1018. ISSN: 0034-4885, 1361-6633. http://stacks.iop.org/0034-4885/70/i=6/a=R03?key=crossref.2186014795bc6e743a5817786698d9f5 (2019) (June 1, 2007).

44. Kuzmin, D. *A Guide to Numerical Methods for Transport Equations* 2010. http://www.mathematik.uni-dortmund.de/~kuzmin/cfdbook.html.

45. Schilling, L. *Direct dynamical tunneling in systems with a mixed phase space* PhD thesis (Technishce Universität Dresden, Dresden, Dec. 11, 2006). 195 pp. (2018).

46. Chirikov, B. & Shepelyansky, D. Chirikov standard map. *Scholarpedia* **3,** 3550. ISSN: 1941-6016. http://www.scholarpedia.org/article/Chirikov_standard_map (2019) (Mar. 3, 2008).

47. Schlagheck, P., Mouchet, A. & Ullmo, D. Resonance-assisted tunneling in mixed regular-chaotic systems. *arXiv:1105.5362 [nlin].* http://arxiv.org/abs/1105.5362 (2019) (May 26, 2011).

48. Case, W. B. Wigner functions and Weyl transforms for pedestrians. *American Journal of Physics* **76,** 937–946. ISSN: 0002-9505, 1943-2909. http://aapt.scitation.org/doi/10.1119/1.2957889 (2019) (Oct. 2008).

49. Zachos, C. K. Deformation Quantization: Quantum Mechanics Lives and Works in Phase-Space. *International Journal of Modern Physics A* **17,** 297–316. ISSN: 0217-751X, 1793-656X. arXiv: hep-th/0110114. http://arxiv.org/abs/hep-th/0110114 (2019) (Jan. 30, 2002).

50. Zachos, C. K., Farnell, D. J. J. & Curtright, T. in *Quantum Mechanics in Phase Space* 0 vols. *World Scientific Series in 20th Century Physics* Volume 34, 1–30 (WORLD SCIENTIFIC, Dec. 1, 2005). ISBN: 978-981-238-384-6. https://www.worldscientific.com/doi/abs/10.1142/9789812703507_0001 (2019).

51. Wigner, E. On the Quantum Correction For Thermodynamic Equilibrium. *Physical Review* **40,** 749–759. ISSN: 0031-899X. https://link.aps.org/doi/10.1103/PhysRev.40.749 (2019) (June 1, 1932).

52. Weyl, H. Quantenmechanik und Gruppentheorie. *Zeitschrift für Physik* **46,** 1–46. ISSN: 1434-6001, 1434-601X. http://link.springer.com/10.1007/BF02055756 (2019) (Nov. 1927).

53. De Gosson, M. A. & Luef, F. Born–Jordan Pseudodifferential Calculus, Bopp Operators and Deformation Quantization. *Integral Equations and Operator Theory* **84,** 463–485. ISSN: 0378-620X, 1420-8989. http://link.springer.com/10.1007/s00020-015-2273-y (2019) (Apr. 2016).

54. Dereli, T., Hakioglu, T. & Tegmen, A. Quantum canonical transformations in Weyl-Wigner-Groenewold-Moyal formalism. *International Journal of Modern Physics A* **24,** 4573–4587. ISSN: 0217-751X, 1793-656X. arXiv: 0904.3416. http://arxiv.org/abs/0904.3416 (2019) (Sept. 30, 2009).

55. Anderson, A. Canonical Transformations in Quantum Mechanics. *Annals of Physics* **232,** 292–331. ISSN: 00034916. arXiv: hep-th/9305054. http://arxiv.org/abs/hep-th/9305054 (2019) (June 1994).

56. Bondar, D. I., Cabrera, R., Lompay, R. R., Ivanov, M. Y. & Rabitz, H. A. Operational Dynamic Modeling Transcending Quantum and Classical Mechanics. *Physical Review Letters* **109,** 190403. ISSN: 0031-9007, 1079-7114. arXiv: 1105.4014. http://arxiv.org/abs/1105.4014 (2019) (Nov. 8, 2012).

57. Mauro, D. Topics in Koopman-von Neumann Theory. *arXiv:quant-ph/0301172.* http://arxiv.org/abs/quant-ph/0301172 (2019) (Jan. 30, 2003).

58. Polkovnikov, A. Phase space representation of quantum dynamics. *Annals of Physics* **325,** 1790–1852. ISSN: 00034916. https://linkinghub.elsevier.com/retrieve/pii/S0003491610000382 (2019) (Aug. 2010).

59. Robertson, D. G. *Solving the Time-Dependent Schrödinger Equation* Oct. 10, 2011. http://faculty.otterbein.edu/DRobertson/compsci/tise-stud.pdf.

60. Trotter, H. F. On the product of semi-groups of operators. *Proceedings of the American Mathematical Society* **10,** 545–545. ISSN: 0002-9939. http://www.ams.org/jourcgi/jour-getitem?pii=S0002-9939-1959-0108732-6 (2019) (Apr. 1, 1959).

61. Arnold, A., Ehrhardt, M. & Sofronov, I. Discrete transparent boundary conditions for the Schrödinger equation: fast calculation, approximation, and stability. *Communications in Mathematical Sciences* **1,** 501–556. ISSN: 15396746, 19450796. `http://www.intlpress.com/site/pub/pages/journals/items/cms/content/vols/0001/0003/a007/` (2019) (2003).